

Computational materials chemistry:
from polymer precursors to ceramics
and high-pressure materials

by

Shariq Haseen

DISSERTATION

Submitted in partial fulfillment of the requirements

For the degree of Doctor of Philosophy

At The University of Texas at Arlington

August 2022

Arlington, Texas

Supervising Committee:

Dr. Peter Kroll

Dr. Kwangho Nam

Dr. Krishnan Rajeshwar

Dr. Jongyun Heo

ABSTRACT

With advances in computing power, the field of computational chemistry has flourished. Using current computational resources, atomistic simulations of billion atoms and trillions of atoms have been performed. Computational techniques can be used to support experimental investigations into new materials as well as independently predict the existence of new materials. Furthermore, computational techniques are becoming instrumental in investigations.

This work is split into two parts. Part I focuses on high-pressure and materials chemistry. We investigate the cristobalite-rutile transformation for SiO_2 , GeO_2 , and TiO_2 , and predict conditions at which cristobalite- GeO_2 and cristobalite- TiO_2 may be synthesized (Chapter 1), we provide supporting calculations for the discovery of two ternary compounds, $\text{Sn}_2\text{N}_2\text{O}$ (Chapter 2) and Si-Ti-N (Chapter 3), synthesized at high pressure, and we investigate the work of adhesion in compound graphene- $\text{SiO}_2/\text{Si}_2\text{CO}_2$ systems (Chapter 4). Part II is focused on studying amorphous ceramics, including polymer-derived ceramics with classical methods. We calculate elastic properties of SiCO ceramics and determine the impact of free carbon content, density, and free carbon morphology (Chapter 1), we develop a new method to quantify the extent of the free carbon morphology in large atomistic systems (Chapter 2), and we develop a new parametrization of the reactive force field ReaxFF for simulations of the polymer-to-ceramic conversion process used to synthesize silicon carbonitride from polysilazanes (Chapter 3).

Copyright by
Shariq Haseen
2022

ACKNOWLEDGEMENTS

First and foremost, I would like to express my deepest gratitude to my advisor Dr. Peter Kroll for his guidance and supervision as I completed my research. Throughout my graduate career, Dr. Kroll provided me extensive teaching, gave me interesting and challenging projects, and supported my conference presentations. From my first physical chemistry lecture with Dr. Kroll to my final research project, Dr. Kroll always pushed me to be a better chemist.

I would like to thank the members of my dissertation committee: Dr. Kwangho Nam, Dr. Krishnan Rajeshwar, and Dr. Jongyun Heo for taking the time to conduct my examinations and providing guidance as I worked toward my degree.

I am grateful for having worked alongside the current and former members of the Kroll group: Ilia Ponomarev, Poroshat Taheri, Akshada Hande, Susana Aguirre-Medel, Atreyi Dasmahapatra, Hanof Alkhaldi, Kendall Hendrix, Mitchell Falgoust, Jared Enriquez, Eman Alasadi, and Greg Monson. I would especially like to thank Dr. John Lang who always showed great interest in my work and provided insightful comments.

I would like to thank the departmental staff: Stephanie Henry, Debbie Cooke, and Jill Howard for help with departmental procedures, scheduling classes, and helping me stay on track for my degree.

I would like to acknowledge some of my fellow graduate students: Sam Sung, Beata Dulko-Smith, Adway Zacharias, Abiud Portillo, Radhiyah Himawan, and Anthony Samuel. Additionally, I would like to thank Tobias Kroll and Brandon Lawrence for providing me technical advice in terms of software and programming.

Finally, I would like to thank my family, my parents, Ahmad and Yasmin Haseen, and my brothers, Fraz and Shazib Haseen, for always supporting me.

TABLE OF CONTENTS

ABSTRACT.....	II
ACKNOWLEDGEMENTS.....	IV
LIST OF FIGURES AND TABLES.....	VI
LIST OF ABBREVIATIONS.....	XIII
INTRODUCTION	1
PART I: HIGH-PRESSURE AND MATERIALS CHEMISTRY	7
CHAPTER 1: PAVING THE WAY FOR CRISTOBALITE TiO_2 AND GeO_2 ATTAINABLE UNDER MODERATE TENSILE STRESS: A DFT STUDY OF TRANSFORMATION PATHS AND ACTIVATION BARRIERS IN CRISTOBALITE- RUTILE TRANSFORMATIONS OF MO_2 (M = Si, Ge, Ti)	8
CHAPTER 2: A NOVEL HIGH-PRESSURE TIN OXYNITRIDE $\text{Sn}_2\text{N}_2\text{O}$	34
CHAPTER 3: DISCOVERY OF TERNARY SILICON TITANIUM NITRIDE WITH SPINEL-TYPE STRUCTURE	55
CHAPTER 4: WORK OF ADHESION IN GRAPHENE- SiO_2 AND GRAPHENE-SiC	83
PART II: CALCULATION AND SIMULATION OF AMORPHOUS CERAMICS	94
CHAPTER 1: ANALYZING THE EFFECT OF COMPOSITION, DENSITY, AND THE MORPHOLOGY OF THE “FREE” CARBON PHASE ON ELASTIC MODULI IN SILICON OXYCARBIDE CERAMICS	95
CHAPTER 2: QUANTIFICATION OF FREE CARBON PHASE MORPHOLOGY ..	122
CHAPTER 3: DEVELOPMENT OF A REACTIVE FORCE FIELD FOR SIMULATIONS OF SiCNH POLYMER-DERIVED CERAMICS	126
CONCLUSIONS.....	139
APPENDIX A.....	142
PUBLICATION INFORMATION AND CONTRIBUTING AUTHORS	143

LIST OF FIGURES AND TABLES

PART I

CHAPTER 1

Table 1: Generic description of lattice parameters and coordinates of cristobalite-type and rutile-type structures using the common space group $C222_1$ (20). The choice of parameters (e.g. 1 rather than 0) allows to describe the transition between of cristobalite and rutile by interpolation between the respective parameters. 13

Figure 1: Initial (top left), intermediate (top middle) and final (top right) step of the transformation path from cristobalite to rutile. The orthorhombic common unit cell (SpGr. $C222_1$) is outlined. Si atoms are blue and O atoms are red. For one Si we highlight its initially four (4) coordinating oxygen neighbors (purple) and the two additional oxygen (green) approaching it to form the final SiO_6 -octahedron. Enlarged views of the forming octahedral SiO_6 during the transformation are shown directly beneath the corresponding step in the transformation path.[34] 14

Table 2: Lattice parameters and internal parameters of $C222_1$ cristobalite-type and rutile-type SiO_2 , GeO_2 , TiO_2 from structures optimized with PBE and SCAN functionals. ^a[35], ^b[36], ^c[37], ^d[38], ^e[39] 15

Table 3: Optimized energies of cristobalite-type and rutile-type SiO_2 , GeO_2 , and TiO_2 at ambient pressure, energy differences ΔE from cristobalite-type to rutile-type, and computed transition pressures p_t found using PBE and SCAN functionals 16

Figure 2: E-V diagrams with quantities given per formula unit (f.u.) for cristobalite-type and rutile-type SiO_2 , GeO_2 , and TiO_2 using PBE (left) and SCAN (right) functionals. . 17

Figure 3: Enthalpy-pressure diagrams for MO_2 (M=Si, Ge, Ti) relative to enthalpy of corresponding cristobalite-type using PBE and SCAN functionals. Cristobalite-rutile transition pressures are found at intersections of enthalpy curves..... 19

Figure 4: Enthalpy profiles of SiO_2 α -cristobalite (step=0) to stishovite (step=20) transition at various pressures. PBE calculations for (top left) anion and (top right) cation method; SCAN calculations for (bottom left) anion and (bottom right) cation

method. All enthalpies are given relative to α -cristobalite SiO_2 at the corresponding pressure. 21

Table 4: Forward activation enthalpies $\Delta H_{a,\text{fwd}}$ for SiO_2 cristobalite-rutile transformations. The asterisk (*) indicates the transition pressure computed in the respective method. 22

Figure 5: Enthalpy profiles of GeO_2 α -cristobalite (step=0) to rutile (step=20) transition at ambient and transition pressure p_t . PBE calculations for (top left) anion and (top right) cation method; SCAN calculations for (bottom left) anion and (bottom right) cation method. All enthalpies are given relative to rutile GeO_2 at corresponding pressure..... 24

Table 5: Reverse activation enthalpies $\Delta H_{a,\text{rev}}$ for GeO_2 cristobalite-rutile transformations. The asterisk (*) indicates the transition pressure computed in the respective method. 24

Figure 6: Enthalpy profiles of TiO_2 α -cristobalite (step=0) to rutile (step=20) transition at ambient and transition pressure p_t . PBE calculations for (top left) anion and (top right) cation method; SCAN calculations for (bottom left) anion and (bottom right) cation method. All enthalpies are given relative to rutile TiO_2 at corresponding pressure. Two points in the diagram for cation method with SCAN (step 1 at -1.9GPa and step 14 at 0 GPa) could not be optimized. 25

Table 6: Reverse activation enthalpies $\Delta H_{a,\text{rev}}$ for TiO_2 cristobalite-rutile transformations. The asterisk (*) indicates the transition pressure computed in the respective method. 26

Figure 7: Enthalpy profiles of transformations from cristobalite- SiO_2 to stishovite- SiO_2 and stishovite- SiO_2 to cristobalite- SiO_2 ; transformations were done at zero pressure with PBE using the half-cation method. Enthalpies are relative to the enthalpy of α -cristobalite- SiO_2 28

CHAPTER 2

Figure 1. XRD pattern of SNO, in full (top) and magnified by a factor of ≈ 20 (bottom), with Rietveld refinement (green line) in space group $Pbcn$ ($\lambda=0.20736 \text{ \AA}$). The reflection markers show the calculated reflection positions of the SNO phase (upper row, in red online) and the spinel Sn_3N_4 (lower row, in blue online). 38

Table 1. Atomic positions of SNO in space group <i>Pbcn</i> (No. 60) from experiment and DFT calculations.....	42
--	----

Figure 2. Crystal structure of SNO. a) Unit cell, showing the distorted octahedral coordination of Sn. b) View along the a-axis, showing grey and yellow coloured octahedra sharing faces (indicated as red triangles). Additional edge sharing (indicated as green lines) connects octahedra into chains running along the b-axis.	42
--	----

Table 2. Bond distances of Sn ₂ N ₂ O from experiment in comparison to DFT calculations.	43
---	----

Figure 3. a) Pressure dependence of the unit-cell volume of SNO and the 3rd order Birch–Murnaghan EoS fitted to the data. b) The same EoS, rescaled to show the normalized stress F in dependence on Eulerian strain f . In the fF plot a 3rd order BM EoS displays as a straight line with y-axis intercept B_0 and slope proportional to $(B'-4)$	44
--	----

Figure 4. Reaction enthalpy (PBE results) of the reaction $\text{SnO}_2 + \text{Sn}_3\text{N}_4 \rightarrow 2\text{Sn}_2\text{N}_2\text{O}$ as a function of pressure. The labels indicate (1) transformation of spinel-type Sn ₂ N ₂ O to <i>Pbcn</i> -Sn ₂ N ₂ O (at 4.6 GPa), (2) $\Delta H_f=0$ (12.0 GPa), (3) transformation of rutile-type SnO ₂ to α -PbO ₂ -type SnO ₂ (12.5 GPa), and (4) transformation of α -PbO ₂ -type SnO ₂ to pyrite-type SnO ₂ (17.2 GPa).	46
--	----

CHAPTER 3

Figure 1: Overview of some high-pressure nitrides experimentally synthesized and theoretically predicted, after W.-Y. Ching et al.[4]	57
---	----

Figure 2: Synthesis procedure for the preparation of the SiTiN single-source precursor (SSP) according to reference[19].	60
---	----

Figure 3: X-ray powder diffraction of SiTiN-run HH112 ($\lambda = 0.207109 \text{ \AA}$) and Rietveld refinement.	61
--	----

Figure 4: (a) Low-magnified ADF-STEM image, (b) ADF-STEM image obtained from a single grain, (c) Ti- <i>K</i> edge STEM-EDX mapping obtained from (b). (d) Atomic-resolution ADF-STEM image obtained from the yellow-framed section shown in (b).at the interface between γ -Si ₃ N ₄ and ternary (Si,Ti) ₃ N ₄ particle (e) EELS profiles of Si- <i>L</i> , N- <i>K</i> and Ti- <i>L</i> _{2,3} edges across the ternary (Si,Ti) ₃ N ₄ nano-particle, where the black, blue,	
--	--

pink and red-colored profiles correspond to the bulk material, the nano-particle, γ - Si_3N_4 and SiTiN , and c-TiN , respectively. 63

Figure 5: SiTiN ternary composition diagram with the known binary subsystems and the novel ternary SiTiN phase located on the tie line between γ - Si_3N_4 and Ti_3N_4 65

Figure 6: (a) Lowest-enthalpy structure of $\text{Si}_{21}\text{Ti}_3\text{N}_{32}$ and (b) its arrangement of fused TiN_6 -cluster. (c) Local environment of vacancy site in $\text{Si}_{21}\text{Ti}_3\text{N}_{31}$ exhibiting TiN_5V -octahedra (d) Lowest-enthalpy structure of $\text{Si}_{18}\text{Ti}_6\text{N}_{31}$ highlighting the chain of edge-sharing TiN_6 -/ TiN_5V -octahedra. Green spheres represent N, red and dark blue spheres tetrahedral and octahedral Si, respectively, and light blue (cyan) spheres Ti. 68

Table 1: Bulk modulus B, shear modulus G, and Vickers hardness H_V of Si_3N_4 and SiTiN compounds with the spinel structure type at ambient pressure using SCAN functional. 71

Table 2: Overview of HP-HT experiments with run number, assembly, pressure, temperature, heating duration and capsule materials. 75

Figure 7: SEM micrographs (run# HH112) showing (left) an overview of the sample pellet after HP-HT and (right) a fracture surface with spinel-type γ - Si_3N_4 and rock salt-type c-TiN crystals. XRD of crushed samples was obtained using synchrotron radiation at the high-resolution powder diffraction beamline P02.1 of PETRA-III, DESY, Hamburg. The XRD pattern was quantitatively analyzed by Rietveld refinement with the program GSAS-II[34]. 75

CHAPTER 4

Table 1: Lattice parameters a and b for graphene- $15\text{Si}_2\text{CO}_2$, graphene- $16\text{Si}_2\text{CO}_2$, and graphene-bilayer- SiO_2 optimized with different dispersion correction methods 86

Table 2: Work of adhesion (J/m^2) for graphite, graphene- $15\text{Si}_2\text{CO}_2$, graphene- $16\text{Si}_2\text{CO}_2$, and graphene-bilayer- SiO_2 87

Table 3: Interlayer equilibrium separation distance (d_0) in Å for graphite, graphene- $15\text{Si}_2\text{CO}_2$, graphene- $16\text{Si}_2\text{CO}_2$, and graphene-bilayer- SiO_2 88

Table 4: Changes in Bader charges (e^-) ($q_{\text{compound}} - q_{\text{isolated-component}}$) for each component of the compound graphene- $\text{SiO}_2/\text{Si}_2\text{CO}_2$ systems optimized within DFT-ulg. Positive

values indicate charge accumulation in the compound model and negative values indicate charge depletion 89

PART II

CHAPTER 1

Figure 1: Models of $\text{Si}_2\text{CO}_2 + \text{C}_{\text{free}}$ (24,576 atoms) generated at $T_{\text{max}} = 4000$ K with a. density $\rho = 1.4 \text{ g/cm}^3$ and b. $\rho = 2.2 \text{ g/cm}^3$. Models from a. and b. shown without Si and O atoms and only C atoms with c. $\rho = 1.4 \text{ g/cm}^3$ and b. $\rho = 2.2 \text{ g/cm}^3$. C content $\text{C}_{\text{free}}:\text{Si} = 0.5$, density ρ , $T_{\text{max}} = 4000$ K. Si atoms are blue, O atoms are red, and C atoms are black. 102

Figure 2: (Left) Shear modulus and (right) Young's modulus vs. density ρ for models with content $\text{C}_{\text{free}}:\text{Si} = 1$ and composition $\text{Si}_5\text{CO}_8 + 5\text{C}_{\text{free}}$, $\text{SiO}_2 + \text{C}_{\text{free}}$, and $\text{Si}_2\text{CO}_2 + 2\text{C}_{\text{free}}$ generated at $T_{\text{max}} = 3000$ K. Elastic constants are calculated in triplicate for each of 3 independently generated models. Error bars (if larger than the symbol used) represent standard error. Simulations are done at 300 K. Lines are provided to guide the eye. 103

Figure 3: (a) Shear modulus and (b) Young's modulus for models with C content $\text{C}_{\text{free}}:\text{Si} = 0.5$, density $\rho = 2.2 \text{ g/cm}^3$, and composition $\text{SiO}_2 + 0.5\text{C}_{\text{free}}$, $\text{Si}_5\text{CO}_8 + 2.5\text{C}_{\text{free}}$, and $\text{Si}_2\text{CO}_2 + \text{C}_{\text{free}}$ generated using $T_{\text{max}} = 4000$ K. Elastic constants are calculated in triplicate for each of 3 independently generated models. Error bars represent standard error. Lines are provided to guide the eye. 104

Figure 4: a. Shear modulus and b. Young's modulus vs free carbon content, $\text{C}_{\text{free}}:\text{Si}$ ratio n , for models of $\text{Si}_5\text{CO}_8 + 5n\text{C}_{\text{free}}$, $\text{SiO}_2 + n\text{C}_{\text{free}}$, $\text{Si}_2\text{CO}_2 + 2n\text{C}_{\text{free}}$ generated at $T_{\text{max}} = 3000$ K with $\rho = 2.2 \text{ g/cm}^3$. C content $\text{C}_{\text{free}}:\text{Si}$ n , density $\rho = 2.2 \text{ g/cm}^3$, $T_{\text{max}} = 3000$ K. Elastic constants are calculated in triplicate for each of 3 independently generated models. Error bars (if larger than the symbol) represent standard error. Simulations are done at 300 K. Lines are provided to guide the eye. 106

Figure 5: a. Shear modulus and b. Young's modulus of $\text{Si}_5\text{CO}_8 + 10\text{C}_{\text{free}}$ models (39,360 atoms, $a=7.9 \text{ nm}$, 2.2 g/cm^3) generated at $T_{\text{max}} = 4000$ K. C content $\text{C}_{\text{free}}:\text{Si} = 0.5, 1, 2, 3$, density $\rho = 2.2 \text{ g/cm}^3$, $T_{\text{max}} = 4000$ K. Elastic constants are calculated in triplicate for each of 3 independently generated models. Error bars represent standard error. Lines are provided to guide the eye. 108

Figure 6: $\text{Si}_5\text{CO}_8 + 10\text{C}_{\text{free}}$ models (39,360 atoms; $a=7.9$ nm; 2.2 g/cm³) annealed at a. 2000 K, b. 4000 K, c. 6000 K, d. 8000 K. C content $\text{C}_{\text{free}}:\text{Si} = 2$, density $\rho = 2.2$ g/cm³, T_{max} . Only C atoms (black) are shown. 110

Figure 7: Young's modulus plotted as a function of T_{max} used in model generation. $\text{Si}_5\text{CO}_8 + 5n\text{C}_{\text{free}}$ models with $\rho = 2.2$ g/cm³ and $\text{C}_{\text{free}}:\text{Si} = n$, with $n = 0.5, 1, 2$, and 3 . Elastic constants are calculated in triplicate for each of 3 independently generated models. Error bars represent standard error. Simulations are done at 300 K. Lines are provided to guide the eye. 111

Figure 8: Young's modulus vs. simulation temperature for models of $\text{Si}_5\text{CO}_8 + 5n\text{C}_{\text{free}}$ annealed between 2000 K – 8000 K with a. $n = 0.5$, b. $n = 1.0$, c. $n = 2.0$, d. $n = 3.0$ where $n = \text{C}_{\text{free}} : \text{Si}$. density $\rho = 2.2$ g/cm³, T_{max} . Elastic constants are calculated in triplicate for each of 3 independently generated models. Error bars represent standard error. Lines are provided to guide the eye. 112

Figure 9: $\text{Si}_5\text{CO}_8 + 10\text{C}_{\text{free}}$ with $\text{C}_{\text{free}}:\text{Si} = 2$ and density $\rho = 2.2$ g/cm³) generated at a. $T_{\text{max}} = 6000$ K and b. $T_{\text{max}} = 8000$ K. The models comprise about 2.5 million atoms within a simulation box of approximately 40 nm. 114

Figure 10: Young's modulus of $\text{Si}_5\text{CO}_8 + 10\text{C}_{\text{free}}$ ($\text{C}_{\text{free}}:\text{Si} = 2$, density $\rho = 2.2$ g/cm³) as a function of simulation temperature for models of different size attained at a. $T_{\text{max}} = 2000$ K and b. $T_{\text{max}} = 8000$ K. A unit cell of a 10 nm model contains 39,360 atoms, a 20 nm model contains 314,880 atoms, and a 40 nm model contains 2,519,040 atoms. Three models each are generated for 10 and 20 nm, while only a single model is generated with a size of 40 nm. Elastic constant calculations for all models are done in triplicate. Error bars represent standard error. Lines are provided to guide the eye. 115

CHAPTER 2

Figure 1: $\text{Si}_5\text{CO}_8 + 10\text{C}_{\text{free}}$ (314,880 atoms; 144,320 C atoms; $a = 15.8$ nm; $\rho = 2.2$ g/cm³). Generated at T_{max} equals a. 2000 K, b. 4000 K, c. 6000 K, and d. 8000 K. Only C atoms (black) are shown. 123

Figure 2: Topological shell counting method applied to carbon atoms in $\text{Si}_5\text{CO}_8 + 10\text{C}_{\text{free}}$ generated at $T_{\text{max}} = 2000$ K, 4000 K, 6000 K, and 8000 K. The topological shell counting method is averaged over the results of three models for each T_{max} 124

CHAPTER 3

Figure 1: Energy correspondence between ReaxFF and DFT energy differences for $15\text{SiC} + 3\text{Si}_3\text{N}_4$ ($\text{Si}_3\text{N}_4:\text{SiC} = 0.2$). Static energies are calculated within ReaxFF without relaxation of DFT-optimized structures, and minimized energies are calculated within ReaxFF after constant volume optimization of DFT-optimized structures within ReaxFF. Energies are relative to the lowest energy Si-C-N structure calculated with the corresponding method (Reference structure ReaxFF energies before minimization: -6.07 eV/atom and after minimization: -6.38 eV/atom). The ideal 1:1 energy correspondence is indicated with a dashed line. 132

Figure 2: a. Infinite single strand of Ceraset $\text{Si}_{15}\text{C}_{21}\text{N}_{15}\text{H}_8$ ($a=21 \text{ \AA}$; $\rho = 0.17 \text{ g/cm}^3$) b. $4 \times 4 \times 4$ supercell of single strand of Ceraset $\text{Si}_{960}\text{C}_{1344}\text{N}_{960}\text{H}_{5184}$ ($a=84 \text{ \AA}$, $\rho = 0.17 \text{ g/cm}^3$). Blue atoms are Si, green balls atom N, black atoms are C, and pink atoms are H. Models displayed with CrystalMaker[34]. 133

Figure 3: Ceraset $\text{Si}_{960}\text{C}_{1344}\text{N}_{960}\text{H}_{5184}$ at 900 K after constant pressure simulation up to 3000 K ($a=54.6 \text{ \AA}$, $\rho = 0.63 \text{ g/cm}^3$) with a. all atoms displayed and b. methane removed from display. Models displayed with CrystalMaker[34]. 134

LIST OF ABBREVIATIONS

DFT: Density functional theory
MD: Molecular dynamics
ReaxFF: Reactive force field
ccp: Cubic-closest packing
hcp: Hexagonal closest packing
VASP: Vienna ab initio Simulation Package
PBE: Perdew, Burke, Ernzerhof generalized gradient approximation functional
SCAN: Strongly Constrained and Appropriately Normed
PAW: Projector-augmented wave
SpGr/S.G.: Space group
HV-HT: High-pressure, high-temperature
LVP: Large volume press
SnNO: $\text{Sn}_2\text{N}_2\text{O}$
XRD: X-ray diffraction
ADT: Automated diffraction tomography
EDX: Energy-dispersive X-ray spectroscopy
2D: Two-dimensional
3D: Three-dimensional
FWHM: Full width half maximum
CN: Coordination number
HSE06/HSE: Heyd-Scuseria-Ernzerhof exchange correlation functional
PBE0: Mixture of Perdew, Burke, Ernzerhof exchange and correlation energies and Hartree-Fock exchange energy
DAC: Diamond anvil cell
CuK α : Copper K- α
NED: Nanoelectron-diffraction
SiTiN: Silicon titanium nitride
SSP: Single-source precursor
PHPS: Perhydropolysilazane
TDMAT: Tetrakis(dimethylamido)titanium

PHTiPS5: Polytitanosilazane

SEM-EDS: Scanning electron microscopy and energy dispersive X-ray spectroscopy

ADF-STEM: Annular dark-field imaging in scanning transmission electron microscope

EELS: Electron energy loss spectroscopy

STEM: Scanning transmission electron microscopy

STEM-EDX: Energy dispersive X-ray tomography in scanning transmission electron microscope

TEM: Transmission electron microscopy

SEM: Scanning electron microscopy

DFT-ulg: Universal low gradient van der Waals correction method

DFT-TS: Tkatchenko-Scheffler van der Waals correction method

DFT-vdW-DF: Nonlocal van der Waals density functional of Dion et al.

DFT-vdW-DF2-B86R: Nonlocal van der Waals density functional of Hamada

DFT-D2: Grimme's D2 van der Waals correction method

SiCO: Silicon oxycarbide

PDC: Polymer-derived ceramic

CMC: Ceramic matrix composite

T_{\max} : maximum temperature used during simulation

WWW: Wooten, Winer, and Waire algorithm

aiMD: ab initio molecular dynamics

LAMMPS: Large-scale Atomic/Molecular Massively Parallel Simulator

INTRODUCTION

With advances in computing power, the field of computational chemistry has flourished. Using current computational resources, atomistic simulations of billion atoms[1] and trillions of atoms[2] have been performed. Computational techniques can be used to support experimental investigations into new materials as well as independently predict the existence of new materials. Investigations with computations have been used to study a variety of different phenomena from the band structure of the tetracyanoplatinate chain[3] to DNA-carbon nanotube hybrids[4] to the F₁-ATPase mechanism[5].

Density functional theory (DFT) is one of the most popular methods used in computational chemical physics[6]. DFT is an electronic structure theory formulated on the principle that the ground-state properties of a system are a function of its total electron density sidestepping the many-electron wave function[7]. Work by Car and Parrinello[8] paved the way for the use of DFT in molecular dynamics simulations.

In spite of DFT general's accuracy and its general applicability, the computational expense of DFT is substantial and simulations exceeding thousands of atoms are not routinely feasible. For investigations where the quantum chemical accuracy of DFT can or must be spared, classical potentials have been developed that can study system sizes up to millions of times larger than DFT. The Tersoff potential is a classical potential where bond order is dependent on the local environment[9]. Although the applications of the Tersoff potential are limited, it can be used to study several properties including mechanical properties[10] and thermal conductivity[11].

In order to perform simulations with quantum chemical accuracy using system sizes approaching those used in empirical potential simulations, the reactive force field ReaxFF[12] was developed. ReaxFF can be trained to reproduce DFT accuracy[13] and perform simulations with system sizes surpassing the practical size limit of DFT. Compared to other classical potentials and force fields, ReaxFF is quite complex. The

system energy calculated by ReaxFF can depend on multiple terms including bond energy, over-coordination energy, under-coordination energy, valence angle energy, torsion angle energy, conjugation energy, and van der Waals energy[12]. However, the central principle of ReaxFF is that (nearly) every term depends smoothly on the bond order. Thus, ReaxFF features bond-breaking allowing for the investigation of chemical reactions.

The first part of this work focuses on DFT calculations of materials synthesized at high pressures and the work of adhesion in compound graphene-SiO₂/Si₂CO₂ systems.

Stishovite is an SiO₂ mineral with the rutile structure-type that is ultrahard[14] but can only be synthesized at high pressures[15, 16]. To predict alternative routes to synthesize stishovite, we investigate energetics of the well-known transformation between α -cristobalite, another SiO₂ mineral, and stishovite. By studying the reverse rutile-cristobalite transformation as well we also examine the formation of cristobalite forms of GeO₂ and TiO₂. From calculation of the activation barriers of the cristobalite-rutile transformation, we predict conditions for the synthesis of stishovite and cristobalite GeO₂ and TiO₂.

We also contribute to collaborations focused on synthesizing ternary materials in high-pressure experiments and characterizing them. Following the synthesis of a new *Pbcn*-Sn₂N₂O, we perform supporting enthalpy-pressure calculations in order to determine pressures at which *Pbcn*-Sn₂N₂O become favorable. Additionally, we contribute bulk modulus and band structure calculations of *Pbcn*-Sn₂N₂O. In the discovery of spinel-type ternary silicon titanium nitride, we provide calculations for elastic properties and electronic properties. Since the exact position of Si and Ti in spinel-type silicon titanium nitride is unknown, and Ti could occupy any of the Si sites from spinel-Si₃N₄, we used combinatorial analysis through DFT calculations to predict favorable sites for Ti placement. Using Bader charge analysis, we calculate Ti to be in two distinct oxidation states, Ti³⁺ and Ti⁴⁺.

Two-dimensional (2D) materials are being studied for further development of complementary metal-oxide-semiconductor (CMOS) technology[17]. Graphene is a 2D material with interesting properties including high carrier mobility[18] and high reversible capacity as lithium anodes[19]. We study the work of adhesion in potential anode systems in lithium-ion batteries consisting of graphene and a second component, either a bilayer-SiO₂ or a (001) SiC surface terminated with oxygen.

Part II is about investigations of amorphous ceramics, including polymer-derived ceramics, with classical methods. Polymer-derived ceramics are a class of advanced ceramics materials that have been under investigation for the last half century[20]. The composition of the ceramic depends on the composition of the starting polymer precursor. For pyrolysis temperatures between 1073 – 1573 K, ceramics (with excess free carbon) produced by the polymer-to-ceramic conversion process can be described as a mixture of an amorphous SiBCNO phase with an embedded “free carbon” phase. Although, there have been several experimental studies[21-23] investigating structural features of polymer-derived ceramics, the amorphous nature of PDCs preclude definitive structural characterization.

We study elastic properties of SiCO ceramics through classical molecular dynamics with the Tersoff potential. We examine how the elastic properties of SiCO ceramics depend on a variety of factors, including composition of the glass, free carbon content, density, and morphology of the free carbon phase. By independently varying parameters, we predict how free carbon content and density separately impact elastic properties. Additionally, we determine how the morphology of the free carbon phase can impact elastic properties.

In order to quantify free carbon morphology exhibited in atomistic models of amorphous ceramics, we develop a three-coordinated carbon topological shell counting method. We demonstrate how the topological shell counting method can be used to

determine the extent of the free carbon network and differentiate between amorphous ceramics with different free carbon morphologies.

Since the composition of PDCs depend on the starting polymer precursor and the method of processing during synthesis, we realize the need for investigation of the polymer-to-ceramic conversion process. We develop a new ReaxFF parameter set to study the polymer-to-ceramic conversion process of polysilazanes into amorphous SiCN ceramics. We start from parameters from Kulkarni et al.[24] and Ponomarev et al.[25] and train them on DFT calculations and ab initio molecular dynamics. The resulting parameter set is evaluated for good reproduction of the DFT potential energy surface for Si-C-N-H materials and we perform simulations of the polysilazane Ceraset.

References

- [1] J. Jung, C. Kobayashi, K. Kasahara, C. Tan, A. Kuroda, K. Minami, S. Ishiduki, T. Nishiki, H. Inoue, Y. Ishikawa, M. Feig, Y. Sugita, New parallel computing algorithm of molecular dynamics for extremely huge scale biological systems, 42(4) (2021) 231-241.
- [2] N. Tchipev, S. Seckler, M. Heinen, J. Vrabec, F. Gratl, M. Horsch, M. Bernreuther, C.W. Glass, C. Niethammer, N. Hammer, B. Krischok, M. Resch, D. Kranzlmüller, H. Hasse, H.-J. Bungartz, P. Neumann, TweTriS: Twenty trillion-atom simulation, 33(5) (2019) 838-854.
- [3] M.-H. Whangbo, R. Hoffmann, The band structure of the tetracyanoplatinate chain, Journal of the American Chemical Society 100(19) (1978) 6093-6098.
- [4] M.L. Mayo, Z.Q. Chen, S.V. Kilina, Computational Studies of Nucleotide Selectivity in DNA–Carbon Nanotube Hybrids, The Journal of Physical Chemistry Letters 3(19) (2012) 2790-2797.
- [5] K. Nam, J. Pu, M. Karplus, Trapping the ATP binding state leads to a detailed understanding of the F1-ATPase mechanism, 111(50) (2014) 17851-17856.
- [6] A.D. Becke, Perspective: Fifty years of density-functional theory in chemical physics, The Journal of Chemical Physics 140(18) (2014) 18A301.
- [7] P. Hohenberg, W. Kohn, Inhomogeneous Electron Gas, Physical Review 136(3B) (1964) B864-B871.
- [8] R. Car, M. Parrinello, Unified Approach for Molecular Dynamics and Density-Functional Theory, Physical Review Letters 55(22) (1985) 2471-2474.
- [9] J. Tersoff, New empirical approach for the structure and energy of covalent systems, Physical Review B 37(12) (1988) 6991-7000.
- [10] Y.-Y. Zhang, Q.-X. Pei, Z.-D. Sha, Y.-W. Zhang, A molecular dynamics study of the mechanical properties of h-BCN monolayer using a modified Tersoff interatomic potential, Physics Letters A 383(23) (2019) 2821-2827.

- [11] Z. Fan, Y. Wang, X. Gu, P. Qian, Y. Su, T. Ala-Nissila, A minimal Tersoff potential for diamond silicon with improved descriptions of elastic and phonon transport properties, *Journal of Physics: Condensed Matter* 32(13) (2019) 135901.
- [12] A.C.T. van Duin, S. Dasgupta, F. Lorant, W.A. Goddard, ReaxFF: A Reactive Force Field for Hydrocarbons, *The Journal of Physical Chemistry A* 105(41) (2001) 9396-9409.
- [13] S.G. Srinivasan, A.C.T. van Duin, P. Ganesh, Development of a ReaxFF Potential for Carbon Condensed Phases and Its Application to the Thermal Fragmentation of a Large Fullerene, *The Journal of Physical Chemistry A* 119(4) (2015) 571-580.
- [14] J.M. Léger, J. Haines, M. Schmidt, J.P. Petit, A.S. Pereira, J.A.H. da Jornada, Discovery of hardest known oxide, *Nature* 383 (1996) 401.
- [15] P.S. De Carli, D.J. Milton, Stishovite: Synthesis by Shock Wave, 147(3654) (1965) 144-145.
- [16] P. Mohanty, D. Li, T. Liu, Y. Fei, K. Landskron, Synthesis of Stishovite Nanocrystals from Periodic Mesoporous Silica, *Journal of the American Chemical Society* 131(8) (2009) 2764-2765.
- [17] A.C. Ferrari, F. Bonaccorso, V. Fal'ko, K.S. Novoselov, S. Roche, P. Bøggild, S. Borini, F.H.L. Koppens, V. Palermo, N. Pugno, J.A. Garrido, R. Sordan, A. Bianco, L. Ballerini, M. Prato, E. Lidorikis, J. Kivioja, C. Marinelli, T. Ryhänen, A. Morpurgo, J.N. Coleman, V. Nicolosi, L. Colombo, A. Fert, M. Garcia-Hernandez, A. Bachtold, G.F. Schneider, F. Guinea, C. Dekker, M. Barbone, Z. Sun, C. Galiotis, A.N. Grigorenko, G. Konstantatos, A. Kis, M. Katsnelson, L. Vandersypen, A. Loiseau, V. Morandi, D. Neumaier, E. Treossi, V. Pellegrini, M. Polini, A. Tredicucci, G.M. Williams, B. Hee Hong, J.-H. Ahn, J. Min Kim, H. Zirath, B.J. van Wees, H. van der Zant, L. Occhipinti, A. Di Matteo, I.A. Kinloch, T. Seyller, E. Quesnel, X. Feng, K. Teo, N. Rupesinghe, P. Hakonen, S.R.T. Neil, Q. Tannock, T. Löfwander, J. Kinaret, Science and technology roadmap for graphene, related two-dimensional crystals, and hybrid systems, *Nanoscale* 7(11) (2015) 4598-4810.
- [18] S.V. Morozov, K.S. Novoselov, M.I. Katsnelson, F. Schedin, D.C. Elias, J.A. Jaszczak, A.K. Geim, Giant Intrinsic Carrier Mobilities in Graphene and Its Bilayer, *Physical Review Letters* 100(1) (2008) 016602.
- [19] H.F. Xiang, Z.D. Li, K. Xie, J.Z. Jiang, J.J. Chen, P.C. Lian, J.S. Wu, Y. Yu, H.H. Wang, Graphene sheets as anode materials for Li-ion batteries: preparation, structure, electrochemical properties and mechanism for lithium storage, *RSC Advances* 2(17) (2012) 6792-6799.
- [20] W. Verbeek, Production of shaped articles of homogeneous mixtures of silicon carbide and nitride, Bayer Aktiengesellschaft, United States, 1973.
- [21] H.-J. Kleebe, G. Gregori, F. Babonneau, Y.D. Blum, D.B. MacQueen, S. Masse, Evolution of C-rich SiOC ceramics: Part I. Characterization by integral spectroscopic techniques: Solid-state NMR and Raman spectroscopy: Dedicated to Professor Dr. Fritz Aldinger on the occasion of his 65th birthday, *International Journal of Materials Research* 97(6) (2006) 699-709.
- [22] Y. Cao, X. Yang, L. An, Electric conductivity and microstructure evolution of polymer-derived SiAlCO ceramics, *Ceramics International* 42(3) (2016) 4033-4038.
- [23] S. Sarkar, Z. Gan, L. An, L. Zhai, Structural Evolution of Polymer-Derived Amorphous SiBCN Ceramics at High Temperature, *The Journal of Physical Chemistry C* 115(50) (2011) 24993-25000.

- [24] A.D. Kulkarni, D.G. Truhlar, S. Goverapet Srinivasan, A.C.T. van Duin, P. Norman, T.E. Schwartzenruber, Oxygen Interactions with Silica Surfaces: Coupled Cluster and Density Functional Investigation and the Development of a New ReaxFF Potential, *The Journal of Physical Chemistry C* 117(1) (2013) 258-269.
- [25] I. Ponomarev, A.C.T. van Duin, P. Kroll, Reactive Force Field for Simulations of the Pyrolysis of Polysiloxanes into Silicon Oxycarbide Ceramics, *The Journal of Physical Chemistry C* 123(27) (2019) 16804-16812.

PART I: HIGH-PRESSURE AND MATERIALS CHEMISTRY

CHAPTER 1: PAVING THE WAY FOR CRISTOBALITE TiO_2 AND GeO_2
ATTAINABLE UNDER MODERATE TENSILE STRESS: A DFT STUDY OF
TRANSFORMATION PATHS AND ACTIVATION BARRIERS IN CRISTOBALITE-
RUTILE TRANSFORMATIONS OF MO_2 ($\text{M} = \text{Si}, \text{Ge}, \text{Ti}$)

Motivation and Scope

There are several different polymorphs of SiO_2 including α -quartz, β -quartz, coesite, α -cristobalite, stishovite, and seifertite. Of the SiO_2 polymorphs, stishovite is a high-pressure polymorph noted for being ultrahard[1]. The synthesis of stishovite requires significantly high pressures[2, 3]. We investigate the transformation between α -cristobalite- SiO_2 and stishovite- SiO_2 , which exhibits the rutile-structure type.

Additionally, we extend the investigation to GeO_2 and TiO_2 , which are found in the rutile-type at ambient pressures. Using two different concerted mechanisms to describe the cristobalite-rutile transformation we calculate activation barriers between the two structure types for SiO_2 , GeO_2 , and TiO_2 . We assess the impact of external pressure on the activation energies associated with the cristobalite-to-rutile transformation.

References

- [1] J.M. Léger, J. Haines, M. Schmidt, J.P. Petitet, A.S. Pereira, J.A.H. da Jornada, Discovery of hardest known oxide, *Nature* 383 (1996) 401.
- [2] P.S. De Carli, D.J. Milton, Stishovite: Synthesis by Shock Wave, 147(3654) (1965) 144-145.
- [3] P. Mohanty, D. Li, T. Liu, Y. Fei, K. Landskron, Synthesis of Stishovite Nanocrystals from Periodic Mesoporous Silica, *Journal of the American Chemical Society* 131(8) (2009) 2764-2765.

Paving the way for cristobalite TiO_2 and GeO_2 attainable under moderate tensile stress: a DFT study of transformation paths and activation barriers in cristobalite-rutile transformations of MO_2 ($\text{M} = \text{Si, Ge, Ti}$)

Shariq Haseen and Peter Kroll*

Department of Chemistry and Biochemistry, The University of Texas at Arlington,
700 Planetarium Place, Arlington, Texas 76019, United States.

* Corresponding author: pkroll@uta.edu

Abstract

We investigate energetics of interconversions between cristobalite-type and rutile-type structures of SiO_2 , GeO_2 , and TiO_2 at different pressures within Density Functional Theory. Cristobalite- SiO_2 is succeeded by the rutile-type, stishovite- SiO_2 , at high pressures. The rutile-types of GeO_2 and TiO_2 are favored at ambient pressure, but small tensile stresses are sufficient to yield cristobalite- GeO_2 and TiO_2 . The transition from one structure-type into the other is modeled using collective movements of cations or anions with different degrees of freedom for the remaining structure parameters. We find that increasing the external pressure decreases activation barriers of the cristobalite-rutile transformation. Activation barriers of the reverse transformation from rutile to cristobalite decrease with decreasing pressure. If only a fraction of cations follows the collective movement we find even lower activation barriers. The final states are still tetrahedrally or octahedrally coordinated structures, albeit not the high-symmetry variants of cristobalite or rutile, respectively. The small tensile stresses needed to favor cristobalite- GeO_2 and TiO_2 over their respective rutile counterparts, and the low

activation barriers involved in their interconversion let us propose a simple route to synthesize cristobalite-GeO₂ and a new cristobalite-TiO₂.

Introduction

Transformations between structures described using the concepts cubic-closest packing (ccp) and hexagonal closest packing (hcp) are standard topics in metallurgy and crystal chemistry.[1] Many of them proceed or are activated at high temperature and/or high pressure. A particular example is the transformation between cristobalite-type and rutile-type structures. Anions in cristobalite are approximately ccp with cations filling tetrahedral interstitials while those in rutile are approximately hcp with cations in octahedral interstitials. The binary oxides silica (SiO₂) and germania (GeO₂) both exhibit cristobalite-type and rutile-type polymorphs.[2-7] SiO₂ α-cristobalite has many industrial uses[8] and stishovite is one of the hardest known oxides.[9] A natural source for GeO₂ cristobalite has not been discovered so far, but synthesis of GeO₂ cristobalite has been reported.[5-7] However, extensive characterization of GeO₂ cristobalite has not been reported, and its existence as a pure phase has even been disputed.[10] Rutile GeO₂ is the most stable GeO₂ polymorph at ambient conditions and has potentially useful optical properties.[11]. The eponymous rutile is a polymorph of titania (TiO₂)[12] and well-known for its use as white pigment[13, 14] Additional applications range from (photo)catalysis to energy storage.[15, 16] A cristobalite-TiO₂ has not yet been synthesized or found in nature.

Previous studies investigated the transformation between SiO₂ cristobalite and stishovite. O’Keefe and Hyde proposed a reaction mechanism by which α-cristobalite transforms to rutile-type via rotation of SiO₄ tetrahedra and simultaneous displacement of cations and anions.[17] This path was studied later by Silvi et al. using Hartree-Fock calculations.[18] Klug et al. were the first to simulate the pressure-induced transformation from cristobalite to stishovite using ab initio constant pressure molecular

dynamics (MD).[19] Analysis of atomic trajectories during the transformation revealed a smooth structural evolution from cristobalite to stishovite similar to the transition path proposed by O’Keefe and Hyde. No intermediate structure of lower symmetry was reported. Huang et al. used a very similar method to study the transition in dynamic simulations.[20] Their study corroborated the transition path of O’Keefe and Hyde but indicated unquenchable intermediate structures along the pathway. Salvadó et al. followed the cristobalite-rutile transformation for SiO₂ within Density Functional Theory (DFT) using a common sub-group and applied a concerted movement of cations along the proposed transition path.[21] Their study yielded a smooth energy profile without intermediate local minima. We had previously performed a similar study of the cristobalite-rutile transition in SiO₂, TiO₂, and Cu₂O (the anti-form) but followed a concerted movement of anions along the proposed transition path instead.[22]

The goal of this paper is to provide a comparative study of the transformation from cristobalite to rutile for SiO₂, GeO₂, and TiO₂. We provide transition pressures and compare enthalpy profiles and activation energies for the concerted movements by cations and by anions. We indicate that intermediate structures may occur if only a fraction of cations move in a concerted way. Anticipating our results, we will show for both GeO₂ and TiO₂ that transformation from a rutile structure to cristobalite requires only moderate tensile stresses, and experimental realization should be feasible.

Method

All calculations are done within Density Functional Theory as implemented in the Vienna *ab initio* Simulation Package (VASP).[23-26] For electron exchange and correlation we use the Generalized Gradient Approximation as parametrized by Perdew, Burke, and Ernzerhof (PBE).[27, 28] For comparison, we apply the Strongly Constrained and Appropriately Normed (SCAN) functional.[29] Atom cores are described through the projector augmented wave (PAW) method.[30, 31] A 4×4×4 mesh is used for all

structures to sample the Brillouin zone.[32] Energies are converged to 0.01 meV/atom and forces to 5 meV/Å.

After optimization of structures we compute the energy of each model for a series of volumes around the minimum configuration. At each step the structure is optimized under the constraint of constant volume. The resulting energy-volume data for each structure is transformed into enthalpy-pressure data by numerically differentiating a spline fit to the data. Points of equal enthalpy then define the transition pressure p_t of the transition from the α -cristobalite-type to the rutile-type. In the case of SiO_2 , p_t is positive, while for GeO_2 and TiO_2 p_t is negative.

Structures and Transition paths

The structure of α -cristobalite MO_2 ($\text{M}=\text{Si}, \text{Ge}, \text{Ti}$) is built up by corner-connected MO_4 tetrahedra. Its topology resembles that of the diamond network, with two-connected O atoms bridging between vertices of the diamond structure. The O atoms in α -cristobalite fall, approximately, on sites of a cubic-closest-packed structure. For SiO_2 and GeO_2 the optimized α -cristobalite structure exhibits bending of the angle at O, while for TiO_2 the bond angle is almost 180° . Hence, TiO_2 optimizes towards the (ideal) α -cristobalite structure.[33] The rutile structure, as realized in stishovite- SiO_2 as well as rutile- GeO_2 and TiO_2 , comprises MO_6 -octahedra sharing edges. O atoms are three-fold coordinated and fall, approximately, on sites of a hexagonal-closest packed structure.

With their resemblance to ccp (cristobalite) and hcp (rutile), a simple transformation path between cristobalite and rutile can be constructed following standard concepts of metallurgy and crystal chemistry.[17] Using a common space group $C222_1$ (20), the two structures can be described using the parameters shown in Table 1.

Using the common space group representation with correspondence between the structure parameters, lattice parameters and coordinates, a transformation between

cristobalite and rutile is facilitated by interpolating the structure parameters between the two structures.

Table 1: Generic description of lattice parameters and coordinates of cristobalite-type and rutile-type structures using the common space group $C222_1$ (20). The choice of parameters (e.g. 1 rather than 0) allows to describe the transition between of cristobalite and rutile by interpolation between the respective parameters.

a,b,c	a_c	a_c	c_c	a_s	a_s	c_s
	x	y	z	x	y	z
Si1	0	$y_c\text{Si}$	1/4	0	1/2	1/4
Si2	$y_c\text{Si}+1/2$	0	0	1	0	0
O1	$x_c\text{O}$	$y_c\text{O}$	$z_c\text{O}$	0	$y_s\text{O}$	1/2
O2	$y_c\text{O}$	$1/2 - x_c\text{O}$	$z_c\text{O}-1/4$	$y_s\text{O}$	1/2	1/4

The interpolation can happen in different ways, for example by linear interpolation of all parameters simultaneously.[17] Two other modes of concerted movement of all atoms are studied here. In the “anion method,” positions of the anions as well as cell parameters are linearly interpolated between cristobalite and rutile. The cations are allowed to optimize, conforming to each new configuration. Previously, we had investigated this path for the transformation in SiO_2 . [22] In the “cation method”, positions of cations are linearly interpolated between initial and final configurations, while the anions are allowed to optimize, conforming to each new configuration. In addition, at each intermediate step the cell parameters are allowed to optimize according to the given constraints. This approach has recently been investigated for transitions in SiO_2 by Salvadó et al.[21] Note that the paths described above retain space group $C222_1$ during the transformation.

“Cation method” and “anion method” are barely distinguishable by looking at intermediate structure. However, the computed energy profiles are noticeably different as we will discuss further below. For both approaches we use 19 intermediate configurations. The small step size between intermediates guarantees a smooth connection and no significant jumps of atoms from one optimized step to the next one.

The concerted movement of atoms as described above causes a rotation of MO_4 tetrahedra in cristobalite. This goes along with their slight deformation and, due to the volume contraction and increasing density, with the approach of two additional anions towards the cation center, see Figure 1. This forms MO_6 octahedra characteristic for the rutile structure. Note that on the path from cristobalite to rutile no bond is broken, but two additional bonds per cation are formed. Conversely, the reverse path from rutile to cristobalite breaks two Si-O bonds.

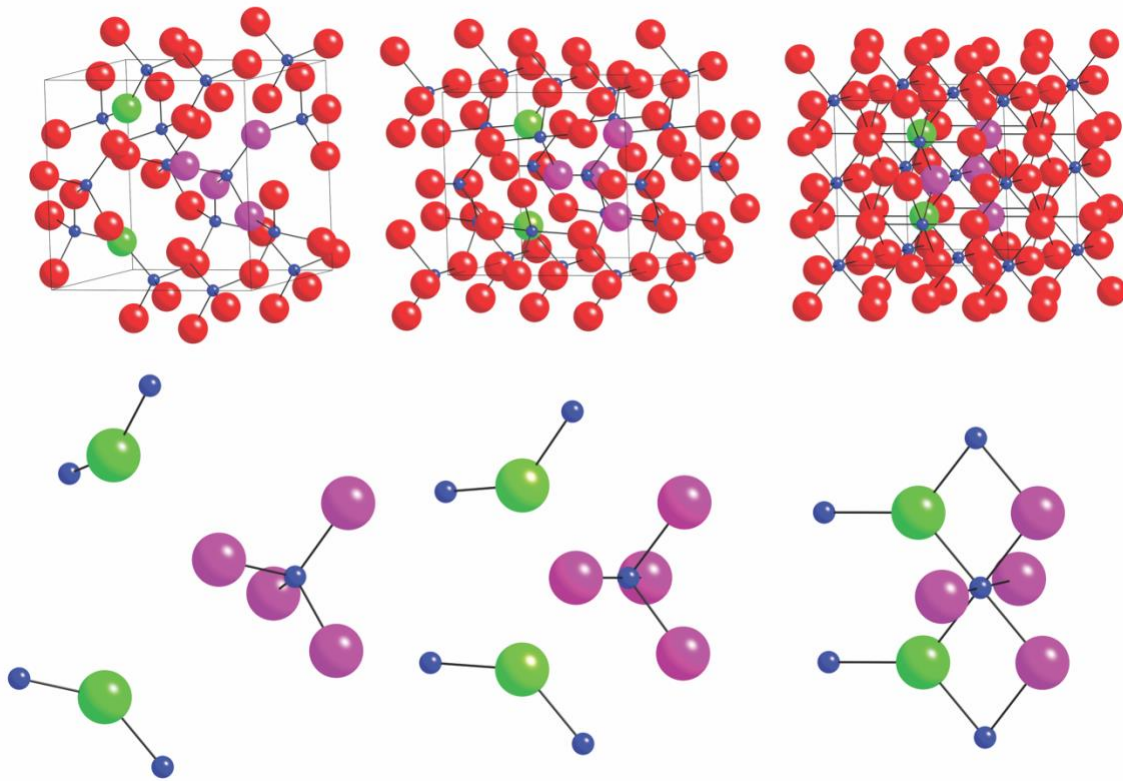


Figure 1: Initial (top left), intermediate (top middle) and final (top right) step of the transformation path from cristobalite to rutile. The orthorhombic common unit cell (SpGr. $C222_1$) is outlined. Si atoms are blue and O atoms are red. For one Si we highlight its initially four (4) coordinating oxygen neighbors (purple) and the two additional oxygen (green) approaching it to form the final SiO_6 -octahedron. Enlarged views of the forming octahedral SiO_6 during the transformation are shown directly beneath the corresponding step in the transformation path.[34]

Table 2: Lattice parameters and internal parameters of $C222_1$ cristobalite-type and rutile-type SiO_2 , GeO_2 , TiO_2 from structures optimized with PBE and SCAN functionals.

^a[35], ^b[36], ^c[37], ^d[38], ^e[39]

		<u>cristobalite-type</u>				<u>rutile-type</u>		
		Exp.	PBE	SCAN		Exp.	PBE	SCAN
<u>SiO_2</u>	a_c (Å)	7.0400 ^a	7.2270	7.0680	a_s (Å)	5.9110 ^c	5.9900	5.9140
	c_c (Å)	6.9321 ^a	7.1520	6.9580	c_s (Å)	5.3338 ^c	5.3880	5.3400
	$y_c\text{Si}$	0.3008 ^a	0.2909	0.3000				
	$x_c\text{O}$	0.0680 ^a	0.0777	0.0679				
	$y_c\text{O}$	0.1719 ^a	0.1646	0.1714	$y_s\text{O}$	0.30613 ^c	0.3069	0.3064
	$z_c\text{O}$	0.4287 ^a	0.4207	0.4282				
<u>GeO_2</u>	a_c (Å)	7.06 ^b	7.2240	7.0160	a_s (Å)	6.2177 ^d	6.3690	6.2530
	c_c (Å)	7.06 ^b	7.3870	7.1800	c_s (Å)	5.7252 ^d	5.8580	5.7800
	$y_c\text{Ge}$	0.328 ^b	0.3201	0.3291				
	$x_c\text{O}$	0.0445 ^b	0.0324	0.0244				
	$y_c\text{O}$	0.211 ^b	0.1945	0.2002	$y_s\text{O}$	0.3063 ^d	0.3067	0.3058
	$z_c\text{O}$	0.465 ^b	0.4562	0.4594				
<u>TiO_2</u>	a_c (Å)		8.4740	8.4210	a_s (Å)	6.49641 ^e	6.5980	6.5200
	c_c (Å)		8.4680	8.4230	c_s (Å)	5.91736 ^e	5.9390	5.9130
	$y_c\text{Ti}$		1/2	1/2				
	$x_c\text{O}$		0.1203	0.1225				
	$y_c\text{O}$		0.1295	0.1274	$y_s\text{O}$	0.3048 ^e	0.3048	0.3042
	$z_c\text{O}$		0.3796	0.3775				

Results and discussions

Optimizing the structures using PBE and SCAN functionals yields parameters listed in Table 2. Energy and energy differences between the optimized (local) ground state structures as well as computed transition pressures are given in Table 3.

Comparing results achieved with both functionals, we note that the SCAN functional appears to “favor” higher coordination of cations in the octahedrally coordinated structure. For instance, α -cristobalite- SiO_2 is more favorable than stishovite (which is rutile- SiO_2). Within PBE the energy difference is 0.58 eV/ SiO_2 , while using SCAN this comes up to only 0.39 eV/ SiO_2 . For both GeO_2 and TiO_2 the rutile structure is more favorable than the cristobalite-type. Computed energy differences for GeO_2 are

Table 3: Optimized energies of cristobalite-type and rutile-type SiO_2 , GeO_2 , and TiO_2 at ambient pressure, energy differences ΔE from cristobalite-type to rutile-type, and computed transition pressures p_t found using PBE and SCAN functionals

	cristobalite-type (eV/f.u.)	rutile-type (eV/f.u.)	ΔE (eV/f.u.)	p_t (GPa)
PBE				
SiO_2	-23.74	-23.16	0.58	5.4
GeO_2	-19.01	-19.17	-0.16	-1.4
TiO_2	-26.32	-26.41	-0.09	-0.4
SCAN				
SiO_2	-31.57	-31.21	0.36	3.2
GeO_2	-36.52	-36.93	-0.41	-3.3
TiO_2	-37.53	-38.05	-0.52	-1.9

-0.16 eV/ GeO_2 (PBE) and -0.41 eV/ GeO_2 (SCAN), and for TiO_2 they are -0.09 eV/ TiO_2 (PBE) and -0.52 eV/ TiO_2 (SCAN). Consequently, transition pressures p_t computed by computed using PBE are systematically 1.5 to 2 GPa higher than transition pressures SCAN (see Table 3).

The reason for reduced transition pressures is related to the (partial) inclusion of short range van-der-Waals interactions in SCAN.[40] This is corroborated by adding van-der-Waals interactions to the PBE functional. We choose the universal low gradient correction (ulg) together with the PBE functional, thus performing PBE+ulg calculations.[41] For the α -cristobalite to stishovite of SiO_2 we then receive a transition pressure of 2.0 GPa, even lower than for SCAN (3.2 GPa) and significantly reduced in comparison to “standard” PBE calculations (5.4 GPa). Very similar trends are found for GeO_2 and TiO_2 as well.

We present the energy-volume graphs for SiO_2 , GeO_2 , and TiO_2 computed using PBE and SCAN in Fig. 2. It is apparent for each compound that the rutile-type structure has a higher curvature around the energy minimum than the cristobalite-type. Therefore, the rutile-type structure is less compressible. The very shallow E-V curve of the cristobalite-type is indicative of the shallow potential energy surface for bending the

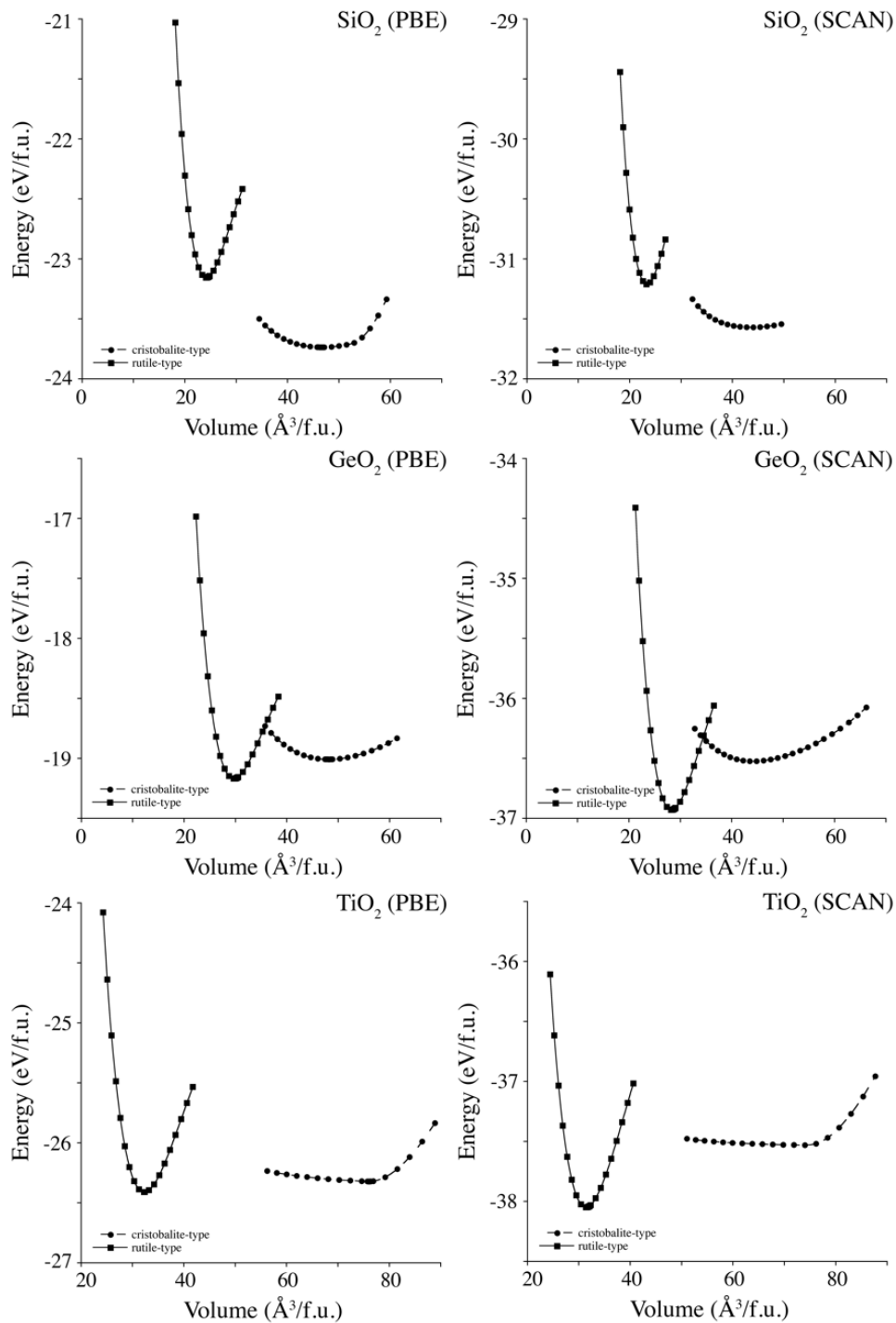


Figure 2: E-V diagrams with quantities given per formula unit (f.u.) for cristobalite-type and rutile-type SiO_2 , GeO_2 , and TiO_2 using PBE (left) and SCAN (right) functionals.

M-O-M bond angle at O.[42] Converting the energy-volume (E-V) data into relative enthalpy-pressure (ΔH -p) diagrams computed yields the diagrams shown in Figure 3, from which we determine transition pressures as collected in Table 3.

Our results for the cristobalite-stishovite transition are aligned with previous studies, which found a transition pressure of 5–6 GPa.[18, 21, 22] Experimentally, a conversion from cristobalite to stishovite is feasible between 10 and 15 GPa, but intermediate phases may appear depending on exact temperature-pressure conditions.[43-45]

Since for both GeO_2 and TiO_2 the rutile structure is more favorable at ambient pressure, we compute negative pressures for a transition from rutile to cristobalite. In the case of GeO_2 values of p_t are -1.4 GPa (PBE) and -3.3 GPa (SCAN). Saito and Ono previously computed polymorphs of GeO_2 and their data yields $p_t \approx -6$ GPa.[46] Yamaguchi et al. reported that cristobalite- GeO_2 transforms into rutile- GeO_2 through just grinding of the material.[7] On the other side, rutile- GeO_2 transforms into α -quartz- GeO_2 at 1340 K at ambient pressure, supporting a small enthalpy difference between octahedral and tetrahedral polymorphs of GeO_2 . [47, 48] Given that for TiO_2 we compute even smaller transition pressures (PBE: -0.4 GPa; SCAN: -1.9 GPa) than for GeO_2 , a transition of rutile into a structure with tetrahedral TiO_4 -units should be feasible.

Negative pressures correspond to isotropic tensile stresses and have been realized by mixing materials with differing crystal structures.[49] Yet another approach is the synthesis of a material or composite under compressive stress and subsequent relaxation. This can be achieved, for instance, by thin film deposition on a bent substrate. Stress-relief of the substrate will in turn induce (negative) tensile stresses on the film. Stresses in the range of 5 GPa are quite commonly occurring in thin film depositions.[50, 51] The rate of a transition and, thus, whether the two polymorphs, cristobalite and rutile, can practically be converted into one another, depends on the activation energy required for

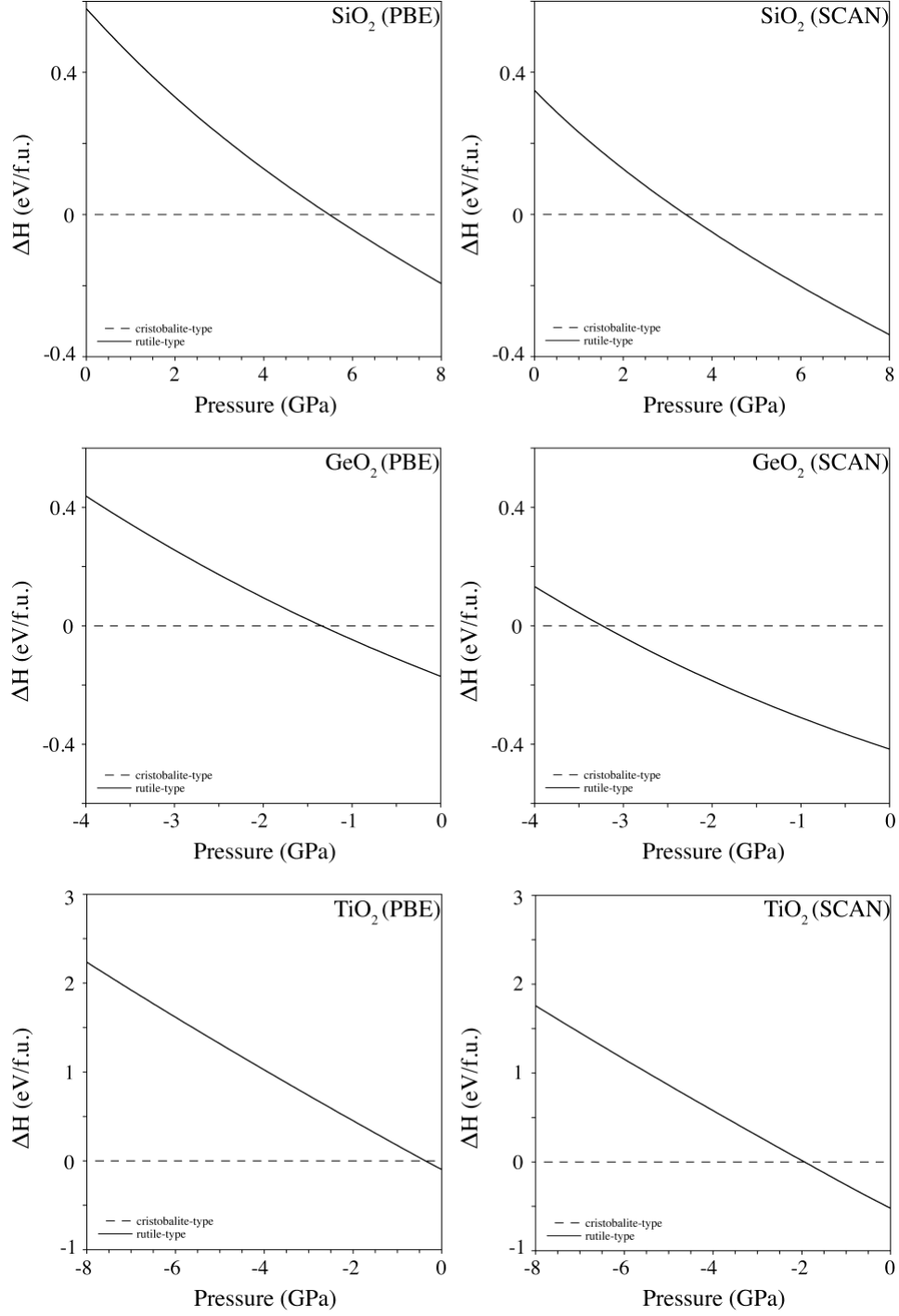


Figure 3: Enthalpy-pressure diagrams for MO_2 (M=Si, Ge, Ti) relative to enthalpy of corresponding cristobalite-type using PBE and SCAN functionals. Cristobalite-rutile transition pressures are found at intersections of enthalpy curves.

the process. Hence our further investigations address the energy profile of a transition between cristobalite- and rutile-type structures.

Transformation profiles between cristobalite and rutile at different pressures

We then set out and computed the enthalpy profile for the transformation from cristobalite-type to rutile-types structure for each compound. The forward transition starts with the optimized structures of cristobalite-types of SiO₂, GeO₂, and TiO₂, while the reverse transition starts with the rutile-type of each compound. We explicitly computed both directions of the transition path, forward and reverse, for each method and received matching energy profiles. We computed transition paths at ambient pressure (0 GPa), at the computed transition pressures (see Table 3), and at a few additional pressures to highlight trends. If a transition was performed at a given pressure, we selected optimized geometries of initial and final structures accordingly.

The enthalpy profile of a transition path reflects the enthalpy differences cristobalite- and rutile-type structures for a given MO₂ compound at a given pressure. Thus, at ambient pressure (0 GPa) initial and final state are energetically different according to the data of Table 3. At transition pressure p_t , however, cristobalite- and rutile-type have equal enthalpy and appear at level with each other. All transition paths provide a configuration with maximum enthalpy, the transition state. The activation barrier for the forward reaction, $\Delta H_{a,fwd}$, is defined as the enthalpy difference between cristobalite and the transition state. Conversely, the difference between rutile and the transition state constitutes the activation barrier for the reverse reaction, $\Delta H_{a,rev}$. We have chosen to plot the energy profiles relative to the structure with lowest energy at ambient pressure. Thus, for SiO₂ we plot the profile relative to cristobalite-type, while for GeO₂ and TiO₂ we plot all profiles relative to the rutile type.

SiO₂

The energy profiles for the two different paths to convert α -cristobalite to stishovite are shown in Figure 4. Enthalpy barriers for the forward path, $\Delta H_{a,fwd}$, at different pressures are listed in Table 4. For paths computed at 0 GPa in both anion and cation method, we investigated the transition state in more detail and computed the Hessian matrix. It exhibits only a single imaginary eigenvalue, and the corresponding eigenvector aligns with conservation of space group symmetry $C222_1$. Overall we find that the cation

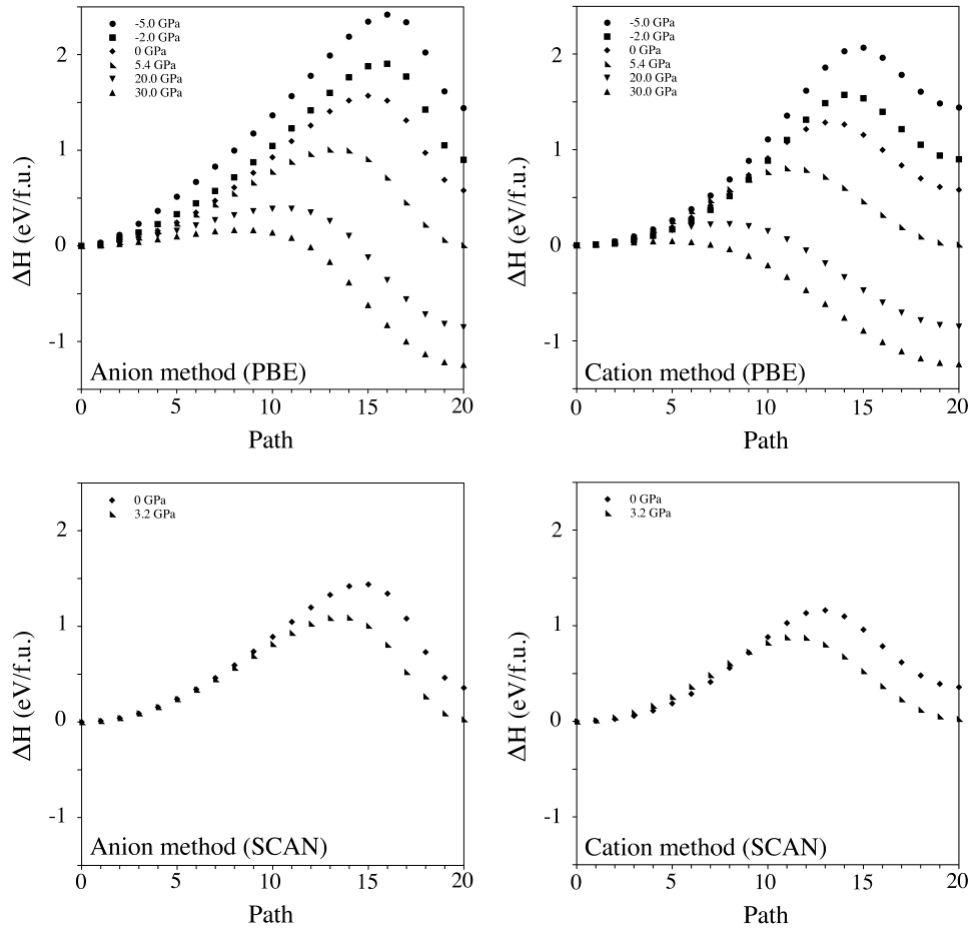


Figure 4: Enthalpy profiles of SiO₂ α -cristobalite (step=0) to stishovite (step=20) transition at various pressures. PBE calculations for (top left) anion and (top right) cation method; SCAN calculations for (bottom left) anion and (bottom right) cation method. All enthalpies are given relative to α -cristobalite SiO₂ at the corresponding pressure.

Table 4: Forward activation enthalpies $\Delta H_{a,fwd}$ for SiO₂ cristobalite-rutile transformations. The asterisk (*) indicates the transition pressure computed in the respective method.

Pressure (GPa)	Anion method $\Delta H_{a,fwd}$ (eV/f.u.)	Cation method $\Delta H_{a,fwd}$ (eV/f.u.)
PBE		
-5.0	2.42	2.07
-2.0	1.90	1.57
0	1.57	1.28
5.4*	1.01	0.81
20.	0.39	0.22
30.	0.17	0.04
SCAN		
0	1.44	1.16
3.2*	1.09	0.88

method produces slightly lower enthalpies, and consequently lower $\Delta H_{a,fwd}$, in comparison to the anion method. This occurs because more degrees of freedom, three position parameters and two cell parameters, are allowed to relax in this approach. In the anion method, we allow only one position parameter to optimize, while all other parameters are interpolated. We also observe that increasing pressure reduces the enthalpy barrier of the forward path, $\Delta H_{a,fwd}$, in either method and in both PBE and SCAN calculations.

Eventually the activation energy $\Delta H_{a,fwd}$ approaches zero (0) at 30 GPa. In experiments, α -cristobalite-SiO₂ completely amorphizes at about 28 GPa.[52] Comparing the two functionals we find that SCAN calculations yield slightly lower activation energies than their PBE counterparts; at ambient pressure $\Delta H_{a,fwd}$ is about 10% lower. For the transition pressure p_t itself, however, $\Delta H_{a,fwd}$ computed in SCAN is slightly higher,

because SCAN computes lower transition pressures in general. Conversely, the higher transition pressure p_t obtained with the PBE functional impacts the energy profile and yields a lower $\Delta H_{a,fwd}$ at p_t .

GeO₂

The energy profiles for the transition paths from an α -cristobalite-type to rutile-type GeO₂ are shown in Figure 5. Note that we depict enthalpy relative to rutile GeO₂ (see Table 5), since this is lower in energy at ambient pressure than cristobalite GeO₂. Consequently, we address $\Delta H_{a,rev}$, the enthalpy barrier for the reverse path. Again, the cation method yields

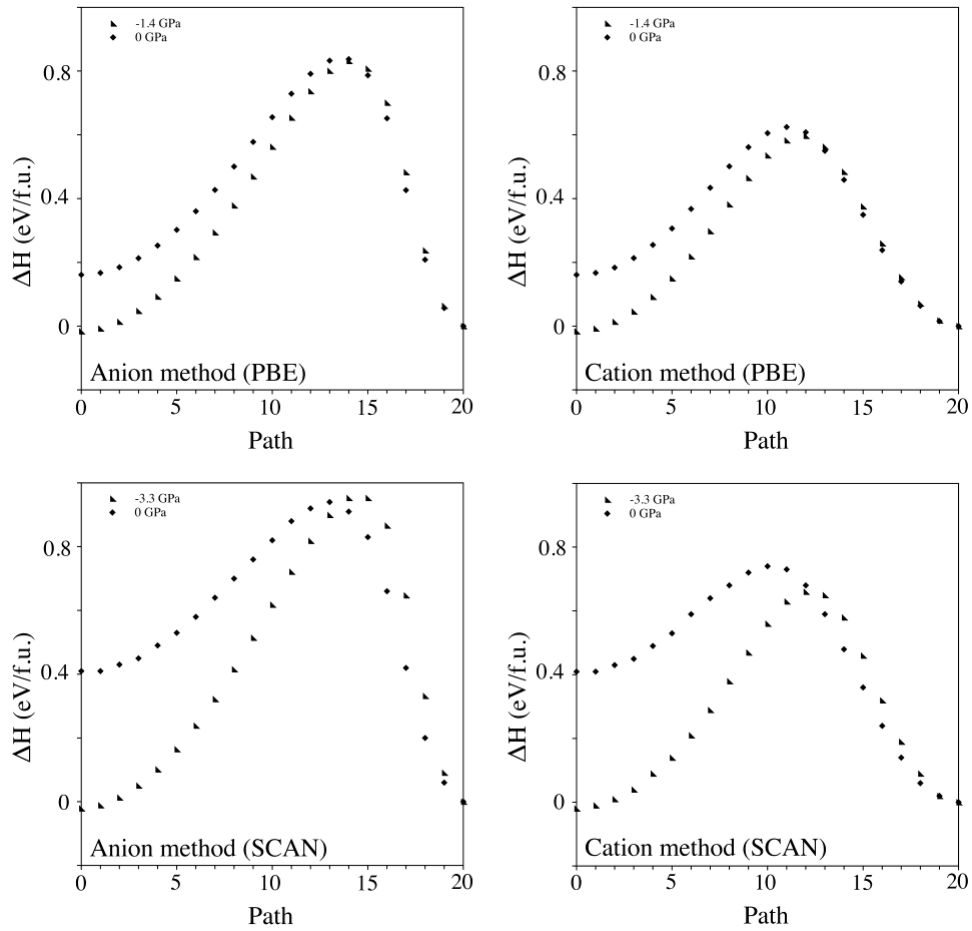


Figure 5: Enthalpy profiles of GeO₂ α -cristobalite (step=0) to rutile (step=20) transition at ambient and transition pressure p_t . PBE calculations for (top left) anion and (top right) cation method; SCAN calculations for (bottom left) anion and (bottom right) cation method. All enthalpies are given relative to rutile GeO₂ at corresponding pressure.

Table 5: Reverse activation enthalpies $\Delta H_{a,rev}$ for GeO₂ cristobalite-rutile transformations. The asterisk (*) indicates the transition pressure computed in the respective method.

Pressure (GPa)	Anion method $\Delta H_{a,rev}$ (eV/f.u.)	Cation method $\Delta H_{a,rev}$ (eV/f.u.)
PBE		
0	0.84	0.62
-1.4*	0.83	0.60
SCAN		
0	0.94	0.74
-3.3*	0.95	0.66

lower enthalpy profiles and lower $\Delta H_{a,rev}$ in comparison to the anion method. An impact of pressure on the energy profile is best seen within the cation method. Decreasing the pressure lowers the energy profile and, as a consequence, yields a lower $\Delta H_{a,rev}$ at negative pressure. Comparing PBE and SCAN calculations we find that SCAN calculations in case of GeO₂ yield higher activation energies than their PBE counterparts, about 20% at ambient pressure. Even at the transition pressure, which SCAN locates at larger negative pressure than PBE, there is still a 10% difference.

TiO₂

The energy profiles for the transition paths from an α -cristobalite-type to rutile-type TiO₂ are shown in Figure 6. We depict enthalpy relative to rutile TiO₂ and address the enthalpy barrier $\Delta H_{a,rev}$ of the reverse path (see Table 6). Once more, the cation

method yields lower enthalpy profiles and lower $\Delta H_{a,rev}$ in comparison to the anion method. Reducing pressure significantly lowers the energy profile and, as a consequence, yields a lower $\Delta H_{a,rev}$.

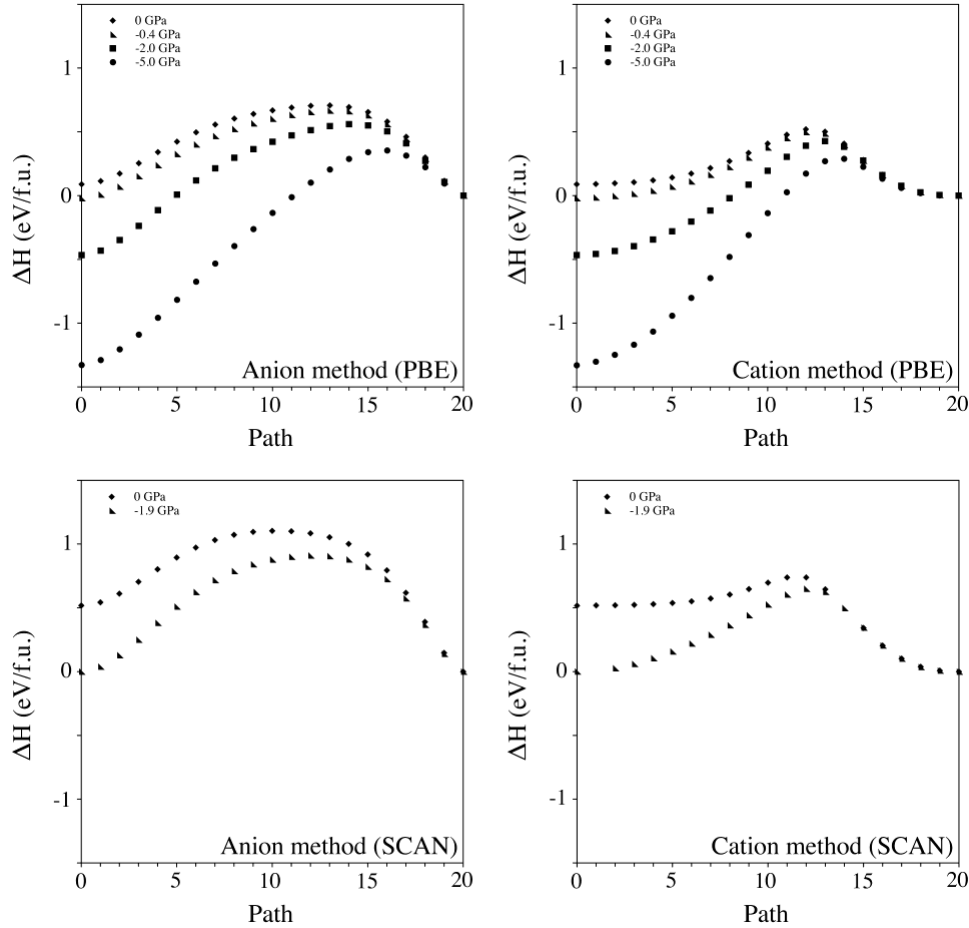


Figure 6: Enthalpy profiles of TiO_2 α -cristobalite (step=0) to rutile (step=20) transition at ambient and transition pressure p_t . PBE calculations for (top left) anion and (top right) cation method; SCAN calculations for (bottom left) anion and (bottom right) cation method. All enthalpies are given relative to rutile TiO_2 at corresponding pressure. Two points in the diagram for cation method with SCAN (step 1 at -1.9 GPa and step 14 at 0 GPa) could not be optimized.

Like with GeO_2 , SCAN calculations yield higher activation energies (about 40%) than their PBE counterparts. Independent of the path selected, however, going from ambient (0 GPa) to -5 GPa essentially cuts the activation barrier in half. Thus, negative pressure

not only favors the cristobalite-type of TiO_2 , but also makes it more easily accessible within this transformation.

Table 6: Reverse activation enthalpies $\Delta H_{a,\text{rev}}$ for TiO_2 cristobalite-rutile transformations. The asterisk (*) indicates the transition pressure computed in the respective method.

Pressure (GPa)	Anion method $\Delta H_{a,\text{rev}}$ (eV/f.u.)	Cation method $\Delta H_{a,\text{rev}}$ (eV/f.u.)
PBE		
-5.0	0.35	0.29
-2.0	0.56	0.43
-0.4*	0.69	0.50
0	0.71	0.52
SCAN		
-1.9*	0.91	0.65
0	1.10	0.74

Further reducing Degrees of Freedom during Transformations

The cation method and anion method are distinguished by the number of constraints implied and by the degrees of freedoms optimized at every step. Overall, the cation method yields lower activation barriers, because at every step more atom coordinates as well as the lattice parameters can relax. It is, therefore, of interest to see, if we can put even less constraints onto the transition and what enthalpy profile this would yield.

Starting with the same size of the simulation cell, 8 cations and 16 anions in space group $C222_1$, we extended the cation method in such a way as we did not impose any symmetry constraint ($P1$) and, furthermore, allowed half of the cations to optimize during the transformation as well. Thus, a concerted motion is only provided by 4 cations, while all other atoms and cell parameters optimize in each intermediate step. We investigated the

path for SiO₂ at ambient pressure (0 GPa) with two different selections of a group of 4 cations, of which we will display the results of one only. The second choice had, essentially, very similar consequences.

Two energy profiles of this “half-cation method” are shown in Figure 7. One corresponds to a forward transition starting with α -cristobalite SiO₂. The value of the activation barrier, $\Delta H_{a, \text{fwd}} = 1.17 \text{ eV/f.u.}$, is slightly lower than the 1.28 eV/f.u. we computed for the (regular) cation method. However, the forward transformation did not yield the expected stishovite SiO₂ structure. Instead, it left the $C222_1$ path early on, coinciding with a non-orthogonal cell at the transition point. Each Si atom still gained two additional bonds but from different O in comparison to the cation method. The final structure adopts monoclinic symmetry (SpGr. $P2_1(4)$)[53] with yet another ordered arrangement of SiO₆ octahedra. It bears resemblance to seifertite-SiO₂,[44] although the agreement is not perfect. Its energy comes out as 0.1 eV/SiO₂ higher than that of seifertite-SiO₂.

The second profile in Figure 7 corresponds to the reverse transition, starting with stishovite SiO₂. The profile is noticeably different from the graph shown in Figure 6.

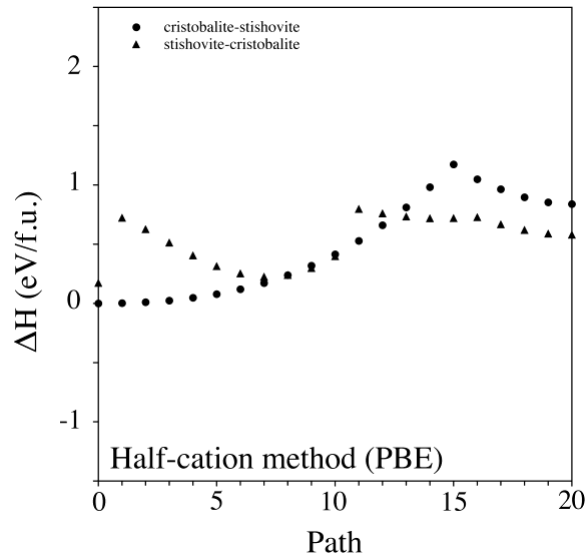


Figure 7: Enthalpy profiles of transformations from cristobalite-SiO₂ to stishovite-SiO₂ and stishovite-SiO₂ to cristobalite-SiO₂; transformations were done at zero pressure with PBE using the half-cation method. Enthalpies are relative to the enthalpy of α -cristobalite-SiO₂.

Moreover, rather than an activation barrier of 0.71 eV/f.u.—the value of the reverse transformation from stishovite to cristobalite following the $C222_1$ path in the cation method—we find that the stishovite structure ruptures with an activation of barely 0.22 eV/f.u. The outcome is not the cristobalite structure either but a disordered arrangement of four- and eight membered rings of corner-sharing SiO₄ tetrahedra in a non-rectangular cell. Its relation to the cristobalite structure is unclear to us. However, it may only take a relatively small amount of bond rearrangements to relate both structures. Such mechanisms are known among polymorphs of SiO₂, for example, for the tridymite to keatite transition.[54]

The results above show, although the idealized structures were not reached, that cristobalite naturally transforms into a structure with SiO₆ octahedra upon compression. Indeed, ab-initio molecular dynamics simulation show that α -cristobalite-SiO₂ transforms into stishovite-SiO₂ at high pressure, with intermediates described within $C222_1$ symmetry.[19] We reproduced the results using the same small simulation cell as in the original study. However, extending the simulation cell to twice its size produced disordered models comprising SiO₆ octahedra rather than stishovite. Conversely, the transition paths show that upon expansion stishovite transforms into a structure with SiO₄ tetrahedra. Adding more degrees of freedom produced slightly lower activation barriers, indicating that our values we present in Tables 4, 5, and 6 can be considered as upper boundaries. Even though the idealized structures were not reached, it is conceivable that in an experiment further annealing of a disordered compound under compressive or tensile stress yields crystalline samples.

Conclusions

Increasing pressure increases the relative stability of the rutile-type over the cristobalite-type for SiO_2 , GeO_2 , and TiO_2 . While for SiO_2 the rutile-type succeeds the cristobalite-type at high pressures, we show that for GeO_2 and TiO_2 , where the rutile-type is an ambient pressure modification, the cristobalite-type is attainable at small negative pressures. Our investigation of transition paths show that increasing pressure yields lower activation barriers for a transformation from cristobalite-type to rutile-type. The activation barrier of the reverse transformation, from rutile-type into cristobalite-type, decreases with decreasing pressure. Following concerted movements of atoms, we show that the cation method of Salvadó et al.[21] yields lower activation barriers than a concerted movement of anions. Even smaller barriers are encountered if only a subset of cations is moved. The resulting structures in these “half cation methods” for both forward and reverse paths still display octahedral or tetrahedral coordination of all cations but may not match rutile or cristobalite structures.

Given that the magnitude of negative pressure at which cristobalite- GeO_2 and cristobalite- TiO_2 become thermodynamically stable is only 1 to 3 GPa, we propose to prepare experiments that utilize tensile stresses of this magnitude. For example, rutile-type GeO_2 or TiO_2 may be deposited as thin film on a curved substrate, which is then relaxed. Subsequent annealing at moderate temperatures may yield a crystalline tetrahedrally coordinated structure. Two new compounds with potentially interesting properties are in reach through relatively simple synthetic pathways.

Acknowledgements

This work was supported by the National Science Foundation (NSF) through awards DMR-1463974 and CMMI-1634448. The computational work was made possible through generous grants by the Texas Advance Computing Center in Austin, TACC, Texas and by the High Performance Computing facilities at UTA.

Conflicts of interest

There are no conflicts to declare.

Data availability

The raw/processed data required to reproduce these findings cannot be shared at this time due to technical or time limitations.

References

- [1] A.F. Wells, Structural inorganic chemistry, Clarendon Press, Oxford, 1975.
- [2] A.J. Leadbetter, A.F. Wright, The Philosophical Magazine: A Journal of Theoretical Experimental and Applied Physics, 33 (1976) 105-112.
- [3] S.M. Stishov, S.V. Popova, Geokhimiya, 10 (1961).
- [4] E.C.T. Chao, J.J. Fahey, J. Littler, D.J. Milton, Journal of Geophysical Research, 67 (1962) 419-421.
- [5] H. Böhm, Naturwissenschaften, 55 (1968) 648-649.
- [6] E. Hauser, H. Nowotny, K.J. Seifert, Monatshefte für Chemie, 101 (1970) 715-720.
- [7] O. Yamaguchi, K. Kotera, M. Asano, K. Shimizu, J. Chem. Soc., Dalton Trans., (1982) 1907-1910.
- [8] P. Degryse, J. Elsen, in, Leuven University Press, Leuven, Belgium, 2003, pp. 120.
- [9] J.M. Léger, J. Haines, M. Schmidt, J.P. Petit, A.S. Pereira, J.A.H. da Jornada, Nature, 383 (1996) 401.
- [10] M. Micolaut, L. Cormier, G.S. Henderson, Journal of Physics: Condensed Matter, 18 (2006) R753-R784.
- [11] M. Sahnoun, C. Daul, R. Khenata, H. Baltache, The European Physical Journal B - Condensed Matter and Complex Systems, 45 (2005) 455-458.
- [12] L. Vegard, The London, Edinburgh, and Dublin Philosophical Magazine and Journal of Science, 32 (1916) 505-518.
- [13] R.E. Day, Progress in Organic Coatings 2, (1973) 269.
- [14] D.H. Solomon, D.G. Hawthorne, Chemistry of Pigments and Fillers, John Wiley, New York, 1983.
- [15] Y. Cao, T. He, Y. Chen, Y. Cao, The Journal of Physical Chemistry C, 114 (2010) 3627-3633.
- [16] D. Deng, M.G. Kim, J.Y. Lee, J. Cho, Energy & Environmental Science, 2 (2009) 818-837.
- [17] M. O'Keefe, B.G. Hyde, Acta Crystallographica Section B, 32 (1976) 2923-2936.
- [18] B. Silvi, L.H. Jolly, P. D'Arco, Journal of Molecular Structure: THEOCHEM, 260 (1992) 1-9.
- [19] D.D. Klug, R. Rousseau, K. Uehara, M. Bernasconi, Y. Le Page, J.S. Tse, Physical Review B, 63 (2001) 104106.
- [20] L. Huang, M. Durandurdu, J. Kieffer, Nature Materials, 5 (2006) 977.

- [21] M.A. Salvadó, P. Pertierra, A. Morales-García, J.M. Menéndez, J.M. Recio, *The Journal of Physical Chemistry C*, 117 (2013) 8950-8958.
- [22] T. Moon, P. Kroll, *J. High Res.*, (2010).
- [23] G. Kresse, J. Hafner, *Physical Review B*, 47 (1993) 558-561.
- [24] G. Kresse, J. Hafner, *Physical Review B*, 49 (1994) 14251-14269.
- [25] G. Kresse, J. Furthmüller, *Computational Materials Science*, 6 (1996) 15-50.
- [26] G. Kresse, J. Furthmüller, *Physical Review B*, 54 (1996) 11169-11186.
- [27] J.P. Perdew, K. Burke, M. Ernzerhof, *Physical Review Letters*, 77 (1996) 3865-3868.
- [28] J.P. Perdew, K. Burke, M. Ernzerhof, *Physical Review Letters*, 78 (1997) 1396-1396.
- [29] J. Sun, A. Ruzsinszky, J.P. Perdew, *Physical Review Letters*, 115 (2015) 036402.
- [30] P.E. Blöchl, *Physical Review B*, 50 (1994) 17953-17979.
- [31] G. Kresse, D. Joubert, *Physical Review B*, 59 (1999) 1758-1775.
- [32] H.J. Monkhorst, J.D. Pack, *Physical Review B*, 13 (1976) 5188-5192.
- [33] R.W.G. Wyckoff, *American Journal of Science*, 9 (1925) 448-459.
- [34] D.C. Palmer, in, *CrystalMaker Software Ltd*, Begbroke, Oxfordshire, England, 2014.
- [35] J.B. Parise, A. Yeganeh-Haeri, D.J. Weidner, J.D. Jorgensen, M.A. Saltzberg, *Journal of Applied Physics*, 75 (1994) 1361-1367.
- [36] K.J. Seifert, H. Nowotny, E. Hauser, *J Monatshefte für Chemie / Chemical Monthly*, 102 (1971) 1006-1009.
- [37] M. Sugiyama, S. Endo, K. Koto, *Mineralogical Journal*, 13 (1987) 455-466.
- [38] J. Haines, J.M. Léger, C. Chateau, A.S. Pereira, *Physics and Chemistry of Minerals*, 27 (2000) 575-582.
- [39] S.C. Abrahams, J.L. Bernstein, *The Journal of Chemical Physics*, 55 (1971) 3206-3211.
- [40] H. Peng, Z. Yang, J. Sun, J.P. Perdew, *ArXiv e-prints*, (2016) arXiv:1510.05712.
- [41] H. Kim, J.-M. Choi, W.A. Goddard, *The Journal of Physical Chemistry Letters*, 3 (2012) 360-363.
- [42] N. Khosrovani, A.W. Sleight, *Journal of Solid State Chemistry*, 121 (1996) 2-11.
- [43] Y. Tsuchida, T. Yagi, *Nature*, 347 (1990) 267-269.
- [44] T. Kubo, T. Kato, Y. Higo, K.-i. Funakoshi, *Science Advances*, 1 (2015) e1500075.
- [45] A. Černok, K. Marquardt, R. Caracas, E. Bykova, G. Habler, H.-P. Liermann, M. Hanfland, M. Mezouar, E. Bobocioiu, L. Dubrovinsky, *Nature Communications*, 8 (2017) 15647.
- [46] S. Saito, T. Ono, *Japanese Journal of Applied Physics*, 50 (2011) 02153-02151 - 021503-021505.
- [47] J. Haines, O. Cambon, E. Philippot, L. Chapon, S. Hull, *Journal of Solid State Chemistry*, 166 (2002) 434-441.
- [48] A.W. Laubengayer, D.S. Morton, *Journal of the American Chemical Society*, 54 (1932) 2303-2320.
- [49] S. Siol, A. Holder, J. Steffes, L.T. Schelhas, K.H. Stone, L. Garten, J.D. Perkins, P.A. Parilla, M.F. Toney, B.D. Huey, W. Tumas, S. Lany, A. Zakutayev, *Science Advances*, 4 (2018) eaaq1442.
- [50] D.R. McKenzie, D. Muller, B.A. Pailthorpe, *Physical Review Letters*, 67 (1991) 773-776.

- [51] J.W. Ager, S. Anders, A. Anders, I.G. Brown, *Applied Physics Letters*, 66 (1995) 3444-3446.
- [52] A.J. Gratz, L.D. DeLoach, T.M. Clough, W.J. Nellis, *Science*, 259 (1993) 663-666.
- [53] H.T. Stokes, D.M. Hatch, *Journal of Applied Crystallography*, 38 (2005) 237-238.
- [54] C.-T. Li, *Acta Crystallographica Section B*, 27 (1971) 1132-1140.

Summary

We investigated the cristobalite-rutile transformation in the forward and reverse directions for SiO_2 , GeO_2 and TiO_2 . Transformations between cristobalite-type and rutile-type structures were described using two different concerted mechanisms, an anion method and a cation method, which were named depending on which set of ions were moved in a concerted fashion during the transformation. We investigated the activation barriers of the forward and reverse transformations for a range of different external pressures, including negative pressures. Increasing pressure favored the rutile structure-type and resulted in a lowered activation barrier for the forward cristobalite-rutile transformation. Decreasing pressure favored the cristobalite structure-type and lowered the activation barrier of the reverse transformation, or the rutile-cristobalite transformation. At negative pressures, cristobalite-type GeO_2 and TiO_2 became thermodynamically stable and we predicted that the synthesis of cristobalite-type GeO_2 and TiO_2 may be possible with moderate tensile stresses.

CHAPTER 2: A NOVEL HIGH-PRESSURE TIN OXYNITRIDE $\text{Sn}_2\text{N}_2\text{O}$

Motivation and Scope

A new *Pbcn* $\text{Sn}_2\text{N}_2\text{O}$ with all Sn six-fold coordinated is synthesized through high-pressure experiments. Ammonolysis is performed on $\text{Sn}[\text{NMe}_2]_4$ mixed with tetrahydrofuran[1] and the resulting Sn-N-O precursors are then subjected to 20 GPa and 1200-1500°C. Characterization is done on the synthesized samples with powdered X-ray diffraction and automated diffraction tomography. Additionally, bulk modulus is experimentally determined. We contribute supporting DFT[2] calculations for elastic properties, including bulk modulus and shear modulus, and band gaps. We seek to rationalize the formation of *Pbcn* $\text{Sn}_2\text{N}_2\text{O}$ by calculating the enthalpy of formation of *Pbcn* $\text{Sn}_2\text{N}_2\text{O}$ from binary compounds at different pressures.

References

- [1] X. Li, A.L. Hector, J.R. Owen, S.I.U. Shah, Evaluation of nanocrystalline Sn_3N_4 derived from ammonolysis of $\text{Sn}(\text{NEt}_2)_4$ as a negative electrode material for Li-ion and Na-ion batteries, *Journal of Materials Chemistry A* 4(14) (2016) 5081-5087.
- [2] P. Hohenberg, W. Kohn, Inhomogeneous Electron Gas, *Physical Review* 136(3B) (1964) B864-B871.

A Novel High-Pressure Tin Oxynitride $\text{Sn}_2\text{N}_2\text{O}$

Shrikant Bhat,^{*[a, e]} Leonore Wiehl,^[b] Shariq Haseen,^[c] Peter Kroll,^[c] Konstantin Glazyrin,^[a] Philipp Gollé-Leidreiter,^[b] Ute Kolb,^[b, d] Robert Farla,^[a] Jo-Chi Tseng,^[a] Emanuel Ionescu,^[b] Tomoo Katsura,^[e] and Ralf Riedel^[b]

^[a]Dr. S. Bhat, Dr. K. Glazyrin, Dr. R. Farla, Dr. J.-C. Tseng

Photon Science, DESY, Notkestrasse 85, 22607 Hamburg (Germany) E-mail:shrikant.bhat@desy.de

^[b]Dr. L. Wiehl, P. Gollé-Leidreiter, Prof. Dr. U. Kolb, Dr. E. Ionescu, Prof. Dr. R. Riedel
FB Material- und Geowissenschaften, Technische Universität Darmstadt 64287,
Darmstadt (Germany)

^[c]S. Haseen, Prof. Dr. P. Kroll

Department of Chemistry and Biochemistry

The University of Texas at Arlington, Arlington, Texas 76019-0065 (USA)

^[d]Prof. Dr. U. Kolb

Institut für Physikalische Chemie, Johannes Gutenberg-Universität Mainz 55128 Mainz
(Germany)

^[e]Dr. S. Bhat, Prof. Dr. T. Katsura

Bayerisches Geoinstitut (BGI), University of Bayreuth 95440 Bayreuth (Germany)

Abstract

We report the first oxynitride of tin, $\text{Sn}_2\text{N}_2\text{O}$ (SNO), exhibiting a Rh_2S_3 -type crystal structure with space group $Pbcn$. All Sn atoms are in six-fold coordination, in contrast to Si in silicon oxynitride ($\text{Si}_2\text{N}_2\text{O}$) and Ge in the isostructural germanium oxynitride

(Ge₂N₂O), which appear in four-fold coordination. SNO was synthesized at 20 GPa and 1200 – 1500°C in a large volume press. The recovered samples were characterized by synchrotron powder X-ray diffraction.

Introduction

The Group 14 elements Si, Ge, and Sn form well-known nitrides[1] with exceptional thermomechanical and optoelectronic properties. Low compressibility and high hardness[1a,2] have been reported for spinel-type Si and Ge nitrides, and their solid solutions are predicted to form a new family of wide direct band gap semiconductors.[3] Hitherto, oxynitrides are known for Si and Ge, but not for Sn. Silicon oxynitride (Si₂N₂O), named “Sinoite”, was discovered in a meteorite by Andersen et al.[1e] in 1962. At the same time, a synthetic Si₂N₂O was prepared by nitriding a mixture of silicon and quartz powder at 1450°C.[1f] It shows orthorhombic symmetry with space group *Cmc*2₁. [1f] Sinoite proved to be one of the most stable, oxidation resistant refractory oxynitrides.[4] Its formation and thermodynamic stability at ambient and high pressure have been investigated computationally previously.[1c] An isostructural germanium oxynitride Ge₂N₂O has been synthesized by ammonolysis of germanium oxides at temperatures above 850°C as well.[1d,5]

An oxynitride of tin is still unknown and has to the best of our knowledge not been reported as bulk material. There are a few reports on thin films of SnO_xN,[6] described as nitrogen-doped tin oxide with undetermined chemical composition and with a crystal structure related to SnO₂, either as rutile-type (mineral name cassiterite), or as pyrite-type high-pressure form.[6a,7] We did not find any computational studies related to tin oxynitrides.

Herein, we report the first tin oxynitride, exhibiting a Rh₂S₃-type crystal structure, which is known as a high-pressure modification of several oxides including Al₂O₃ and Fe₂O₃. All Sn atoms are in six-fold coordination, in contrast to the sinoite-type with only

four-fold metal coordination. We employed a high-pressure high-temperature (HP-HT) method, using a large volume press (LVP) for the synthesis of a novel $\text{Sn}_2\text{N}_2\text{O}$ compound (SNO). Materials are characterized by elemental analysis, angle-dispersive XRD, TEM in combination with automated diffraction tomography (ADT), and energy-dispersive X-ray spectroscopy (EDX). We also determined the bulk modulus of SNO and used DFT calculations for structure modelling.

Results and Discussion

Precursor and HP-HT synthesis

The XRD pattern of the Sn-N-O precursor, prepared by low temperature ammonolysis, shows spinel-type Sn_3N_4 (as the only crystalline phase) and an amorphous background (Figure S1, Supporting Information). Elemental analysis by the combustion method confirmed a content of 5.3(3) wt.% oxygen and 11.2(2) wt.% nitrogen in the synthesized compound. From these values, elemental contents of 18 (1) at.% O, 43.6 (8) at.% N, and 38(1) at.% Sn in the as-received compound can be calculated, which may be described as a mixture of tin nitride and tin oxide with a molar ratio of 1:1. This formally corresponds to a $\text{Sn}_2\text{N}_2\text{O}$ stoichiometry. This precursor was subjected to HP-HT conditions (20 GPa and 1200–1500°C) in a Hall-type six-ram LVP (mavo press LPQ6 1500-100; Max Voggenreiter GmbH, Germany) installed at the P61B beamline at DESY, Hamburg. After HP-HT treatment, each recovered sample was dense and fine-grained in appearance (Figure S3, Supporting Information). EDX spectroscopy on the recovered samples confirms the presence of oxygen in addition to nitrogen and tin (Figure S4, Supporting Information) without other contamination. Quantification of O and N was not possible as EDX is not reliable for low Z elements.[8]

X-ray diffraction

The XRD pattern of the HP-HT product measured with synchrotron radiation (Figure 1) shows a manifold of well resolved reflections—apart from a small fraction of spinel Sn_3N_4 —which do not match to any known phase in the powder diffraction database (ICDD). They represent a novel phase, which (in the first approach) could be indexed by a primitive cubic lattice with $a=7.831(2)$ Å.

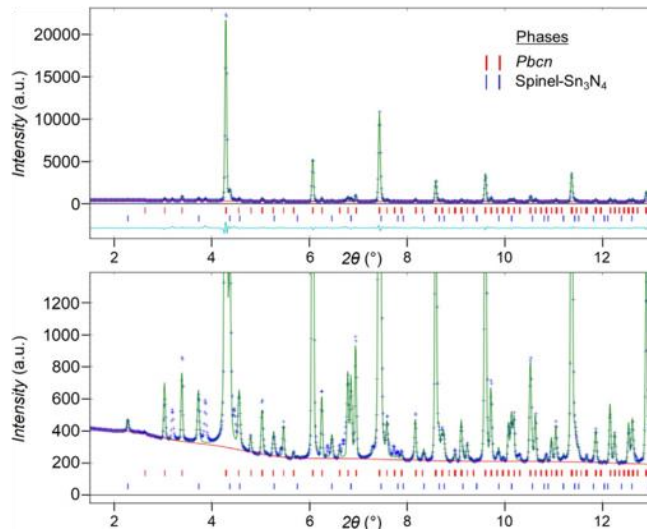


Figure 1. XRD pattern of SNO, in full (top) and magnified by a factor of ≈ 20 (bottom), with Rietveld refinement (green line) in space group *Pbcn* ($\lambda=0.20736$ Å). The reflection markers show the calculated reflection positions of the SNO phase (upper row, in red online) and the spinel Sn_3N_4 (lower row, in blue online).

A preliminary structure model of SNO could be deduced from the integrated intensities of the powder reflections, using direct methods (shelxs2013[9]). This model in space group *Pa-3* represents a double perovskite with two inequivalent Sn sites. One Sn shows a distorted octahedral coordination as usual in low-symmetry double perovskites. The other Sn resides in the centre of eight corner-linked octahedra, a position which in perovskites usually is occupied by atoms larger than those in the octahedral position. The cation to anion ratio of 2:3, implied by the structure model, is in accordance with the measured chemical composition $\text{Sn}_2\text{N}_2\text{O}$ (for Sn^{4+} , N^{3-} , O^{2-}). However, the model appears to represent only an averaged structure. No satisfying Rietveld refinement could be

achieved within the framework of the cubic unit cell. On the other hand, a possible splitting of X-ray reflections indicating a distortion of the cubic unit cell to lower symmetry seems to be too small to be detected in the XRD pattern.

Electron diffraction tomography (ADT)

To elucidate the correct crystal symmetry of SNO, electron diffraction covering the 3D space was performed, namely automated diffraction tomography (ADT)[10] on a synthesized sample (run# HH148 at 20 GPa, 1500°C, Ta capsule). This sample contained only a very low fraction of spinel Sn_3N_4 and no third phase, as confirmed by XRD ($\text{CuK}\alpha$). ADT allows for collecting electron-diffraction intensities from single crystals as small as some tens of nm, and thus enables single-crystal structure determination from such small crystals. Crystals were used without any special orientation to the electron beam. The acquired off-zone diffraction patterns show reduced dynamical scattering effects and provide intensity data suitable for kinematical structure determination approaches like direct methods. For data acquisition a series of electron diffraction images (2D detector) are collected while tilting the crystal by 1° after every image. The wedges between the zones are integrated using electron beam precession. By processing these images afterwards, all patterns are reconstructed into a 3D diffraction space allowing visualization of the full diffraction information. More details are shown in the Supporting Information.

The unit-cell was derived from ADT data with lattice parameters $a=7.80$, $b=5.42$, $c=5.52$ Å, which corresponds to an orthorhombic metric in the limit of expected errors of 1% for cell axes and 1° for angles. Two of the cell edges are approximately equal in length, and by a factor of $\sqrt{2}$ shorter than the third one, in accordance with the pseudo-cubic unit cell from the XRD powder pattern. Inspection of the systematic extinctions leads to a match with space group (S.G.) $Pbcn$. The crystal structure was solved from 224 unique diffraction intensities at a resolution limit of 0.8 Å, using direct methods

(SIR2014).[11] For the further evaluation of the single-crystal ADT measurement, optimized lattice parameters from the synchrotron powder XRD data were used, as they are much more precise than those from electron diffraction.

Lattice parameters from XRD

The lattice parameters of SNO were optimized by Rietveld refinement of the synchrotron powder data in S.G. *Pbcn*, with starting values from electron diffraction. In comparison with LaB₆, only a small line broadening of the SNO reflections was observed, corresponding to a crystallite size of ≈ 250 nm. The refined lattice parameters are $a=7.8257(8)$, $b=5.5315(5)$, $c=5.5438(4)$, and $V=239.98(4)$ Å³ with ratios of $a/b=1.4148=1.0004 \times \sqrt{2}$ and $a/c=1.4116=0.9982 \times \sqrt{2}$. The deviation of the unit-cell parameters from pseudo-cubic symmetry is so small, that the orthorhombic line splitting is less than the reflection width (FWHM) in the synchrotron powder diagram, as shown by the red tic marks in Figure 1. The upper figure shows the full XRD pattern with the profile calculated by Rietveld refinement in green colour and the difference curve in cyan. Below, an enlarged view of the same pattern is shown, magnified by a factor of ≈ 20 to enable visualization of the weak reflections. The structure model in space-group *Pbcn* was adopted from the crystal structure derived from ADT and not refined. The final wR is 7.5% and the phase fraction of spinel Sn₃N₄ (blue tic marks) refined to 8.6 wt.%. There remain a few noninterpreted reflections belonging to a third, yet unknown phase (visible XRD data points without green calculated profile). These reflections cannot be explained by metallic tin or any of the reported Sn–O phases such as SnO₂ at ambient conditions (rutile-type *P4₂/mnm*)[12] or at high-pressure (*Pnnm* and pyrite-type *Pa-3*),[7] or by Sn₂O₃ (*P1*),[13] Sn₃O₄ (*P2₁/c*),[14] or SnO (litharge-type *P4/nmm*).[15]

Crystal structure from ADT

The crystal structure was kinematically refined from 5176 single-crystal reflections measured as ADT data set up to a resolution of 0.5 Å. Averaging equivalent reflections in space group *Pbcn* resulted in 1046 unique reflections with $R_{\text{int}}=0.21$. The final residual is $R1=0.26$. Dynamical refinement reduced the residual further to $R1=0.09$. Dynamically derived atomic positions are shown in Table 1, all atomic positions are provided in the Supporting Information. Tin and nitrogen atoms are in general position (8d), whereas oxygen is positioned on the 2-fold axis (4c). The electron-scattering factors of nitrogen and oxygen are too similar to distinguish these elements from the diffraction data. However, only the chosen assignment of sites represents an ordered structure, as the amounts of nitrogen and oxygen have a ratio of 2:1 and also the numbers of atomic positions of the sites 8d and 4c have a ratio of 2:1. There is no reason to assume nitrogen and oxygen to be disordered over both sites. Optimization of *Pbcn*- $\text{Sn}_2\text{N}_2\text{O}$ at ambient pressure using DFT confirms the soundness of the proposed structure of SNO. The calculated lattice parameters are $a=7.83010$, $b=5.66335$, $c=5.62591$ Å, (PBE values) and atomic coordinates are included in Table 1. The crystal structure of SNO is shown in Figure 2. All Sn atoms are symmetrically equivalent and have identical coordination, differing only by orientation or mirror symmetry. Within a single SnN_4O_2 octahedron the Sn–N and Sn–O bond lengths from experiment and theory are compared in Table 2. In the dense SNO structure the octahedra share edges and even faces, leading to short Sn–Sn distances of 3.269(5) and 3.091(7) Å, respectively.

Table 1. Atomic positions of SNO in space group *Pbcn* (No. 60) from experiment and DFT calculations.

Table 1. Atomic positions of SNO in space group <i>Pbcn</i> (No. 60) from experiment and DFT calculations.				
Experiment (dynamical refinement)				
Atom	<i>x</i>	<i>y</i>	<i>z</i>	<i>U</i> _{iso} [Å ²]
Sn1	0.11535(9)	0.24354(15)	0.52443(16)	0.0040(3)
N1	0.3507(5)	0.3841(7)	0.3952(9)	0.0012(8)
O1	0	0.4513(10)	0.25	0.0037(11)
DFT calculations				
Atom	<i>x</i>	<i>y</i>	<i>z</i>	
Sn1	0.1157	0.2376	0.5251	
N1	0.3507	0.3790	0.3954	
O1	0	0.4530	0.25	

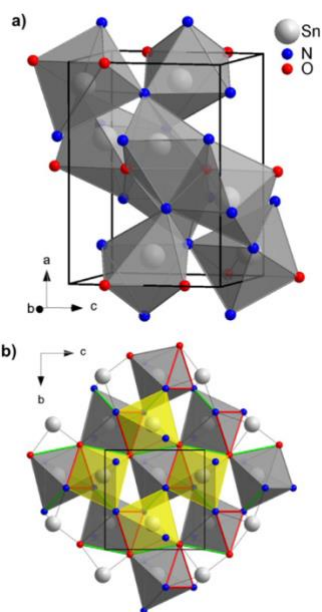
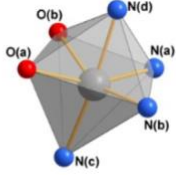


Figure 2. Crystal structure of SNO. a) Unit cell, showing the distorted octahedral coordination of Sn. b) View along the a-axis, showing grey and yellow coloured octahedra sharing faces (indicated as red triangles). Additional edge sharing (indicated as green lines) connects octahedra into chains running along the b-axis.

Table 2. Bond distances of $\text{Sn}_2\text{N}_2\text{O}$ from experiment in comparison to DFT calculations.

Table 2. Bond distances of $\text{Sn}_2\text{N}_2\text{O}$ from experiment in comparison to DFT calculations.			
Bond distance	DFT d [Å]	Experiment d [Å]	SnN_4O_2 octahedron with labelling of atoms
Sn–O(a)	2.169	2.110(3)	
Sn–O(b)	2.343	2.286(4)	
Sn–N(a)	2.202	2.190(5)	
Sn–N(b)	2.174	2.130(4)	
Sn–N(c)	2.136	2.124(4)	
Sn–N(d)	2.223	2.233(4)	

Equation of state

The bulk modulus of SNO $B_0=193(5)$ GPa with pressure derivative $B'=6.9(7)$ was determined from the pressure dependence of the unit-cell volume by fitting a 3rd order Birch–Murnaghan equation of state (EoS). The pressure dependence of the unit-cell volume is shown in Figure 3a, while the slope ($3/2 B_0 (B' - 4) \neq 0$) of the linear $\ln V$ -plot in Figure 3b clearly indicates the Birch–Murnaghan equation of state to be of 3rd order rather than 2nd order ($B'=4$). The high value of the pressure derivative B' may be explained by deviatoric stress, which can evolve in dense sintered powders with submicron grain size at high pressure even under a neon pressure medium.[16] Deviatoric stress shows up in the $\ln V$ -plot as a deviation of data points from a straight line in the high-pressure range. In our sample, however, such deviations are smaller than the experimental errors (cf. Figure 3b) and do not justify judging the highest-pressure data points as significantly affected by deviatoric stress.

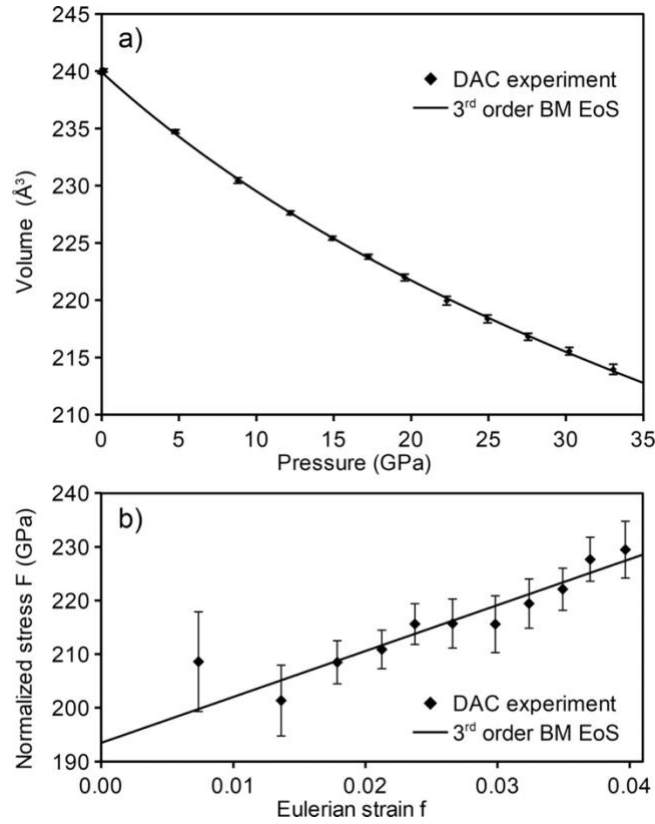


Figure 3. a) Pressure dependence of the unit-cell volume of SNO and the 3rd order Birch–Murnaghan EoS fitted to the data. b) The same EoS, rescaled to show the normalized stress F in dependence on Eulerian strain f . In the fF plot a 3rd order BM EoS displays as a straight line with y-axis intercept B_0 and slope proportional to $(B'-4)$.

DFT calculations

For $\text{Sn}_2\text{N}_2\text{O}$, we computed a bulk modulus B_0 of 177 and 208 GPa by using the PBE and SCAN functional, respectively. The experimentally determined bulk modulus fits within this range. This is about 10% higher than B_0 of spinel-type Sn_3N_4 , which we computed to 164 GPa [SCAN: 191 GPa] (exp. 148: 1.2 GPa).[17] The shear modulus G is 95 GPa using the PBE functional [SCAN: 112 GPa], about 10% lower than G of Sn_3N_4 . Combining B_0 and G yields a single-crystal hardness of $\text{Sn}_2\text{N}_2\text{O}$ of 11–12 GPa.[18] Since G is lower and B_0 is higher in comparison to Sn_3N_4 , the hardness value of $\text{Sn}_2\text{N}_2\text{O}$ can be expected to be 30–50% lower than the hardness of Sn_3N_4 (14–17 GPa). Band structure

calculations for $\text{Sn}_2\text{N}_2\text{O}$ by PBE and SCAN yield gaps of 0.3 and 0.6 eV, respectively. These values likely underestimate the true band gap. Using hybrid functionals we find a gap of 1.3 and 1.9 eV for HSE06[19] and PBE0[20] calculations, respectively. Thus, we expect that the gap of $\text{Sn}_2\text{N}_2\text{O}$ single crystals will be close to that of Sn_3N_4 , for which a value of 1.6 eV has been calculated[21] and 1.6:0.2 eV[3b] determined experimentally.

To rationalize the formation of $\text{Sn}_2\text{N}_2\text{O}$ in the high-pressure experiment we computed its enthalpy of formation from the binaries SnO_2 and Sn_3N_4 as a function of pressure. SnO_2 itself displays a rich high-pressure chemistry and has been subject of multiple experimental and computational studies.[7,22] At low pressure the rutile-type of SnO_2 is most favourable. We compute the pressure at which it transforms into the pyrite-type of SnO_2 to 9.6 GPa. Sn_3N_4 adopts the spinel structure at ambient pressure and transforms into post-spinel phases only above 40 GPa. Huang et al.[23] predicted CaTi_2O_4 - and CaFe_2O_4 -type orthorhombic structures at 40 and 60 GPa, respectively. On the other hand, Kearney et al.[24] predicted structures with space groups $P2_1/c$ and $R-3c$ at pressures above 40 and 87 GPa, respectively. At ambient pressure, the enthalpy of formation ΔH_f of $Pbcn$ - $\text{Sn}_2\text{N}_2\text{O}$ from the binaries is +0.56 eV/ $\text{Sn}_2\text{N}_2\text{O}$; taking the more favourable (at zero pressure) defect-spinel-type of $\text{Sn}_2\text{N}_2\text{O}$ the enthalpy difference is still +0.30 eV/ $\text{Sn}_2\text{N}_2\text{O}$. This indicates that $\text{Sn}_2\text{N}_2\text{O}$ is *meta*-stable with respect to decomposition into the binaries. Figure 4 shows that $\text{Sn}_2\text{N}_2\text{O}$ will form at 12.0 GPa [SCAN: 14.3 GPa] and remains stable against decomposition at higher pressures.

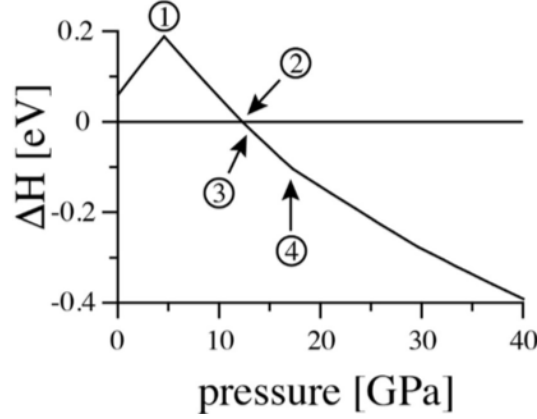


Figure 4. Reaction enthalpy (PBE results) of the reaction $\text{SnO}_2 + \text{Sn}_3\text{N}_4 \rightarrow 2\text{Sn}_2\text{N}_2\text{O}$ as a function of pressure. The labels indicate (1) transformation of spinel-type $\text{Sn}_2\text{N}_2\text{O}$ to *Pbcn*- $\text{Sn}_2\text{N}_2\text{O}$ (at 4.6 GPa), (2) $\Delta H_f = 0$ (12.0 GPa), (3) transformation of rutile-type SnO_2 to α - PbO_2 -type SnO_2 (12.5 GPa), and (4) transformation of α - PbO_2 -type SnO_2 to pyrite-type SnO_2 (17.2 GPa).

Searching for alternative structures of $\text{Sn}_2\text{N}_2\text{O}$ potentially appearing at low or high pressures, we found two relevant candidates. A “defect” spinel-type structure with disorder among the anions and vacancies on cation sites, constitutes the low-pressure modification of $\text{Sn}_2\text{N}_2\text{O}$. While we computed the lowest energy structure to adopt the ordered spinel In_2S_3 -type structure, we found other “defective” variants of spinel (e.g. with S.G. *P32m1*) within a few meV/atom. All “defect” spinel-types exhibit tetrahedrally and octahedrally coordinated cations. At ambient pressure, the “defect” spinel-type of $\text{Sn}_2\text{N}_2\text{O}$ is about 0.25 eV/ $\text{Sn}_2\text{N}_2\text{O}$ more favourable than the *Pbcn*-type. The transition to *Pbcn*- $\text{Sn}_2\text{N}_2\text{O}$ occurs at 5 GPa. The newly synthesized tin oxynitride remains the most favourable structure up to 95 GPa, when a new $\text{Sn}_2\text{N}_2\text{O}$ -III with seven- and eight-fold coordinated cations (CN=7.5 at 100 GPa) and orthorhombic (*Pmn21*) symmetry becomes favoured by enthalpy. $\text{Sn}_2\text{N}_2\text{O}$ -III distorts upon decompression into a monoclinic (*P21*) structure with reduced coordination.

Re-investigating the sequence of high-pressure structures of $\text{Si}_2\text{N}_2\text{O}$ [1c] we find that a *Pbcn*- $\text{Si}_2\text{N}_2\text{O}$ will succeed the Al_2O_3 -type only above 90 GPa. The Rh_2S_3 -type

structure (sometimes addressed as Rh_2O_3 -II type) with space group $Pbcn$ is known as a high-pressure phase of $\alpha\text{-Al}_2\text{O}_3$ (corundum, $R\text{-}3c$) above 113 GPa,[25] or $\alpha\text{-Fe}_2\text{O}_3$ (hematite, $R\text{-}3c$) above 41 GPa,[26] or Bixbyite-type In_2O_3 in the range of 10–25 GPa,[27] in which the latter compound shows also a metastable corundum-type phase at ≈ 6 GPa.

Conclusions

In conclusion, the discovered tin oxynitride $\text{Sn}_2\text{N}_2\text{O}$ with space group $Pbcn$ (Rh_2S_3 -type structure) is another example demonstrating the potential of high-pressure synthesis to access novel materials. Tin is in six-fold coordination in the Rh_2S_3 -type structure in contrast to the sinoite-type oxynitrides of Si and Ge with four-fold metal coordination. Tin oxynitride was synthesized at high pressure and high temperature using a large volume press at beamline P61B, DESY, Hamburg. The compound forms from tin oxide and tin nitride only at high pressure and can be quenched to ambient pressure retaining its high-pressure structure. The crystal structure of the novel compound was determined using synchrotron powder XRD in combination with single-crystal electron diffraction tomography from a 200 nm sized single crystal. DFT calculations predicted this structure to be stable above 12 GPa and to remain the most favourable one up to 95 GPa. The calculations also confirmed the ordered distribution of nitrogen and oxygen. The synthesized tin oxynitride may be considered for applications, for example, in the field of low band-gap semiconductors. From the viewpoint of fundamental solid-state chemistry, $\text{Sn}_2\text{N}_2\text{O}$ is a new member of inorganic compounds with the well-known Rh_2S_3 -type structure. It is also the first evidence for the existence of a crystalline ternary oxynitride of tin and complements and extends the well-known Group 14 element oxynitrides of silicon and germanium.

Experimental Section

Synthesis

Oxygen-containing tin nitride precursors were synthesized from a $\text{Sn}[\text{NMe}_2]_4$ complex using a two-stage ammonolysis procedure as described by Hector et al.[28] In the first stage, 7.93 mmol of $\text{Sn}[\text{N}(\text{CH}_3)_2]_4$ was dissolved in 50 mL THF and cooled to -78°C . Then, condensed ammonia was added by dropping method to the solution under constant stirring. A yellow powder was recovered after drying from the solvent and subsequently subjected to a second-stage standard ammonolysis at 150°C for 6 h and then to 400°C for 2 h (heating rate 2°C min^{-1} ; details are given in the Supporting Information). The product was characterized by XRD and elemental analysis using the combustion method (LECO tester). This precursor was subjected to HP-HT conditions (20 GPa and 1200–1500°C) in a Hall-type six-ram LVP (mavo press LPQ6 1500-100; Max Voggenreiter GmbH, Germany) installed at the P61B beamline at DESY, Hamburg.

XRD

X-ray diffraction of a crushed, synthesized sample (run# HH127, 20 GPa, 1200°C , Pt capsule) was performed using synchrotron radiation at the high-resolution powder beamline P02.1 of PETRA-III, DESY, Hamburg. The XRD pattern was quantitatively analysed by Rietveld refinement with the program GSAS-II[29] using instrumental profile parameters from a LaB_6 standard measured on the same instrument. A second sample (run# HH148, 20 GPa, 1500°C , Ta capsule) was characterized with $\text{CuK}\alpha$ radiation from a laboratory source. The pressure dependence of the unit-cell volume of SNO was measured in a diamond anvil cell (DAC) using synchrotron radiation at the extreme-condition beamline P02.2 of PETRA III, DESY, upon increasing the pressure from 0.14 to 33 GPa. The pressure in the DAC was measured with the ruby fluorescence method. The bulk modulus and its pressure derivative was determined by an equation of state fit [EosFit v5.2].[30] The volume at ambient pressure, $V_0=239.80(1) \text{ \AA}^3$, was

determined from the Rietveld refinement of an X-ray pattern measured with CuK α radiation using a sample from the same HP-HT run (#HH141, 20 GPa, 1300°C, Ta capsule) as for the DAC experiment.

Electron diffraction (ADT)

Automated diffraction tomography (ADT) experiments[10] were carried out at the electron microscopy centre (EMC-M) of the Johannes Gutenberg-University Mainz. A TEM Tecnai F30 ST equipped with a field emission gun at 300 kV was used. Sample imaging for crystal tracking during stage tilt was performed in m-STEM mode with a HAADF detector. Diffraction measurements were performed using nanoelectron-diffraction (NED) mode with a 10 μ m C2 aperture leading to a semi-parallel illumination with a beam size of 200 nm. Electron diffraction patterns were acquired with a Gatan CCD US4000 using 2k x 2k images taken with 1 s exposure time for each pattern. To provide a high tilt range a Fischione tomography sample holder was used (tilt range of -45–60° due to limitations on the grid). ADT data were collected with electron beam precession (precession electron diffraction, PED) to improve reflection intensity integration quality using a Digistar unit developed by NanoMEGAS SPRL (precession angle 1°).[31] A fast acquisition module recently developed was used for diffraction data acquisition applying sequential tilts of 1°. The Fast-ADT acquisition is re-ported in more detail in the upcoming article of Plana-Ruiz et al.[32] Data processing, 3D reconstruction, cell parameter determination and space group analysis as well as diffraction intensity extraction were performed with ADT3D (eADT) software.[33] Ab initio structure solution assuming the kinematic approximation ($\text{Int} \propto |F(hkl)|^2$) was performed by direct methods implemented in the program SIR2014 including as well difference Fourier mapping and least-squares refinement.[11] Scattering factors for electrons were taken from Doyle and Turner.[34] Kinematical structure refinement was performed with

shelxl2013[9] and dynamical structural refinement with JANA2006[35] after data extraction with PETS.[36]

DFT calculations

Calculations of total energy and volume were done within density functional theory as implemented in the Vienna ab initio simulation package (VASP).[37] The Generalized Gradient Approximation (GGA-PBE)[38] was used together with the projector-augmented-wave (PAW) method.[39] Consistency checks were done with the Strongly Conserved and Appropriately Normed (SCAN) function-al.[40] All results were obtained using a plane wave cut-off energy of 500 eV with forces converged to better than 1 meVÅ⁻¹. The Brillouin zone of each structure was sampled by *k*-point meshes with grid sizes smaller than 0.03 Å⁻¹. With the parameters above, enthalpy differences between structures are converged to better than 1 meV. Enthalpy and pressure of products and reactants are extracted from energy-volume data of corresponding structures. Computed elastic constants yield Young's modulus *E* and shear modulus *G* via the Voigt–Reuss–Hill approximation.[41] The approach of Chen et al.[18] was used to estimate single-crystal hard-ness. Searching for additional and alternative potential candidate structures of Sn₂N₂O we applied the USPEX code.[42] The code readily produced *Pbcn*-Sn₂N₂O and *Pmn*2₁-Sn₂N₂O among a manifold of structures. Low-pressure modifications of defective spinel-types were taken from previous works[1c,43] and outperformed models provided by the search algorithm.

Acknowledgements

Financial support by the Federal Ministry of Education and Re-search, Germany (BMBF, grants no.: 05K16WC2 & 05K13WC2). Parts of this research were carried out at the large volume press (LVP) beamline P61B, high-resolution powder diffraction beamline P02.1 and extreme conditions beamline P02.2 at PET-RAIII DESY, a member of the

Helmholtz Association (HGF). Authors also acknowledge valuable support from Stefan Sonntag (DESY), Nico Gaida (Uni Kiel/ Uni. Nagoya), and Satish Kulkarni (SEM assistance @DESY NanoLab). P.K. acknowledges financial support by NSF through awards OISE-1743701 and CMMI 1634448.

Conflict of interest

The authors declare no conflict of interest.

Keywords: density functional calculations · electron diffraction · high-pressure synthesis · synchrotron radiation · tin oxynitride

References

- [1] a)A. Zerr, G. Miehe, G. Serghiou, M. Schwarz, E. Kroke, R. Riedel, H. Fueß, P. Kroll, R. Boehler, *Nature* 1999, 400, 340–342; b)G. Serghiou, G. Miehe, O. Tschauner, A. Zerr, R. Boehler, *J. Chem. Phys.* 1999, 111, 4659– 4662; c)P. Kroll, M. Milko, *Z. Anorg. Allg. Chem.* 2003, 629, 1737–1750; d)J. C. Labbe, M. Billy, *Mater. Chem.* 1977, 2, 157–170; e)C. A. Andersen, K. Keil, B. Mason, *Science* 1964, 146, 256; f)C. Brosset, I. Idrestedt, *Nature* 1964, 201, 1211.
- [2] N. Nishiyama, R. Ishikawa, H. Ohfuji, H. Marquardt, A. Kurnosov, T. Taniguchi, B.-N. Kim, H. Yoshida, A. Masuno, J. Bednarcik, E. Kulik, Y. Ikuhara, F. Wakai, T. Irifune, *Sci. Rep.* 2017, 7, 44755.
- [3] a)T. D. Boyko, E. Bailey, A. Moewes, P. F. McMillan, *Phys. Rev. B* 2010, 81, 155207; b)T. D. Boyko, A. Hunt, A. Zerr, A. Moewes, *Phys. Rev. Lett.* 2013, 111, 097402.
- [4] M. E. Washburn, *J. Am. Ceram. Soc.* 1967, 50, 667–671.
- [5] J. D. Jorgensen, S. R. Srinivasa, J. C. Labbe, G. Roult, *Acta Crystallogr. Sect. B* 1979, 35, 141–142.
- [6] a)H. J. Gwon, N.-R. Kang, Y. Lee, S. O. Won, H. J. Chang, J.-W. Choi, C.-Y. Kang, S. K. Kim, B. Kwon, S. Nahm, J.-Y. Kim, J.-S. Kim, S.-H. Baek, *Chem. Mater.* 2016, 28, 7051–7057; b)S. Livraghi, N. Barbero, S. Agnoli, C. Barolo, G. Granozzi, F. Sauvage, E. Giamello, *Phys. Chem. Chem. Phys.* 2016, 18, 22617–22627; c)A. S. Bolokang, D. E. Motaung, C. J. Arendse, T. F. G. Muller, *J. Alloys Compd.* 2015, 622, 824–830; d)G. X. Zhou, S. J. Xiong, X. L. Wu, L. Z. Liu, T. H. Li, P. K. Chu, *Acta Mater.* 2013, 61, 7342–7347.
- [7] J. Haines, J. M. L8ger, *Phys. Rev. B* 1997, 55, 11144–11154.
- [8] F. Tessier, *Materials* 2018, 11, 1331.
- [9] G. Sheldrick, *Acta Crystallogr. Sect. A* 2008, 64, 112–122.

- [10] U. Kolb, T. Gorelik, E. Mugnaioli, *Mater. Res. Soc. Symp. Proc.* 2011, 1184-GG1101-1105.
- [11] M. C. Burla, R. Caliendo, B. Carrozzini, G. L. Cascarano, C. Cuocci, C. Giacobazzo, M. Mallamo, A. Mazzone, G. Polidori, *J. Appl. Crystallogr.* 2015, 48, 306–309.
- [12] W. H. Baur, A. A. Khan, *Acta Crystallogr. Sect. B* 1971, 27, 2133–2139. [13] G. Murken, M. Trçmel, *Z. Anorg. Allg. Chem.* 1973, 397, 117–126.
- [14] T. A. White, M. S. Moreno, P. A. Midgley, *Z. Kristallogr. Cryst. Mater.* 2010, 225, 56–66.
- [15] J. Pannetier, G. Denes, *Acta Crystallogr. Sect. B* 1980, 36, 2763–2765. [16] K. Glazyrin, N. Miyajima, J. S. Smith, K. K. M. Lee, *J. Geophys. Res. Solid Earth* 2016, 121, 3377–3392.
- [17] G. K. Pradhan, A. Kumar, S. K. Deb, U. V. Waghmare, C. Narayana, *Phys. Rev. B* 2010, 82, 144112.
- [18] X.-Q. Chen, H. Niu, D. Li, Y. Li, *Intermetallics* 2011, 19, 1275–1281.
- [19] A. V. Krukau, O. A. Vydrov, A. F. Izmaylov, G. E. Scuseria, *J. Chem. Phys.* 2006, 125, 224106.
- [20] J. P. Perdew, M. Ernzerhof, K. Burke, *J. Chem. Phys.* 1996, 105, 9982–9985.
- [21] C. M. Caskey, J. A. Seabold, V. Stevanovic, M. Ma, W. A. Smith, D. S. Ginley, N. R. Neale, R. M. Richards, S. Lany, A. Zakutayev, *J. Mater. Chem. C* 2015, 3, 1389–1396.
- [22] a)I. Erdem, H. H. Kart, T. Cagin, *J. Alloys Compd.* 2014, 587, 638–645; b)B. Zhu, C.-M. Liu, M.-B. Lv, X.-R. Chen, J. Zhu, G.-F. Ji, *Physica B+C* 2011, 406, 3508–3513; c)S. Ono, K. Funakoshi, A. Nozawa, T. Kikegawa, *J. Appl. Phys.* 2005, 97, 073523; d)S. Ono, E. Ito, T. Katsura, A. Yoneda, M. J. Walter, S. Urakawa, W. Utsumi, K. Funakoshi, *Phys. Chem. Miner.* 2000, 27, 618–622; e)Y. He, J. F. Liu, W. Chen, Y. Wang, H. Wang, Y. W. Zeng, G. Q. Zhang, L. N. Wang, J. Liu, T. D. Hu, H. Hahn, H. Gleiter, J. Z. Jiang, *Phys. Rev. B* 2005, 72, 212102; f)H. Hellwig, A. F. Goncharov, E. Gregoryanz, H.-k. Mao, R. J. Hemley, *Phys. Rev. B* 2003, 67, 174110; g)S. Endo, S. Nitawaki, T. Shige, Y. Akahama, T. Kikegawa, O. Shimomura, *High. Press. Res.* 1990, 4, 408–410.
- [23] M. Huang, Y. P. Feng, *J. Appl. Phys.* 2004, 96, 4015–4017.
- [24] J. S. C. Kearney, M. Grauzinyte, D. Smith, D. Sneed, C. Childs, J. Hinton, C. Park, J. S. Smith, E. Kim, S. D. S. Fitch, A. L. Hector, C. J. Pickard, J. A. Flores-Livas, A. Salamat, *Angew. Chem. Int. Ed.* 2018, 57, 11623–11628; *Angew. Chem.* 2019, 130, 11797–11802.
- [25] J. F. Lin, O. Degtyareva, C. T. Prewitt, P. Dera, N. Sata, E. Gregoryanz, H. K. Mao, R. J. Hemley, *Nat. Mater.* 2004, 3, 389–393.
- [26] E. Bykova, L. Dubrovinsky, N. Dubrovinskaia, M. Bykov, C. McCammon, S. V. Ovsyannikov, H. P. Liermann, I. Kuppenko, A. I. Chumakov, R. Ruffer, M. Hanfland, V. Prakapenka, *Nat. Commun.* 2016, 7, 10661.
- [27] A. Gurlo, D. Dzivenko, P. Kroll, R. Riedel, *Phys. Status Solidi RRL* 2008, 2, 269–271.
- [28] X. Li, A. L. Hector, J. R. Owen, S. I. U. Shah, *J. Mater. Chem. A* 2016, 4, 5081–5087.
- [29] B. H. Toby, R. B. Von Dreele, *J. Appl. Crystallogr.* 2013, 46, 544–549. [30] R. J. Angel, *Rev. Mineral. Geochem.* 2000, 41, 35–59.
- [31] R. Vincent, P. A. Midgley, *Ultramicroscopy* 1994, 53, 271–282.

- [32] S. Plana-Ruiz, J. Portillo, Y. Krysiak, L. Fink, S. Estrad8, U. Kolb, unpublished results.
- [33] U. Kolb, E. Mugnaioli, T. E. Gorelik, *Cryst. Res. Technol.* 2011, 46, 542–554.
- [34] P. A. Doyle, P. S. Turner, *Acta Crystallogr. Sect. A* 1968, 24, 390–397.
- [35] V. Petr&cek, M. Dusek, L. Palatinus, *Z. Kristallogr. Cryst. Mater* 2014, 229, 345–352.
- [36] L. Palatinus, P. Brazda, M. Jelinek, J. Hrda, G. Steciuk, M. Klementova, *Acta Crystallogr. Sect. B* 2019, 75, 512–522.
- [37] a)P. Hohenberg, W. Kohn, *Phys. Rev.* 1964, 136, B864–B871; b)G. Kresse, J. Furthmeller, *J. Comp. Mater. Sci.* 1996, 6, 15–50; c)G. Kresse, J. Hafner, *Phys. Rev. B* 1993, 47, 558–561; d)G. Kresse, J. Hafner, *Phys. Rev. B* 1994, 49, 14251–14269.
- [38] a)J. P. Perdew, K. Burke, M. Ernzerhof, *Phys. Rev. Lett.* 1996, 77, 3865–3868; b)J. P. Perdew, K. Burke, M. Ernzerhof, *Phys. Rev. Lett.* 1997, 78, 1396.
- [39] a)P. E. Bl&chhl, *Phys. Rev. B* 1994, 50, 17953–17979; b)G. Kresse, D. Joubert, *Phys. Rev. B* 1999, 59, 1758–1775.
- [40] W. H. Sun, A. Holder, B. Orvananos, E. Arca, A. Zakutayev, S. Lany, G. Ceder, *Chem. Mater.* 2017, 29, 6936–6946.
- [41] a)W. Voigt, *Lehrbuch der Kristallphysik*, B. B. Teubner, Leipzig, 1928; b)A. Reuss, *J. Appl. Math. Mech.* 1929, 9, 49–58; c)R. Hill, *Proc. Phys. Soc. London Sect. A* 1952, 65, 349–354.
- [42] a)A. O. Lyakhov, A. R. Oganov, H. T. Stokes, Q. Zhu, *Comput. Phys. Commun.* 2013, 184, 1172–1182; b)A. R. Oganov, C. W. Glass, *J. Chem. Phys.* 2006, 124, 244704; c)A. R. Oganov, A. O. Lyakhov, M. Valle, *Acc. Chem. Res.* 2011, 44, 227–237.

Summary

A new *Pbcn*-Sn₂N₂O with all Sn six-fold coordinated was synthesized through high-pressure experiments and characterized through powdered X-ray diffraction and automated diffraction tomography. The experimental bulk modulus of *Pbcn*-Sn₂N₂O was determined to be 193(5) GPa. Using DFT[1] we calculated the bulk modulus of *Pbcn*-Sn₂N₂O to be within a range of 177 – 208 GPa agreeing with experiment. Additionally, by calculating the single crystal hardness of *Pbcn*-Sn₂N₂O we estimated the hardness of *Pbcn*-Sn₂N₂O to be 30 – 50% lower than the hardness of spinel-type Sn₃N₄. Band gap calculations with hybrid functionals[2, 3] indicated that the band gap of *Pbcn*-Sn₂N₂O was in the range of the band gap of Sn₃N₄. In rationalizing the formation of *Pbcn*-Sn₂N₂O, we calculated ΔH_f of *Pbcn*-Sn₂N₂O from the binaries to be positive at ambient pressure indicating that the experimentally recovered *Pbcn*-Sn₂N₂O is metastable with respect to decomposition into binary compounds at ambient pressures. Furthermore, calculations of enthalpy as a function of pressure showed that *Pbcn*-Sn₂N₂O becomes stable with respect to decomposition into binary compounds at 12 GPa and remains the most thermodynamically favored form of *Pbcn*-Sn₂N₂O until 95 GPa.

References

- [1] P. Hohenberg, W. Kohn, Inhomogeneous Electron Gas, Physical Review 136(3B) (1964) B864-B871.
- [2] A.V. Krukau, O.A. Vydrov, A.F. Izmaylov, G.E. Scuseria, Influence of the exchange screening parameter on the performance of screened hybrid functionals, The Journal of Chemical Physics 125(22) (2006) 224106.
- [3] J.P. Perdew, M. Ernzerhof, K. Burke, Rationale for mixing exact exchange with density functional approximations, The Journal of Chemical Physics 105(22) (1996) 9982-9985.

CHAPTER 3: DISCOVERY OF TERNARY SILICON TITANIUM NITRIDE WITH SPINEL-TYPE STRUCTURE

Motivation and Scope

A new ternary Si-Ti-N compound with spinel-structure type is fortunately discovered during high-pressure experiments. Perhydropolysilazane and tetrakis(dimethylamido)titanium are reacted together to synthesize a single-source precursor which is converted into an amorphous Si-Ti-N ceramic under an ammonia atmosphere at 1000°C. Subjecting the amorphous ceramic to 15-20 GPa and 1800 – 2000°C results in a sintered sample that is a mixture of c-TiN and spinel-Si₃N₄, with ternary spinel-type (Si_{1-x},Ti_x)₃N₄ nanocrystals embedded in the spinel-Si₃N₄. We use DFT[1] to perform combinatorial analysis in order to determine the site preference of Ti in spinel-type (Si_{1-x},Ti_x)₃N₄. From the most favorable structures of ternary spinel-type (Si_{1-x},Ti_x)₃N₄ that we find we compute the enthalpy of formation of the ternary compound from its binary phases. We use Bader charge analysis[2] to verify the experimental findings that Ti is present in spinel-type (Si_{1-x},Ti_x)₃N₄ in multiple oxidation states. Additionally, we compute elastic properties and band gaps.

References

- [1] P. Hohenberg, W. Kohn, Inhomogeneous Electron Gas, Physical Review 136(3B) (1964) B864-B871.
- [2] R.F.W. Bader, Atoms in Molecules: A Quantum Theory, Clarendon Press, Oxford, UK, 1990.

Discovery of Ternary Silicon Titanium Nitride with Spinel-Type Structure

Shrikant Bhat^{1*}, Abhijeet Lale², Samuel Bernard², Wei Zhang³, Ryo Ishikawa^{3,4},
Shariq Haseen⁵, Peter Kroll⁵, Leonore Wiehl⁷, Robert Farla¹, Tomoo Katsura⁶, Yuichi
Ikuhara³ and Ralf Riedel⁷

¹Deutsches Elektronen-Synchrotron DESY, D-22607 Hamburg, Germany

²University of Limoges, CNRS, IRCER UMR 7315, F-87000, Limoges, France

³Institute of Engineering Innovation, University of Tokyo, Bunkyo, Tokyo, 113-8656,
Japan

⁴Japan Science and Technology Agency, PRESTO, Kawaguchi, Saitama 332-0012, Japan

⁵Department of Chemistry and Biochemistry, University of Texas at Arlington,
Arlington, Texas 76019, United States

⁶Bayerisches Geoinstitut (BGI), University of Bayreuth, 95440 Bayreuth, Germany

⁷Technische Universität Darmstadt, Fachbereich Material- und Geowissenschaften,
Fachgebiet Disperse Feststoffe, Otto-Berndt-Str. 3, D-64287 Darmstadt, Germany

* Corresponding author: shrikant.bhat@desy.de

Abstract

Here we report on the discovery of a ternary silicon titanium nitride with the general composition $(\text{Si}_{1-x}\text{Ti}_x)_3\text{N}_4$ with $x = 0 < x < 1$ and spinel-type crystal structure. The novel nitride is formed from an amorphous silicon titanium nitride (SiTiN) precursor under high-pressure/high-temperature conditions in a large volume high-pressure device. Under the conditions of 15 – 20 GPa and 1800 - 2000°C, spinel-type $\gamma\text{-Si}_3\text{N}_4$ and rock salt-type c-TiN are formed. In addition, crystals of the discovered nano-sized ternary phase $(\text{Si}_{1-x}\text{Ti}_x)_3\text{N}_4$ embedded in $\gamma\text{-Si}_3\text{N}_4$ are identified. The ternary compound is formed due to

kinetically-controlled synthesis conditions and is analyzed to exhibit the spinel-type structure with ca. 8 atom% of Ti. The Ti atoms occur in both Ti^{3+} and Ti^{4+} oxidation states and are located on the Si sites. The ternary nano-crystals have to be described as $(\text{Si},\text{Ti})_3\text{N}_4$ with N-vacancies resulting in the general composition $(\text{Si}^{4+}_{1-x} \text{Ti}^{4+}_{x-\delta} \text{Ti}^{3+\delta})_3\text{N}_4$.

δ .

Introduction

Spinel-type silicon nitride $\gamma\text{-Si}_3\text{N}_4$ is a high-pressure phase of silicon nitride and has been discovered in 1999[1]. In the same year, from the group 14 element, spinel type Ge_3N_4 and Sn_3N_4 [3] have been found afterwards. Based on these experimental findings, Ching

	C	Si	Ge	Sn	Ti	Zr	Hf
C	C_3N_4	CSi_2N_4	CGe_2N_4	CSn_2N_4	CTi_2N_4	CZr_2N_4	
Si	SiC_2N_4	Si_3N_4	SiGe_2N_4	SiSn_2N_4	SiTi_2N_4	SiZr_2N_4	
Ge	GeC_2N_4	GeSi_2N_4	Ge_3N_4	GeSn_2N_4	GeTi_2N_4	GeZr_2N_4	
Sn	SnC_2N_4	SnSi_2N_4	SnGe_2N_4	Sn_3N_4	SnTi_2N_4	SnZr_2N_4	
Ti	TiC_2N_4	TiSi_2N_4	TiGe_2N_4	TiSn_2N_4	Ti_3N_4	TiZr_2N_4	
Zr	ZrC_2N_4	ZrSi_2N_4	ZrGe_2N_4	ZrSn_2N_4	ZrTi_2N_4	Zr_3N_4	ZrHf_2N_4
Hf						HfZr_2N_4	Hf_3N_4

Figure 1: Overview of some high-pressure nitrides experimentally synthesized and theoretically predicted, after W.-Y. Ching et al.[4]

et al. predicted a variety of binary and ternary nitrides including nitrides of transition metal elements[4]. In Figure 1, an updated selection of prominent high-pressure nitrides experimentally accomplished (blue background) and those theoretically predicted (white background) but not achieved yet are listed.

According to their calculations, 39 spinel-type nitrides are characterized by interesting functional and structural features ranging from super-hardness via semiconducting to metallic properties[5]. Later on, it has been found experimentally, that the transition metal high-pressure nitrides of $M = \text{Ti, Zr and Hf}$ with the stoichiometry M_3N_4 do not show the spinel-type structure as forecasted, but appear in the cubic Th_3P_4 structure-type[6]. Experimental studies verified that spinel nitride $\gamma\text{-Si}_3\text{N}_4$ in particular, but also the transition metal nitrides M_3N_4 with $M = \text{Zr, Hf}$ combine ultra-high hardness with high thermal stability against decomposition in different environments. This suggests their promising use in potential applications such as cutting tools[7-9]. Due to their predicted semiconducting behaviour, calculations showed that spinel-type nitrides exhibit interesting optoelectronic properties, which may lead to applications such as light-emitting diodes[4,10].

Figure 1 impressively reveals that the majority of the predicted ternary nitrides have not been synthesized yet. To the best of our knowledge, the spinel-type GeSi_2N_4 is the solitary ternary nitride successfully synthesized[11,12]. Other ternary nitrides remained unknown yet though projected in various studies. There are even more theoretical studies predicting the existence of ternary nitrides e.g. with perovskite-type-based structures[13] and others[14] which could further immensely extend the field of unknown nitrides. Recently, a few new ternary nitrides with different structure types were synthesized by Sun et al.[15,16] based on a calculated large stability map of the inorganic ternary metal nitrides. They reported thin films of Zn-based and Mg-based ternary nitrides with wurtzite-type and rock salt-type structures, respectively[16].

The forecasted ternary nitrides open up further numerous scientific questions related to synthesis, chemistry and properties of this interesting family of new materials. Novel synthesis approaches including high-pressure methods in combination with theoretical calculations offer a chance to find correct pressure/temperature conditions to realize the synthesis of the exemplarily mentioned and calculated nitrides[17].

In the present study, we report on a discovery of a ternary nitride formed between Si_3N_4 and Ti_3N_4 synthesized under high-pressure/temperature conditions, namely at pressures of 15 - 20 GPa and temperatures of 1800 - 2000°C in a large volume press. While the binary nitrides crystallize in different structure types (spinel-type for Si_3N_4 and Th_3P_4 -type for Ti_3N_4 [18]), the formed ternary nitride reveals the spinel-type structure and it is, therefore, considered that Si in $\gamma\text{-Si}_3\text{N}_4$ is substituted by Ti. In addition, the ternary $(\text{Si,Ti})_3\text{N}_4$ crystals are nano-sized and are embedded in $\gamma\text{-Si}_3\text{N}_4$ single crystals.

Results

Single-source-precursor synthesis.

High-pressure synthesis of inorganic metal nitrides requires appropriate precursor compounds, which contain all the elements of the targeted material to be obtained. In our study we first synthesized a single-source precursor (SSP) by the reaction of perhydropolysilazane (PHPS) with tetrakis(dimethylamido)titanium (TDMAT) according to the scheme given in Figure 2[19,20]. For this reaction, we set a Si:Ti atomic ratio of 5.

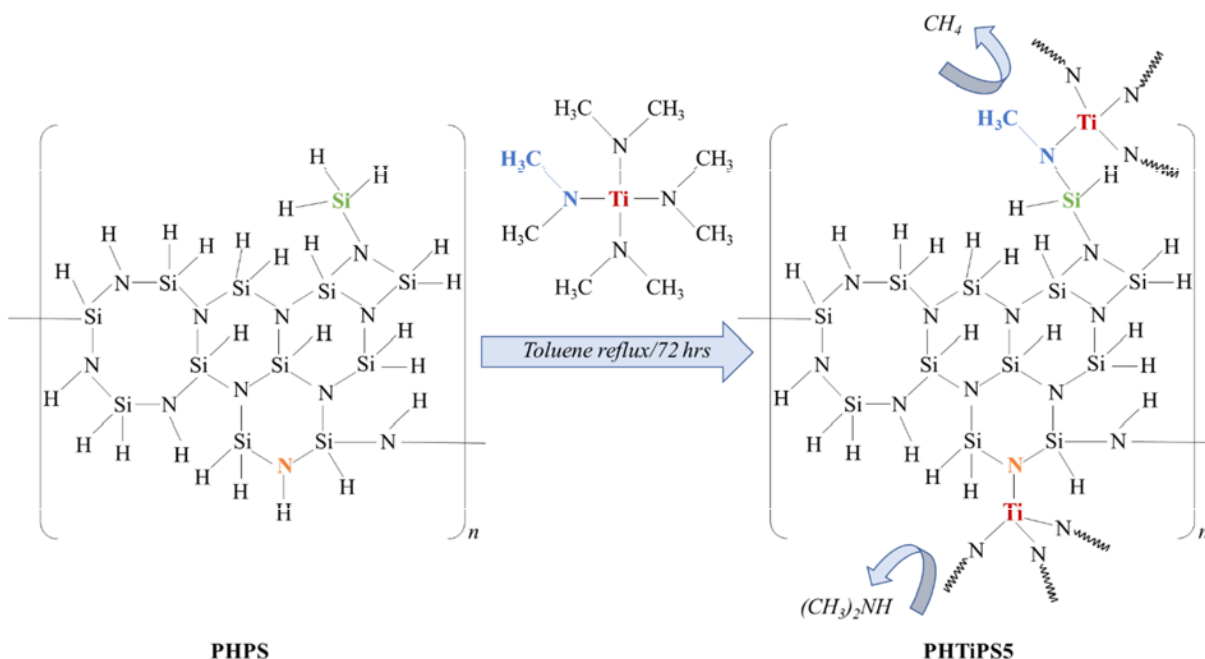


Figure 2: Synthesis procedure for the preparation of the SiTiN single-source precursor (SSP) according to reference[19].

The obtained SSP formed via the reaction of N-H- (dimethylamine release) and Si-H- (methane release) bonds from PHPS with the ligands of TDMAT is denoted as polytitanosilazane (PHTiPS5) and the following composition was obtained by chemical analysis: 38.4 wt% Si, 17.2 wt% Ti, 7.3 wt% H, 16.0 wt% N, 21.1 wt% C and 0.9 wt% O. By neglecting the oxygen contamination, a formal composition is derived from the analytical values: $Si_{1.0}Ti_{0.25}C_{1.2}N_{0.8}H_{5.2}$.

The SSP is finally converted to an amorphous/nanocrystalline SiTiN ceramic in ammonia atmosphere at 1000 °C with a ceramic yield of 73.25 wt%. Along with the amorphous background, the X-ray powder pattern of the synthesized SiTiN shows nanocrystalline features, which fit to the rock salt phase of TiN with a ~ 4.3 Å and a crystallite size of 2-3 nm. A quantitative elemental analysis of the SiTiN material revealed a composition of Si – 44.2 wt%; Ti – 18.9 wt%; N – 33.1 wt%; C – 0.02 wt% O – 3.8 wt%. The values are used to calculate a formal composition of the synthesized

powder by neglecting the carbon contamination: $\text{Si}_{1.0}\text{Ti}_{0.2}\text{N}_{1.5}\text{O}_{0.15}$ that represents the presence of $0.3 \text{ Si}_3\text{N}_4 + 0.2 \text{ TiN} + 0.07 \text{ SiO}_2$ of the respective thermodynamically phase compositions. Thus, the Si:Ti ratio in the ammonolyzed and pyrolyzed material amounts ca. 5 and reflects that of the molar ratio used for the synthesis of the SSP.

High-pressure synthesis.

In the second step, the acquired SiTiN powder is subjected to a high-pressure/high-temperature treatment. The high-pressure experiments were performed in a large volume press under pressures between 16 and 20 GPa and temperatures between 1800 and 2000°C. After pressure release, a compact and sintered body is isolated from the reaction chamber. A SEM image of a fracture surface of the sample exhibits a composite microstructure with dark and bright contrasted nanocrystals (see Figure 7). X-ray diffraction analysis of the powdered sample revealed the presence of spinel-type $\gamma\text{-Si}_3\text{N}_4$ and rocksalt-type c-TiN as well as some contamination with stishovite SiO_2 (Figure 3).

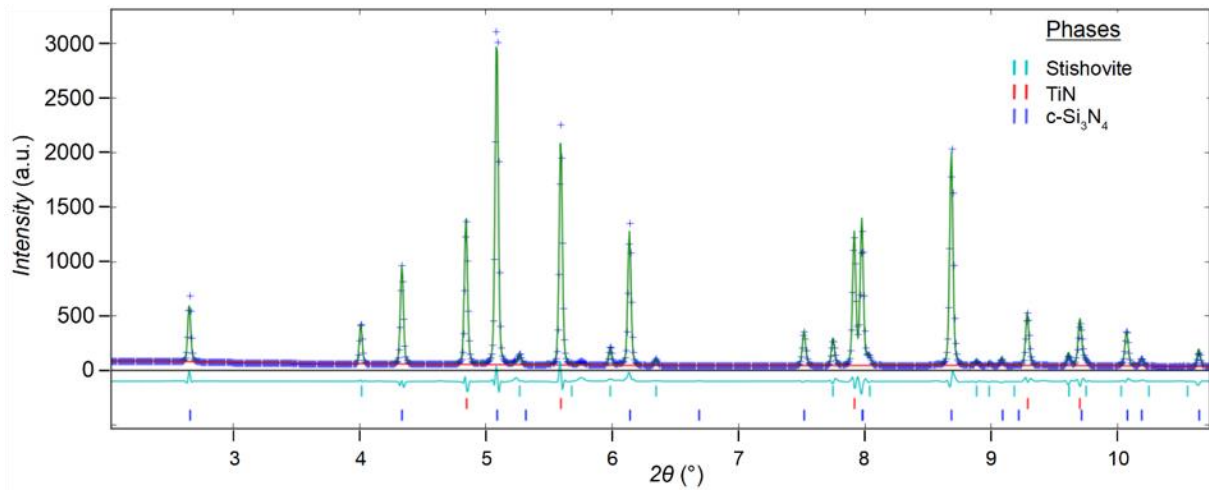


Figure 3: X-ray powder diffraction of SiTiN-run HH112 ($\lambda = 0.207109 \text{ \AA}$) and Rietveld refinement.

The fraction of the crystalline phases was obtained by Rietveld refinement of the XRD data. The fractions were 72.6 wt% $\gamma\text{-Si}_3\text{N}_4$, 20.2 wt% of c-TiN and 7.1 wt% Stishovite

(SiO₂) together with < 0.1 wt% Pt from the capsule material of the high- pressure experiment. The Si:Ti ratio thus remained ca. 5, and the bulk sample composition of the SiTiN starting material therefore did not significantly change during experimental high-pressure/temperature treatment.

Structural analysis via XRD and electron microscopy.

The average sizes of the synthesized γ -Si₃N₄ and c-TiN were derived from the peak widths of the XRD pattern, and found both 260 ± 90 nm. Since these grain sizes are too small for chemical composition analysis by SEM-EDS, the samples were observed using ADF-STEM. As shown in Figure 4(a), the sample consisted of two phases with different brightnesses. Since the brightness increases with increasing average atomic number, the brighter contrast grains should contain heavier elements, i.e. Ti. It is therefore concluded that the bright- and dark-contrast grains are c-TiN and γ -Si₃N₄, respectively. This evaluation was also confirmed by electron diffraction and EDX mapping (Figure 4b) of this region.

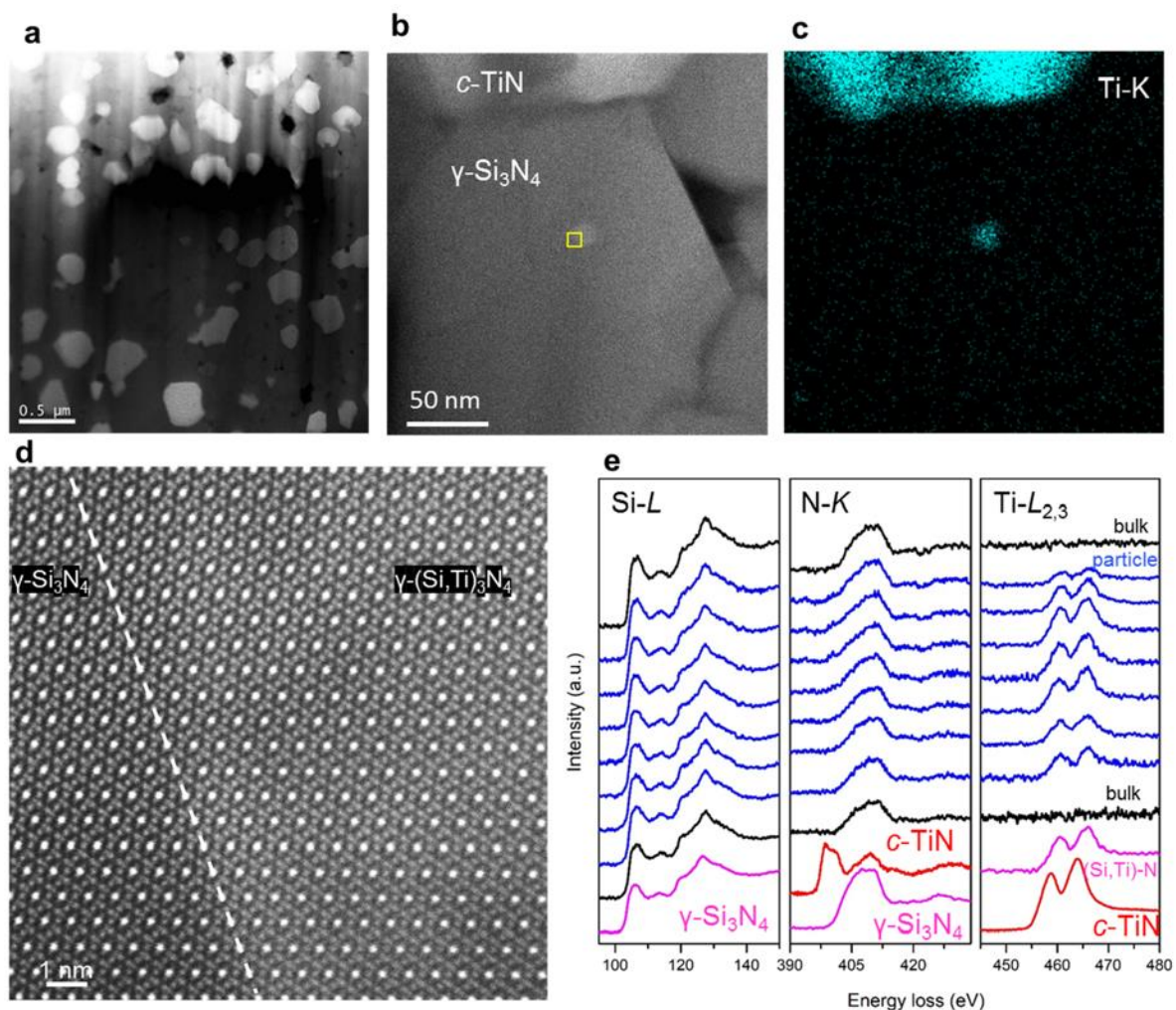


Figure 4: (a) Low-magnified ADF-STEM image, (b) ADF-STEM image obtained from a single grain, (c) Ti-K edge STEM-EDX mapping obtained from (b). (d) Atomic-resolution ADF-STEM image obtained from the yellow-framed section shown in (b). at the interface between γ -Si₃N₄ and ternary (Si,Ti)₃N₄ particle (e) EELS profiles of Si-L, N-K and Ti-L_{2,3} edges across the ternary (Si,Ti)₃N₄ nano-particle, where the black, blue, pink and red-colored profiles correspond to the bulk material, the nano-particle, γ -Si₃N₄ and SiTiN, and c-TiN, respectively.

On the close inspection of the grains, we found a third type of nanocrystals inside of the γ -Si₃N₄ grains that can be seen as a brighter dot contrast in the ADF-STEM image of Fig. 4(b), suggesting that the nanocrystal should contain Ti atoms. The embedded nanocrystals are around 10 – 20 nm in size and occur in the majority of the silicon nitride

host crystals. The distribution of nanoparticles in γ - Si_3N_4 grain can be found in the low-magnification of annular bright-field (ABF) STEM image (see Supplementary Note 1). To directly confirm the validity of Ti-concentration at the nano-particle, we performed STEM-EDX mapping and the map of Ti-*K* edge is shown in Fig. 4(c). On the basis of the STEM-EDX mapping, we elucidate that the nanocrystal contains Si, N and Ti atoms, and moreover the concentration of Si atoms is smaller than that in the vicinity of γ - Si_3N_4 . Thus, Ti atoms are considered to be in the substitutional form at Si atomic sites. It is important to note that no significant oxygen is found in the nanocrystals. Figure 4(d) shows an atomic-resolution ADF-STEM image viewed along the [110] orientation of γ - Si_3N_4 , including the interface between the nanocrystal and γ - Si_3N_4 . As indicated by the dotted line in Fig. 4(d), the nanocrystal (right-side) shows slightly brighter Z-contrast than that in the bulk of γ - Si_3N_4 , suggesting that the nanocrystal contains Ti atoms but the structure retains spinel-type with the coherent interface between the host γ - Si_3N_4 and the nanocrystal: the discovery of the ternary $(\text{Si},\text{Ti})_3\text{N}_4$. We note that although the boundary between the nanoparticle and γ - Si_3N_4 may be difficult to realize from the weak Z-contrast difference, it is the most evident in the Z-contrast intensity profile across the grain boundary and the simultaneously recorded ABF-STEM image (see Supplementary Note 2). For the further investigation, we performed EELS analysis across the nanocrystal as shown in Fig. 4(e), where the blue-, black- and red-colored profiles are related to the nanocrystal, γ - Si_3N_4 , and c-TiN, respectively. The pink colored profiles are obtained from the bulk of γ - Si_3N_4 and the nanoparticle (average for Ti- $L_{2,3}$ edge). The Si-*L*, and N-*K* edges of the nanocrystal are basically similar to those in γ - Si_3N_4 , which is well compatible with the observed atomic structure. The Ti- $L_{2,3}$ edges are localized within the nanocrystal, and the peak positions of the Ti- $L_{2,3}$ edge show slight upward shift compared with that in c-TiN, suggesting that Ti occurs in two oxidation states in the nanocrystal, namely Ti^{3+} and Ti^{4+} . In spinel-type structure, there are two atomic sites for cations, namely octahedral and tetrahedral coordination, and the Ti oxidation states for the sites

have to be considered as Ti^{3+} and Ti^{4+} . For the compensation of the total charge, the nanocrystal requires N vacancies, and we conclude that the formed ternary spinel structure has to be described as $(\text{Si}^{4+}_{1-x}\text{Ti}^{4+}_{x-\delta}\text{Ti}^{3+}_{\delta})^3\text{N}_{4-\delta}$, where we could not determine the Ti content (x) because the experimental spectroscopic information (EDX and EELS) is in 2D projection (the nanocrystal is embedded in $\gamma\text{-Si}_3\text{N}_4$ grain). However, from EELS we can roughly estimate the following ratio $\text{Ti}^{4+}:\text{Ti}^{3+} = (x-\delta):\delta \sim 0.7 : 0.3$, which leads to $\delta \sim 0.3 x$.

Thermodynamic considerations.

The composition of the synthesized ternary silicon titanium nitride solid solution is located on the tie line between the binary subsystems $\gamma\text{-Si}_3\text{N}_4$ and Ti_3N_4 as illustrated in the isothermal section of the phase diagram shown in Figure 5.

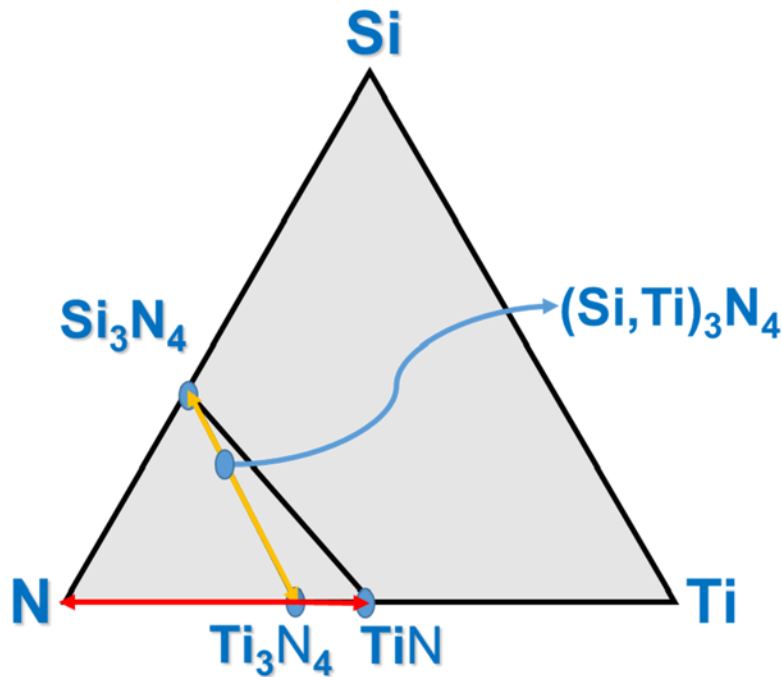
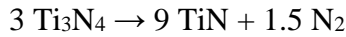


Figure 5: SiTiN ternary composition diagram with the known binary subsystems and the novel ternary SiTiN phase located on the tie line between $\gamma\text{-Si}_3\text{N}_4$ and Ti_3N_4 .

Accordingly, under the applied high-pressure/high-temperature conditions, amorphous SiTiN produced three phases, namely submicron-sized c-TiN with rocksalt-type structure and γ -Si₃N₄[1] grains with nano-sized inclusions of a ternary γ -(Si,Ti)₃N₄ phase, both with spinel-type structure. With respect to the phase diagram we may hypothesize that the ternary γ -(Si,Ti)₃N₄ phase partitions first into γ -Si₃N₄ and Ti₃N₄ (along the yellow colored tie line in Figure 5). However, Ti₃N₄ is thermodynamically unstable under our experimental conditions of 15-20 GPa and 1800-2000°C[21]. Thus, Ti₃N₄ readily decomposes into the thermodynamically stable phases c-TiN and gaseous N₂ along the red colored tie line of the binary Ti-N subsystems presented in Figure 5 and according to the following reaction equation:



Moreover, crystalline Ti₃N₄ cannot be recovered at ambient pressure[18,21], while the high-pressure phase of silicon-nitride shows an enormous metastability even at ambient pressure and can be heated up to 1400°C without any phase transformation[22]. Finally, once TiN is formed from the ternary γ -SiTiN phase, the resulting γ -Si₃N₄/c-TiN composite is thermodynamically stable at P > 10 GPa and metastable under ambient pressure.

Computation of Ti site preference and structure search.

Guided by the experimental data we started exploring spinel-type SiTiN. A first task was to evaluate site preference of Ti⁴⁺ substituting for Si⁴⁺ in Si₃N₄. We chose to work in the conventional unit cell of the spinel structure comprising 56 atoms. In a structure model of Si₂₃TiN₃₂ at ambient pressure, Ti prefers substitution of the octahedral site over a tetrahedral site. The energy difference we compute, however, is very small – only 0.01

eV. Increasing pressure increases slightly the preference for Ti to occupy the octahedral site to 0.07 eV at 15 GPa.

In a next step, we computed substitution of three Si by Ti simultaneously, still keeping Ti^{4+} . Thus, within the conventional unit cell we considered $\text{Si}_{21}\text{Ti}_3\text{N}_{32}$ and performed a structure search over all possible combinations of three Ti on cation sites. The model with the lowest enthalpy that emerged displays three Ti in octahedral sites coordinating to the same N (see Figure 6a and 6b). The small cluster formed by three fused TiN_6 -octahedra resembles a fragment of the rock-salt TiN structure, albeit in this case with Ti^{4+} rather than Ti^{3+} as in TiN. The next lowest enthalpy model, still containing only Ti^{4+} in octahedral sites is already 0.19 eV higher in energy (for the full 56 atom unit cell). The first model comprising Ti in a tetrahedral site comes out 0.28 eV higher in enthalpy than the ground state model of $\text{Si}_{21}\text{Ti}_3\text{N}_{32}$. Interestingly, the model of $\text{Si}_{21}\text{Ti}_3\text{N}_{32}$ with highest enthalpy (about 3 eV higher than the ground state model) also comprises all Ti in octahedral sites, but arranged with maximum distance from each other.

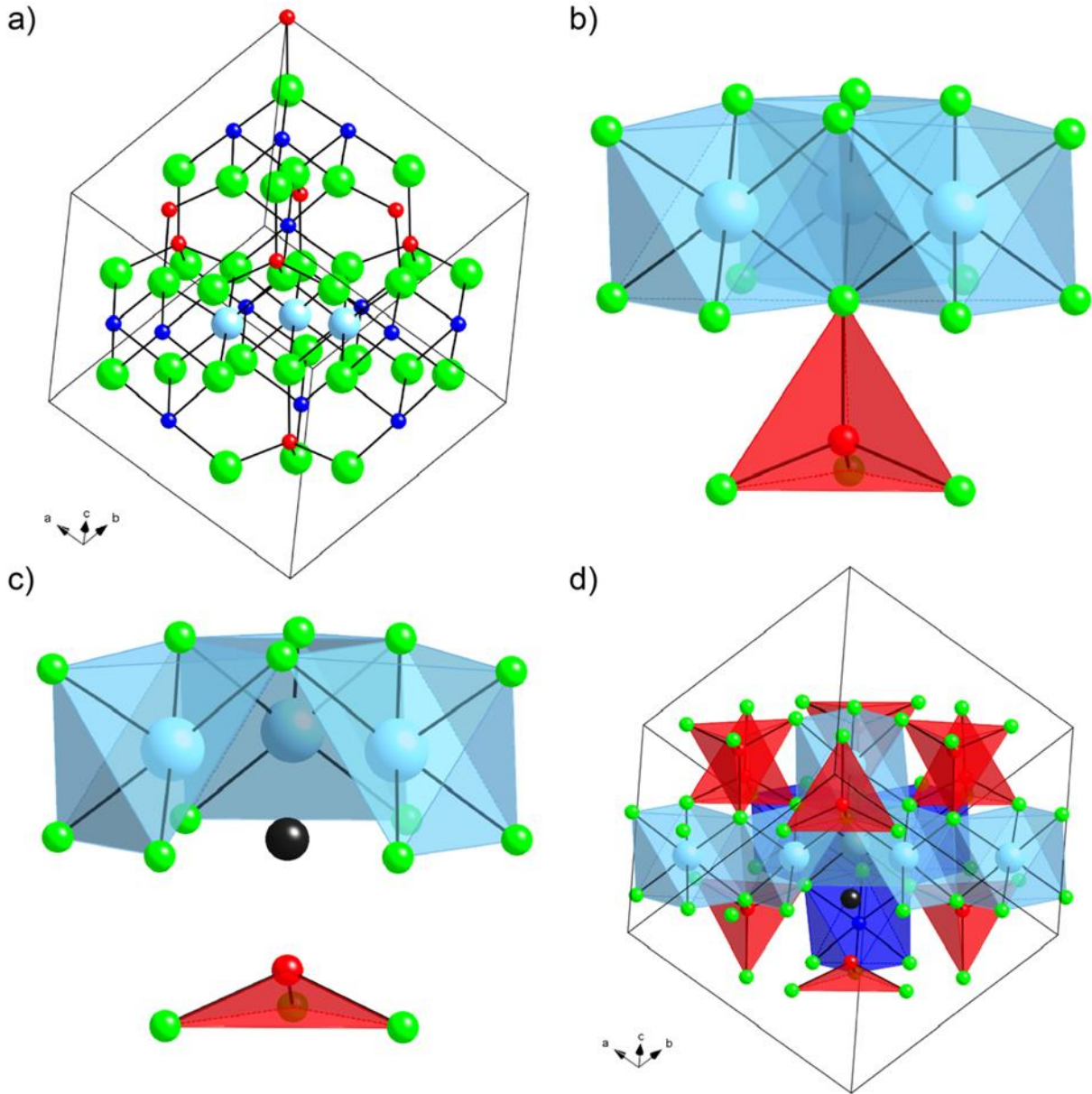


Figure 6: (a) Lowest-enthalpy structure of $\text{Si}_{21}\text{Ti}_3\text{N}_{32}$ and (b) its arrangement of fused TiN_6 -cluster. (c) Local environment of vacancy site in $\text{Si}_{21}\text{Ti}_3\text{N}_{31}$ exhibiting TiN_5V -octahedra (d) Lowest-enthalpy structure of $\text{Si}_{18}\text{Ti}_6\text{N}_{31}$ highlighting the chain of edge-sharing TiN_6 -/ TiN_5V -octahedra. Green spheres represent N, red and dark blue spheres tetrahedral and octahedral Si, respectively, and light blue (cyan) spheres Ti.

Introducing an anion vacancy does not change the picture of preferred cation arrangements in structures. Note that in models of $\text{Si}_{21}\text{Ti}_3\text{N}_{31}$ all three Ti are (formally) Ti^{3+} . Again, we found that Ti prefers octahedral sites and tends to cluster. With the

vacancy in the model, the lowest enthalpy structure displays all Ti adjacent to the defect as TiN_5V -octahedra (see Figure 6c). Alternative arrangements are now a bit closer in energy, the second lowest-enthalpy structure is only 0.12 eV higher than the lowest-enthalpy model. Among all combinations, the highest enthalpy structure is still one in which all Ti are in octahedral, but maximally dispersed in the structure.

We finally expanded our search to $\text{Si}_{18}\text{Ti}_6\text{N}_{31}$. This model displays half of Ti as Ti^{4+} and the other half as Ti^{3+} . We limited our combinatorial search on Ti in octahedral sites, and computed only a few models explicitly considering tetrahedral Ti as well. The lowest enthalpy configuration of $\text{Si}_{18}\text{Ti}_6\text{N}_{31}$ then shows only octahedral Ti, with three Ti in octahedral sites adjacent to the vacancy and the other Ti in different octahedral sites. Within the unit cell we considered, there now appears a chain of connected TiN_6 - TiN_5V -octahedra sharing edges along the [1 1 0] direction. Alternatives with more dispersed arrangements are less favorable in energy. This indicates once again the preference of Ti to cluster (see Figure 6d).

Enthalpy of formation.

To compute enthalpies of formation, ΔH_f , of the ternary SiTiN compounds we use Si_3N_4 , TiN (for Ti^{3+}), and spinel-type Ti_3N_4 as reference models. Note that a spinel-type Ti_3N_4 is not known, and only a Th_3P_4 -type Ti_3N_4 has been synthesized at 72 GPa in reference[18]. The lowest energy structure of Ti_3N_4 comprising Ti^{4+} is predicted to adopt a monoclinic structure, as earlier studies have shown[23,24].

Despite the fact that spinel-type Ti_3N_4 is not the ground state of Ti_3N_4 , we nevertheless find only positive values for ΔH_f of spinel-type SiTiN. This implies that its decomposition into binary compounds is favored by enthalpy. An anion vacancy and presence of some Ti^{3+} only increases the trend and so does pressure. With the ΔH_f spinel-type SiTiN being positive, we turn to estimate the entropy of mixing, ΔS_{mix} , arising from distributing Ti among the cation sites and a vacancy among anion sites[25,26].

Neglecting site preferences, which will only reduce our estimate of ΔS_{mix} , we estimate an upper bound of ΔS_{mix} of 749, 1160, 1430 J/(K·mol), for $\text{Si}_{21}\text{Ti}_3\text{N}_{32}$, $\text{Si}_{21}\text{Ti}_3\text{N}_{31}$, and $\text{Si}_{18}\text{Ti}_6\text{N}_{31}$, respectively. Since less vacancies are present than Ti cations, the cation mixing contributes to the total entropy of mixing more than the anion mixing. With $\Delta G = \Delta H_f - T\Delta S_{\text{mix}}$, we estimate that it would require temperatures greater than 5000 K to “stabilize” $\text{Si}_{21}\text{Ti}_3\text{N}_{31}$ and $\text{Si}_{18}\text{Ti}_6\text{N}_{31}$ against decomposition into the ternary system Si_3N_4 , TiN, and spinel-type Ti_3N_4 . We also considered a superstructure of $\alpha\text{-Si}_3\text{N}_4$ and substituted Si partially by Ti. This structure, thus, comprises tetrahedrally coordinated Ti^{4+} and may serve as a model for the precursor used during synthesis of spinel-type SiTiN. Not surprisingly, the lowest enthalpy structure of such a $\text{Si}_{21}\text{Ti}_3\text{N}_{32}$ displays all Ti clustered and bonding to the same N. Moreover, we find that incorporation of Ti slightly reduces the pressure of the transition by 0.4 GPa, if we compare our models of $\text{Si}_{21}\text{Ti}_3\text{N}_{32}$ and $\text{Si}_{21}\text{Ti}_3\text{N}_{32}$ discussed above relative to pure Si_3N_4 structures.

In summary, the occurrence of spinel-type SiTiN cannot be attributed to thermodynamical stability. A spinel-type $(\text{Si,Ti})_3\text{N}_4$ solid solution is less favorable than assemblages of separated phases of Si_3N_4 , TiN, and Ti_3N_4 . However, the spinel-type $(\text{Si,Ti})_3\text{N}_4$ solid solution is more favorable than the precursor system with tetrahedral Ti^{4+} mixed into a silicon nitride at 15 GPa. Therefore, formation of spinel-type $(\text{Si,Ti})_3\text{N}_4$ should be due to the sluggish kinetics, because formation of separate phases from the uniform precursor is a slower process than formation of a single phase of the spinel-type $(\text{Si,Ti})_3\text{N}_4$ solid solution.

Ti oxidation state.

An interesting question is related to the different charge states identified for Ti in spinel-type $(\text{Si,Ti})_3\text{N}_4$. The compound comprises both Ti^{3+} and Ti^{4+} . For a characterization of charges, we compute the lowest energy configuration of $\text{Si}_{21}\text{Ti}_3\text{N}_{32}$, $\text{Si}_{21}\text{Ti}_3\text{N}_{31}$, and $\text{Si}_{18}\text{Ti}_6\text{N}_{31}$, and use Bader charge analysis[27,28]. In $\text{Si}_{21}\text{Ti}_3\text{N}_{32}$, which displays Ti^{4+} , we

find 2.8 e[−] around the Ti according to the Bader charge analysis. On the other hand, Ti³⁺ in Si₂₁Ti₃N₃₁ exhibits higher Bader charges of 3.2 e[−]. In Si₁₈Ti₆N₃₁, which formally has equal proportions of Ti³⁺ and Ti⁴⁺, we indeed find half of the Ti with Bader charges of 2.0 e[−], while the other half displays Bader charges between 2.6 and 2.9 e[−]. This allows us to identify the two cohorts as Ti⁴⁺ and Ti³⁺, respectively. Noteworthy is that Ti³⁺ appears adjacent to the vacancy as TiN₅V-octahedra, while Ti⁴⁺ appears within TiN₆-octahedra.

Elastic properties.

We also computed elastic constants for all compounds and estimate elastic moduli (B , G) as well as Vickers hardness H_V , see Table 1. The Si₃N₄ is a notably hard material[29], but adding Ti reduces elastic properties and decrease hardness. The estimated hardness of Si₁₈Ti₆N₃₁ comes out to be close of half of that of Si₃N₄.

Table 1: Bulk modulus B , shear modulus G , and Vickers hardness H_V of Si₃N₄ and SiTiN compounds with the spinel structure type at ambient pressure using SCAN functional.

	B (GPa)	G (GPa)	H_V (GPa)
Si₃N₄	333	283	42
Si₂₁Ti₃N₃₂	327	248	33
Si₂₁Ti₃N₃₁	308	234	32
Si₁₈Ti₆N₃₁	292	204	26

Electronic properties.

We compute the band gap of γ -Si₃N₄ to 4.95 eV using the screened hybrid HSE-functional[30]. This aligns with previous calculations and available experimental data[31]. Replacing Si⁴⁺ by Ti⁴⁺ introduces localized unfilled d-states below the conduction band, ultimately decreasing the width of the band gap. Introducing a single

nitrogen vacancy creates an odd number of Ti^{3+} and results in a partially filled band in the middle of the gap.

Discussion

In summary, an amorphous SiTiN compound was synthesized by the reaction of perhydropolysilazane with tetrakis(dimethylamido)titanium and subsequent heat treatment in ammonia at 1000°C . The SiTiN was exposed to 15-20 GPa pressure and $1800\text{-}2000^\circ\text{C}$ in a large volume press to form a high-pressure $\gamma\text{-Si}_3\text{N}_4/\text{c-TiN}$ composite material for the first time. The special feature of the obtained composite is due to the discovery of an additional nanocrystalline ternary $\gamma\text{-(Si,Ti)}_3\text{N}_4$ phase with spinel-type structure embedded within the majority of the submicron $\gamma\text{-Si}_3\text{N}_4$ crystals. The $\gamma\text{-(Si,Ti)}_3\text{N}_4$ phase was analyzed in detail by TEM and EELS and the results clearly showed the presence of two types of Ti atoms, namely Ti^{3+} and Ti^{4+} , which in turn requires the formation of vacancies in the anion lattice. Therefore, the general formula of the discovered ternary spinel-type SiTiN has to be described as $(\text{Si}^{4+}_{1-x}\text{Ti}^{4+}_{x-\delta}\text{Ti}^{3+\delta})_3\text{N}_{4-\delta}$. According to theoretical calculations, Ti^{3+} appears adjacent to the vacancy as TiN_5V -octahedra, while Ti^{4+} appears within TiN_6 -octahedra. Moreover, all of the ternary SiTiN compounds have been calculated to be thermodynamically unstable with respect to the binary phases, which is in accordance with the experimental result, that finally a binary $\gamma\text{-Si}_3\text{N}_4/\text{c-TiN}$ high-pressure composite is formed.

In consequence, it has to be noted that the synthesis of the ternary spinel-type SiTiN phase is kinetically controlled and requires an appropriate precursor material (SSP) with Ti^{4+} atoms in tetrahedral coordination together with tetrahedrally coordinated Si in amorphous silicon nitride. A direct reaction of Si_3N_4 with TiN to form a ternary high-pressure SiTiN phase is thermodynamically impossible and has not been observed yet experimentally. The present work encourages to study other SSP-derived Si-based

systems containing transition metal atoms other than Ti to form innovative high-pressure composite materials and novel inorganic ternary metal nitrides.

Methods

Single-Source-Precursor Synthesis

A single source precursor (SSP) of titanium-modified perhydropolysilazane (PHPS) was synthesized by a reaction between PHPS and tetrakis(dimethylamido)titanium (TDMAT) with a molar Si:Ti ratio 5:1 (labelled as PHPTiS5) according to our previous reports[19,20].

The manipulation of the PHPTiS5 sample was made in an argon-filled glove box (Jacomex, Campus-type; O₂ and H₂O concentrations kept at 0.1 ppm and 0.8 ppm, respectively) to be ground in an agate mortar and then placed in alumina boats. Alumina boats containing the polymers were introduced in tubes under protective atmospheres (argon) to be transferred under argon flow into a silica tube inserted in a horizontal furnace [THERMOCONCEPT OS50/450/12]. After evacuation of the furnace under dynamic vacuum (0.1 mbar), the tube was refilled with ammonia up to atmospheric pressure and a continuous flow of ammonia was maintained through the tube. Subsequently, the samples were pyrolyzed at a heating rate of 5 °C min⁻¹ to 1000°C (dwell time for 2 h) in order to produce the SiTiN precursor (labelled as PHPTiS5_1000). After cooling at a rate of 2°C min⁻¹ under nitrogen flow, the PHPTiS5_1000 was used as a starting material for the subsequent high pressure synthesis.

The silicon and titanium contents of the synthesized SiTiN powders were measured by inductively coupled plasma/optical emission spectroscopy (ICP/OES) [Optima 8300 optical emission spectrometer Perkin Elmer, USA]. The carbon and the oxygen, nitrogen and hydrogen contents of the powders were determined by combustion elemental analysis [Carbon (EMIA-321V), O/N/H analyzer (EMGA-830) Horiba, Japan].

The phase composition of samples prepared at 1000°C was determined by powder X-ray diffraction (XRD) with a Bruker AXS D8 Discover and CuK α radiation. The scans were performed in the range of $2\theta \in \langle 15^\circ; 90^\circ \rangle$ with a step of 0.015° and an exposure time of 0.7 s. The diffraction patterns were analyzed using the Diffrac + EVA software with the JCPDS-ICDD database.

High-Pressure Synthesis

High-pressure high-temperature experiments were performed in a Hall-type six-ram LVP (mavo press LPQ6 1500-100; Max Vöggenreiter GmbH, Germany) installed at the P61B beamline at DESY, Hamburg³². The samples were synthesized in a 14/7 or 10/4 assembly of eight tungsten carbide cubes (32 mm Fujilloy TF08) at the target pressures. A Cr₂O₃-doped MgO octahedron was used as the pressure-transmitting medium. The starting material was cold pressed into pellet form ($h = 1.6$ mm, $\phi = 1.9$ mm) using a platinum foil before placing in the MgO tube. The octahedral assembly was compressed to a pressure of 16 and 20 GPa and, at pressure, heated to a chosen temperature in the range of 1800 - 2000°C and held for 30 min. Pressure was calibrated at room temperature using the semiconductor to metal transition of GaP at 22 GPa^[33]. Sample temperatures were estimated using power-temperature relations calibrated in a separate run using a W5%Re/W26%Re thermocouple (C-type). Overview of experimental conditions with the corresponding run numbers are given in Table 2.

Table 2: Overview of HP-HT experiments with run number, assembly, pressure, temperature, heating duration and capsule materials.

Run No	Sample	Assembly	Pressure (GPa)	Temperature (°C)	Heating duration (min)	Capsule material
HH113	SiTiN-II	14/7	16	1800	30	Pt
HH109	SiTiN-II	10/4	20	1800	30	Pt
HH112	SiTiN-II	10/4	20	2000	20	Pt

After recovery, each sample was found dense and fine-grained in appearance (see Figure 7).

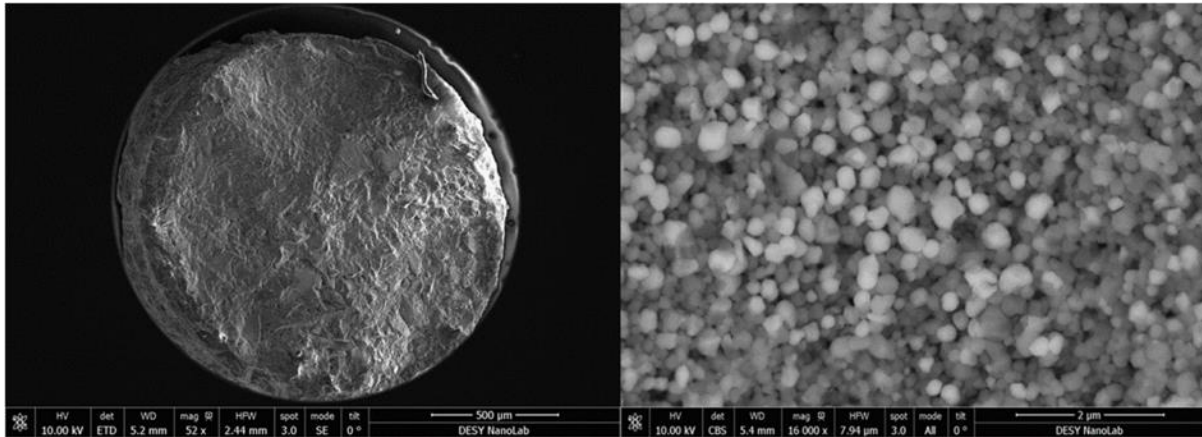


Figure 7: SEM micrographs (run# HH112) showing (left) an overview of the sample pellet after HP-HT and (right) a fracture surface with spinel-type γ - Si_3N_4 and rock salt-type c-TiN crystals. XRD of crushed samples was obtained using synchrotron radiation at the high-resolution powder diffraction beamline P02.1 of PETRA-III, DESY, Hamburg. The XRD pattern was quantitatively analyzed by Rietveld refinement with the program GSAS-II[34].

Electron Microscopy

For the preparation of electron transparent thin specimen, the synthesized bulk sample was processed by focused ion beam (Helios G4, Thermo Fisher Scientific) and subsequently, to clean the specimen, Ar ion beam milling was performed at 0.5 kV in the final step. For the atomic and electronic structure analysis, we used an aberration-corrected STEM (JEM ARM-200CF, JEOL Ltd.), equipped with an annular dark-field (ADF) and annular bright-field (ABF) detectors, EEL spectrometer (Enfinium, Gatan Inc.) and dual electron dispersive X-ray (EDX) spectrometers. The electron microscope was operated at 200 kV. For atomic-scale imaging and spectroscopy, the illumination semi-angle was 24 mrad, and the ABF and ADF detectors span from 12 to 24 and 64 to 200 mrad, respectively, where a typical beam current was 20 pA.

Computational Method

All calculations were performed using density functional theory (DFT) as implemented in the Vienna ab initio simulation package (VASP).[35-38] For correlation and exchange we use the Strongly Conserved and Appropriately Normed (SCAN) functional together with the projector-augmented-wave (PAW) method.[39-41] Reported results were obtained using a plane wave cut-off energy of 500 eV. We sample the Brillouin zone of the conventional unit cell and all derived structures using a $2 \times 2 \times 2$ k -point mesh. With parameters reported above, enthalpy differences between structures are converged to better than 0.005 eV per conventional unit cell. Different models of spinel-type $\text{Si}_{21}\text{Ti}_3\text{N}_{32}$ and $\text{Si}_{21}\text{Ti}_3\text{N}_{31}$ were investigated by testing all the possible combinations of Ti at Si octahedral and tetrahedral sites. We first identified lowest enthalpy structures by static calculations without further relaxation. Structures with low enthalpies were further optimized until forces converged to 0.01 eV/Å and residual stresses are below 0.01 GPa. It turned out that this optimization does not change the ranking of the models to a significant extent. Lowest enthalpy models of each composition were further optimized

(forces converged to 5 meV/Å) and used for subsequent calculations. The lowest enthalpy model of $\text{Si}_{18}\text{Ti}_6\text{N}_{31}$ attained monoclinic structure (SpGr. $C1m1$ (8); $a=7.905$ Å, $b = 7.905$ Å, $c=7.923$ Å, $\alpha = 89.94^\circ$, $\beta = 89.94^\circ$, $\gamma = 89.68^\circ$), but displayed only small distortion away from a pseudo-cubic cell. Substituting Ti for Si increases the cell volume relative to spinel- Si_3N_4 even in models with a vacancy.

References

- [1] Zerr, A.; Miehe, G.; Serghiou, G.; Schwarz, M.; Kroke, E.; Riedel, R.; Fueß, H.; Kroll, P.; Boehler, R. Synthesis of cubic silicon nitride. *Nature* **1999**, *400*, 340.
- [2] Serghiou, G.; Miehe, G.; Tschauner, O.; Zerr, A.; Boehler, R. Synthesis of a cubic Ge_3N_4 phase at high pressures and temperatures. *J. Chem. Phys.* **1999**, *111*, 4659.
- [3] Scotti, N.; Kockelmann, W.; Senker, J.; Trassel, S.; Jacobs, H. Sn_3N_4 , a tin(IV) nitride - Syntheses and the first crystal structure determination of a binary tin-nitrogen compound. *Z Anorg Allg Chem* **1999**, *625* (9), 1435.
- [4] Ching, W. Y.; Mo, S. D.; Ouyang, L. Z.; Rulis, P.; Tanaka, I.; Yoshiya, M. Theoretical prediction of the structure and properties of cubic spinel nitrides. *J Am Ceram Soc* **2002**, *85* (1), 75.
- [5] Ching, W. Y.; Mo, S. D.; Tanaka, I.; Yoshiya, M. Prediction of spinel structure and properties of single and double nitrides. *Physical Review B* **2001**, *63* (6).
- [6] Zerr, A.; Miehe, G.; Riedel, R. Synthesis of cubic zirconium and hafnium nitride having Th_3P_4 -structure. *Nat. Mater.* **2003**, *2*, 185.
- [7] Zerr, A.; Riedel, R.; Sekine, T.; Lowther, J. E.; Ching, W. Y.; Tanaka, I. Recent advances in new hard high-pressure nitrides. *Adv. Mater.* **2006**, *18*, 2933.
- [8] Zerr, A.; Kempf, M.; Schwarz, M.; Kroke, E.; Göken, M.; Riedel, R. Elastic moduli and hardness of cubic silicon nitride. *J. Am. Ceram. Soc.* **2002**, *85*, 86.
- [9] Chhowalla, M.; Unalan, H. E. Thin films of hard cubic Zr_3N_4 stabilized by stress. *Nature Materials* **2005**, *4* (4), 317.
- [10] Ching, W. Y.; Mo, S. D.; Ouyang, L.; Tanaka, I.; Yoshiya, M. Prediction of the new spinel phase of Ti_3N_4 , and SiTi_2N_4 and the metal-insulator transition. *Physical Review B* **2000**, *61* (16), 10609.
- [11] Boyko, T. D.; Bailey, E.; Moewes, A.; McMillan, P. F. Class of tunable wide band gap semiconductors $\text{g}-(\text{Ge}_x\text{Si}_{1-x})_3\text{N}_4$. *Phys. Rev. B* **2010**, *81* (15), 155207.
- [12] Soignard, E.; McMillan, P. F.; Leinenweber, K. Solid solutions and ternary compound formation among Ge_3N_4 - Si_3N_4 nitride spinels synthesized at high pressure and high temperature. *Chem. Mater.* **2004**, *16*, 5344.
- [13] Sarmiento-Perez, R.; Cerqueira, T. F. T.; Korbel, S.; Botti, S.; Marques, M. A. L. Prediction of Stable Nitride Perovskites. *Chemistry of Materials* **2015**, *27* (17), 5957.
- [14] Beznosikov, B. V.; Aleksandrov, K. S. Prediction of some antiperovskites. *J Struct Chem* **2002**, *43* (5), 798.
- [15] Sun, W. H.; Bartel, C.; Arca, E.; Bauers, S.; Matthews, B.; Orvananos, B.; Chen, B. R.; Toney, M.; Schelhas, L.; Tumas, W. et al. Map of the inorganic ternary metal nitrides. *Abstr Pap Am Chem S* **2019**, 257.
- [16] Sun, W. H.; Bartel, C. J.; Arca, E.; Bauers, S. R.; Matthews, B.; Orvananos, B.; Chen, B. R.; Toney, M. F.; Schelhas, L. T.; Tumas, W. et al. A map of the inorganic ternary metal nitrides. *Nature Materials* **2019**, *18* (7), 732.
- [17] Riedel, R.; Yu, Z. J. Charting stability space. *Nature Materials* **2019**, *18* (7), 664.
- [18] Bhadram, V. S.; Liu, H. Y.; Xu, E. S.; Li, T. S.; Prakapenka, V. B.; Hrubciak, R.; Lany, S.; Strobel, T. A. Semiconducting cubic titanium nitride in the Th_3P_4 structure. *Phy Rev Mater* **2018**, *2* (1).
- [19] Bechelany, M. C.; Proust, V.; Gervais, C.; Ghisleni, R.; Bernard, S.; Miele, P. In Situ Controlled Growth of Titanium Nitride in Amorphous Silicon Nitride: A General

- Route Toward Bulk Nitride Nanocomposites with Very High Hardness. *Advanced Materials* **2014**, 26 (38), 6548.
- [20] Bechelany, M. C.; Proust, V.; Lale, A.; Miele, P.; Malo, S.; Gervais, C.; Bernard, S. Nanocomposites through the Chemistry of Single-Source Precursors: Understanding the Role of Chemistry behind the Design of Monolith-Type Nanostructured Titanium Nitride/Silicon Nitride. *Chem-Eur J* **2017**, 23 (4), 832.
- [21] Alkhalidi, H.; Kroll, P. Chemical Potential of Nitrogen at High Pressure and High Temperature: Application to Nitrogen and Nitrogen-Rich Phase Diagram Calculations. *Journal of Physical Chemistry C* **2019**, 123 (12), 7054.
- [22] Jiang, J. Z.; Kragh, F.; Frost, D. J.; Stahl, K.; Lindelov, H. Hardness and thermal stability of cubic silicon nitride. *J. Phys.-Condes. Matter* **2001**, 13 (22), L515.
- [23] Su, V.; Kroll, P. Reinvestigation and Clarification of Titanium (IV) Nitride, Ti_3N_4 : Prediction of Low Energy Structures and a New Ground State. *Report for Welch Summer Student Program* **2011**, 5.
- [24] Weinberger, C. R.; Yu, X. X.; Yu, H.; Thompson, G. B. Ab initio investigations of the phase stability in group IVB and VB transition metal nitrides. *Comput. Mater. Sci.* **2017**, 138, 333.
- [25] Kroll, P.; Milko, M. Theoretical Investigation of the Solid State Reaction of Silicon Nitride and Silicon Dioxide forming Silicon Oxynitride ($\text{Si}_2\text{N}_2\text{O}$) under Pressure. *Zeitschrift für anorganische und allgemeine Chemie* **2003**, 629 (10), 1737.
- [26] Kroll, P.; Dronskowski, R.; Martin, M. Formation of spinel-type gallium oxynitrides: a density-functional study of binary and ternary phases in the system Ga–O–N. *Journal of Materials Chemistry* **2005**, 15 (32), 3296.
- [27] Bader, R. F. W. *Atoms in Molecules: A Quantum Theory*; Clarendon Press: Oxford, UK, 1990.
- [28] Tang, W.; Sanville, E.; Henkelman, G. A grid-based Bader analysis algorithm without lattice bias. *Journal of Physics: Condensed Matter* **2009**, 21 (8), 084204.
- [29] Zerr, A.; Kempf, M.; Schwarz, M.; Kroke, E.; Göken, M.; Riedel, R. Elastic Moduli and Hardness of Cubic Silicon Nitride. **2002**, 85 (1), 86.
- [30] Krukau, A. V.; Vydrov, O. A.; Izmaylov, A. F.; Scuseria, G. E. Influence of the exchange screening parameter on the performance of screened hybrid functionals. *Journal of Chemical Physics* **2006**, 125 (22).
- [31] Boyko, T. D.; Hunt, A.; Zerr, A.; Moewes, A. Electronic Structure of Spinel-Type Nitride Compounds Si_3N_4 , Ge_3N_4 , and Sn_3N_4 with Tunable Band Gaps: Application to Light Emitting Diodes. *Phys Rev Lett* **2013**, 111 (9).
- [32] Bhat, S.; Wiehl, L.; Haseen, S.; Kroll, P.; Glazyrin, K.; Leidreiter, P. G.; Kolb, U.; Farla, R.; Tseng, J. C.; Ionescu, E. et al. A Novel High-Pressure Tin Oxynitride $\text{Sn}_2\text{N}_2\text{O}$. *Chemistry* **2019**, DOI:10.1002/chem.201904529 10.1002/chem.201904529.
- [33] Ono, S.; Kikegawa, T. Determination of the phase boundary of GaP using in situ high pressure and high-temperature X-ray diffraction. *High Pressure Res* **2017**, 37 (1), 28.
- [34] Toby, B. H.; Von Dreele, R. B. GSAS-II: the genesis of a modern open-source all purpose crystallography software package. *J Appl Crystallogr* **2013**, 46, 544.
- [35] Kresse, G.; Hafner, J. Ab-initio Molecular-Dynamics for Liquid-Metals. *Physical Review B* **1993**, 47 (1), 558.

- [36] Kresse, G.; Hafner, J. Ab-Initio Molecular-Dynamics Simulation of the Liquid-Metal Amorphous-Semiconductor Transition in Germanium. *Physical Review B* **1994**, 49 (20), 14251.
- [37] Kresse, G.; Furthmüller, J. Efficiency of ab-initio total energy calculations for metals and semiconductors using a plane-wave basis set. *Comp Mater Sci* **1996**, 6 (1), 15.
- [38] Hohenberg, P.; Kohn, W. Inhomogeneous Electron Gas. *Physical Review B* **1964**, 136 (3b), B864.
- [39] Blöchl, P. E. Projector augmented-wave method. *Physical Review B* **1994**, 50 (24), 17953.
- [40] Kresse, G.; Joubert, D. From ultrasoft pseudopotentials to the projector augmented-wave method. *Physical Review B* **1999**, 59 (3), 1758.
- [41] Sun, J.; Ruzsinszky, A.; Perdew, J. P. Strongly Constrained and Appropriately Normed Semilocal Density Functional. *Physical Review Letters* **2015**, 115 (3), 036402.

Acknowledgement

R.R. is grateful for a JSPS fellowship from August to October 2019 (Fellowship ID : S19003). R.I. and Y.I. acknowledge the support from JSPS KAKENHI (Grant No. 17H01316, 17K18974, 19H05788, JP17H06094) and “Nanotechnology Platform” (Project No. 12024046) by MEXT, Japan. Financial support was also provided by the Federal Ministry of Education and Research, Germany (BMBF, grant no.: 05K16WC2 & 05K13WC2). Parts of this research were carried out at the large volume press (LVP) beamline P61B and high-energy powder diffraction beamline P02.1 at PETRAIII DESY Hamburg, a member of the Helmholtz Association (HGF). Authors also thank Satish Kulkarni from DESY NanoLab for SEM assistance. Samuel Bernard acknowledges the support from the French funding agency Agence Nationale de la Recherche (ANR) (Project number ANR-16-CE08-0026).

Author contributions

Abhijeet Lale and Samuel Bernard synthesized the single-source precursor and characterized the composition and molecular structure. Shrikant Bhat designed and performed the high-pressure experiments. Robert Farla supported and helped the high-pressure study. Ryo Ishikawa and Wei Zhang investigated the high-pressure samples by electron microscopic methods. Shariq Haseen and Peter Kroll worked on the computational part and Leonore Wiehl on the crystal structure analysis via Rietveld refinement. Ralf Riedel, Yuichi Ikuhara and Tomoo Katsura conceived the project and wrote the paper with input from the other authors.

Competing interests

The authors declare no competing interests.

Summary

A ternary spinel-type $(\text{Si}_{1-x}, \text{Ti}_x)_3\text{N}_4$ compound with spinel-structure type is fortuitously discovered during high-pressure experiments as nanocrystals embedded in spinel- Si_3N_4 in a mixture of c-TiN and spinel- Si_3N_4 . In spinel-type $(\text{Si}_{1-x}, \text{Ti}_x)_3\text{N}_4$, Ti atoms are substituted at different Si sites found in spinel- Si_3N_4 . We perform combinatorial analysis with DFT[1] and find that Ti slightly prefers substitution of octahedral sites over tetrahedral sites in spinel-type $(\text{Si}_{1-x}, \text{Ti}_x)_3\text{N}_4$, though only with a small energy gain of -0.01 eV/56 atoms. In the lowest enthalpy structures of spinel-type $(\text{Si}_{1-x}, \text{Ti}_x)_3\text{N}_4$ that we found, Ti occupied all octahedral sites and exhibited clustering behavior. Next, we computed the enthalpy of formation of the lowest enthalpy ternary compound from its binary phases. We found that the decomposition of spinel-type $(\text{Si}_{1-x}, \text{Ti}_x)_3\text{N}_4$ into its binary phases is thermodynamically favored even if entropy of mixing is taken into account. However, because the precursor that led to the synthesis of spinel-type $(\text{Si}_{1-x}, \text{Ti}_x)_3\text{N}_4$ contained tetrahedral Ti, which are highly disfavored in spinel-type $(\text{Si}_{1-x}, \text{Ti}_x)_3\text{N}_4$ the formation of spinel-type $(\text{Si}_{1-x}, \text{Ti}_x)_3\text{N}_4$ likely occurred due to sluggish kinetics. Bader charge analysis[2] indicated that both Ti^{3+} and Ti^{4+} were present in structures of spinel-type $(\text{Si}_{1-x}, \text{Ti}_x)_3\text{N}_4$ corroborating experimental results. Although, assigning the oxidation state of Ti atoms with Bader charge analysis alone was not possible. Additionally, we found that spinel-type $(\text{Si}_{1-x}, \text{Ti}_x)_3\text{N}_4$ has lower bulk modulus, shear modulus, hardness than spinel- Si_3N_4 as well as having a smaller band gap.

References

- [1] P. Hohenberg, W. Kohn, Inhomogeneous Electron Gas, Physical Review 136(3B) (1964) B864-B871.
- [2] R.F.W. Bader, Atoms in Molecules: A Quantum Theory, Clarendon Press, Oxford, UK, 1990.

CHAPTER 4: WORK OF ADHESION IN GRAPHENE-SiO₂ AND GRAPHENE-SiC

Motivation and Scope

Graphene is a 2D material that has been intensely studied since Novoselov et al.[1, 2] first synthesized free graphene. Investigations suggest that the properties of graphene change if it is bonded to a substrate, and its properties also depend on the identity of the substrate[3, 4]. We study the work of adhesion in potential lithium-ion anode systems consisting of graphene and a second component, either a bilayer-SiO₂ or a (001) SiC surface terminated with oxygen. Additionally, we perform Bader charge analysis[5] to determine the impact of charge transfer on the work of adhesion of each system we study.

Reference

- [1] K.S. Novoselov, A.K. Geim, S.V. Morozov, D. Jiang, Y. Zhang, S.V. Dubonos, I.V. Grigorieva, A.A. Firsov, Electric Field Effect in Atomically Thin Carbon Films, 306(5696) (2004) 666-669.
- [2] K.S. Novoselov, D. Jiang, F. Schedin, T.J. Booth, V.V. Khotkevich, S.V. Morozov, A.K. Geim, Two-dimensional atomic crystals, 102(30) (2005) 10451-10453.
- [3] J. Torres, Y. Zhu, P. Liu, S.C. Lim, M. Yun, Adhesion Energies of 2D Graphene and MoS₂ to Silicon and Metal Substrates, 215(1) (2018) 1700512.
- [4] S. Das, D. Lahiri, D.-Y. Lee, A. Agarwal, W. Choi, Measurements of the adhesion energy of graphene to metallic substrates, Carbon 59 (2013) 121-129.
- [5] R.F.W. Bader, Atoms in Molecules: A Quantum Theory, Clarendon Press, Oxford, UK, 1990.

Work of adhesion in graphene-SiO₂ and graphene-SiCO

Introduction

Graphene has been the focus of numerous investigations since it was first synthesized[1, 2]. The two-dimensional (2D) nature of graphene makes it a promising candidate for complementary metal-oxide-semiconductor (CMOS) design[3]. Additionally, graphene exhibits carrier mobility greater than 200,000 cm²/Vs[4] and reversible capacity between 540 – 835 mAh/g as an anode in lithium-ion batteries[5, 6]. As an anode, graphene has been combined with silicon, which by itself has a theoretical reversible capacity of 4200 mAh/g but undergoes volume expansion up to 400% during cycling[7] resulting in disintegration of the anode. Silicon-graphene composites have been synthesized and exhibited high capacity retention [8] and storage capacity up to 2200 mAh/g[9].

There have been several investigations of the work of adhesion between graphene and various systems[10, 11]. Additionally, substantial work has been done on the work of adhesion between SiO₂ and graphene. In 2011, Koenig et al.[12] measured the work of adhesion between monolayer graphene and a SiO₂-substrate using a pressurized blister test and reported a value of 0.45 ± 0.02 J/m². In 2013, Boddeti et al.[13] reported a work of adhesion value of 0.24 J/m² between graphene and SiO₂ by also performing pressurized blister tests. Meanwhile, Gao et al.[14] calculated 0.349 J/m² for work of adhesion associated with graphene and reconstructed silicon dioxide surfaces.

Considering the recent synthesis of a 2D bilayer of SiO₂ on graphene[15], we investigate potential anode materials consisting of a graphene-SiO₂-bilayer system as well as additional graphene-Si₂CO₂ systems. Through first-principles calculations, we calculate the work of adhesion between compound systems of graphene and SiO₂/Si₂CO₂. Using Bader charge analysis[16], we determine the impact of charge transfer on calculated work of adhesion values.

Method

Spin-polarized density functional theory calculations were carried out with the Vienna ab initio Simulation Package (VASP)[17-20]. Exchange-correlation was described by the PBE functional[21, 22], and calculations used the projector-augmented wave method (PAW)[23] with a $E_{\text{kin}} = 500$ eV. Forces were converged to 50 meV/Å. Additionally, since PBE does not correctly describe dispersion interactions, calculations were done with the Tkatchenko-Scheffler method[24] (DFT-TS), the universal low gradient method[25] (DFT-ulg), and Hamada's nonlocal van der Waals density functional[26] (DFT-vdW-DF2-B86R). A k -point set of $2 \times 2 \times 2$ was used for calculations of graphite and a k -point set of $1 \times 1 \times 1$ was used for all other calculations when sampling the Brillouin zone[27]. Work of adhesion was calculated by taking the difference between the energy of an unrelaxed structure with “infinite” interlayer separation distance ($d_{\infty} = 20$ Å) and the energy of an optimized structure with equilibrium interlayer separation distance (d_0) and dividing by the cross-sectional area of the interface A (see Equation 1). Bader charge analysis was performed using the Bader Charge Analysis code[28, 29] developed by the Henkelman Group.

$$\text{Work of adhesion} = \frac{E_{d_{\infty}} - E_{d_0}}{A} \quad (1)$$

Models

We investigated three different compound systems: graphene-bilayer-SiO₂, graphene-15Si₂CO₂, and graphene-16Si₂CO₂. To model the graphene-bilayer-SiO₂ system we combined a supercell of graphene (150 atoms) with a bilayer of SiO₂ (64 SiO₂). The bilayer-SiO₂ model itself was constructed of two layers of [SiO₄]-tetrahedra.

Additionally, we constructed two graphene-Si₂CO₂ models. Two (001) surfaces of SiC were terminated with oxygen and then extended into supercells of $3 \times 5 \times 1$ and $4 \times 4 \times 1$. The

3×5×1 supercell had a composition of 15Si₂CO₂ and was combined with a supercell of graphene (48 atoms) to yield a graphene-15Si₂CO₂. Meanwhile, the 4×4×1 supercell had a composition of 16Si₂CO₂ and was combined with a supercell of graphene (60 atoms) to yield a graphene-16Si₂CO₂ system. Lattice parameters are given in Table 1. For reference, we also performed calculations on graphite with 6 graphene layers with ABABAB-stacking (12 atoms).

Table 1: Lattice parameters a and b for graphene-15Si₂CO₂, graphene-16Si₂CO₂, and graphene-bilayer-SiO₂ optimized with different dispersion correction methods

	graphene-15Si ₂ CO ₂		graphene-16Si ₂ CO ₂		graphene-bilayer-SiO ₂	
	<u>a (Å)</u>	<u>b (Å)</u>	<u>a (Å)</u>	<u>b (Å)</u>	<u>a (Å)</u>	<u>b (Å)</u>
DFT-ulg	8.6499	14.7040	12.1710	12.4442	21.2688	18.4193
DFT-TS	8.6612	14.7266	12.1851	12.4578	21.2736	18.4235
DFT-vdW-DF2 B86R	8.6735	14.7441	12.1989	12.4730	21.2959	18.4427

Results

Work of adhesion

Using different dispersion correction methods, we calculated work of adhesion (see Table 2). Calculations of the work of adhesion for graphite by the various dispersion correction methods generally agree with experiment[30]. Although DFT-DF functionals typically overestimate the equilibrium interlayer separation distance between layers d_0 [31], the DFT-DF2-B86R functional calculates d_0 close to those of the Tkatchenko-Scheffler and universal low gradient dispersion correction methods. Results from all van der Waals correction methods predict the work of adhesion between graphene for both Si₂CO₂ slabs and the bilayer-SiO₂ slab to be lower than the work of adhesion of graphite. Work of

adhesion is higher for the graphene-Si₂CO₂ systems than for the graphene-bilayer-SiO₂ system.

Table 2: Work of adhesion (J/m²) for graphite, graphene-15Si₂CO₂, graphene-16Si₂CO₂, and graphene-bilayer-SiO₂

	graphite	graphene- 15Si ₂ CO ₂	graphene- 16Si ₂ CO ₂	graphene- bilayer-SiO ₂
DFT-ulg	0.41	0.37	0.37	0.27
DFT-TS	0.58	0.46	0.45	0.33
DFT-vdW-DF2-B86R	0.39	0.29	0.29	0.25
Exp.	0.39 ± 0.02[30]	-	-	-

Generally, d_0 of the graphene-Si₂CO₂ systems is smaller than d_0 of graphene-bilayer-SiO₂. For graphene-16Si₂CO₂ there are 16 O atoms on the relevant side of the Si₂CO₂ slab interacting with 60 carbon atoms in the graphene layer leading to a 0.267 O: 1 C ratio (0.11 O atoms/Å² of graphene). Similarly, graphene-15Si₂CO₂ has an oxygen surface density of 0.11 O atoms/Å² of graphene. Meanwhile, for graphene-bilayer-SiO₂ there are 48 O atoms on the relevant side of the bilayer-SiO₂ slab interacting with 150 C atoms in the graphene layer. Thus, there is a surface density of 0.12 O atoms/Å² of graphene. Considering the similar oxygen surface densities of each system, it is unlikely that repulsion between the surface O of each Si₂CO₂/bilayer-SiO₂ surface and graphene is responsible for the difference in d_0 between the graphene-Si₂CO₂ systems and graphene-bilayer-SiO₂.

Table 3: Interlayer equilibrium separation distance (d_0) in Å for graphite, graphene-15Si₂CO₂, graphene-16Si₂CO₂, and graphene-bilayer-SiO₂

	graphite	graphene- 15Si ₂ CO ₂	graphene- 16Si ₂ CO ₂	graphene- bilayer-SiO ₂
DFT-ulg	3.34	3.10	3.08	3.20
DFT-TS	3.32	3.06	3.06	3.18
DFT-vdW-DF2- B86R	3.33	3.09	3.07	3.17
Exp.	3.34[32]	-	-	-

Charge analysis

In order to determine the impact of charge transfer between the two components of the graphene-SiO₂/Si₂CO₂ systems on the work of adhesion, we calculate Bader charges for each component of the compound systems optimized with DFT-ulg (see Table 4). Bader charge analysis indicates charge transfer occurs between the two components of a compound model. Generally, the bilayer-SiO₂/Si₂CO₂ component of each compound model accumulates charge while the graphene component is depleted of charge. The magnitude of the largest charge transfer is between 0.0033 e⁻/Å² which is smaller than even the charge transfer between small organic molecules on an MoS₂ monolayer (0.005 – 0.025 e⁻/Å²)[33].

Table 4: Changes in Bader charges (e^-) ($q_{\text{compound}} - q_{\text{isolated-component}}$) for each component of the compound graphene-SiO₂/Si₂CO₂ systems optimized within DFT-ulg. Positive values indicate charge accumulation in the compound model and negative values indicate charge depletion

	bilayer-SiO ₂ /Si ₂ CO ₂	graphene
graphene-bilayer-SiO ₂	+0.00317	-0.00317
graphene-15Si ₂ CO ₂	+0.00330	-0.00330
graphene-16Si ₂ CO ₂	+0.00251	-0.00251

Summary

We calculated the work of adhesion energies of interfaces formed between graphene and a bilayer-SiO₂ and graphene and Si₂CO₂. In order to correct for the poor description of dispersion interactions in standard PBE we performed calculations with several different van der Waals correction methods and functionals. Results produced by all dispersion correction methods generally agreed well with experiment for graphite. Although there is a large range of reported values for the work of adhesion between SiO₂ and graphene, our calculated work of adhesion value for graphene-bilayer-SiO₂ falls within that range.[12-14]

Work of adhesion values in the graphene-Si₂CO₂ systems were significantly larger than work of adhesion in the graphene-bilayer-SiO₂ system. In order to determine why work of adhesion values differed between the graphene-Si₂CO₂ systems and the graphene-bilayer-SiO₂ system we investigated the role charge transfer within the compound systems. While Bader charge analysis did indicate that there was charge transfer taking place from graphene to the Si₂CO₂/bilayer-SiO₂ surface in each system, the magnitude of the charge transfer is likely too small to explain the differences in the

work of adhesion between the graphene-Si₂CO₂ systems and the graphene-bilayer-SiO₂ system.

References

- [1] K.S. Novoselov, A.K. Geim, S.V. Morozov, D. Jiang, Y. Zhang, S.V. Dubonos, I.V. Grigorieva, A.A. Firsov, Electric Field Effect in Atomically Thin Carbon Films, 306(5696) (2004) 666-669.
- [2] K.S. Novoselov, D. Jiang, F. Schedin, T.J. Booth, V.V. Khotkevich, S.V. Morozov, A.K. Geim, Two-dimensional atomic crystals, 102(30) (2005) 10451-10453.
- [3] A.C. Ferrari, F. Bonaccorso, V. Fal'ko, K.S. Novoselov, S. Roche, P. Bøggild, S. Borini, F.H.L. Koppens, V. Palermo, N. Pugno, J.A. Garrido, R. Sordan, A. Bianco, L. Ballerini, M. Prato, E. Lidorikis, J. Kivioja, C. Marinelli, T. Ryhänen, A. Morpurgo, J.N. Coleman, V. Nicolosi, L. Colombo, A. Fert, M. Garcia-Hernandez, A. Bachtold, G.F. Schneider, F. Guinea, C. Dekker, M. Barbone, Z. Sun, C. Galiotis, A.N. Grigorenko, G. Konstantatos, A. Kis, M. Katsnelson, L. Vandersypen, A. Loiseau, V. Morandi, D. Neumaier, E. Treossi, V. Pellegrini, M. Polini, A. Tredicucci, G.M. Williams, B. Hee Hong, J.-H. Ahn, J. Min Kim, H. Zirath, B.J. van Wees, H. van der Zant, L. Occhipinti, A. Di Matteo, I.A. Kinloch, T. Seyller, E. Quesnel, X. Feng, K. Teo, N. Rupesinghe, P. Hakonen, S.R.T. Neil, Q. Tannock, T. Löfwander, J. Kinaret, Science and technology roadmap for graphene, related two-dimensional crystals, and hybrid systems, Nanoscale 7(11) (2015) 4598-4810.
- [4] S.V. Morozov, K.S. Novoselov, M.I. Katsnelson, F. Schedin, D.C. Elias, J.A. Jaszczak, A.K. Geim, Giant Intrinsic Carrier Mobilities in Graphene and Its Bilayer, Physical Review Letters 100(1) (2008) 016602.
- [5] E. Yoo, J. Kim, E. Hosono, H.-s. Zhou, T. Kudo, I. Honma, Large Reversible Li Storage of Graphene Nanosheet Families for Use in Rechargeable Lithium Ion Batteries, Nano Letters 8(8) (2008) 2277-2282.
- [6] H.F. Xiang, Z.D. Li, K. Xie, J.Z. Jiang, J.J. Chen, P.C. Lian, J.S. Wu, Y. Yu, H.H. Wang, Graphene sheets as anode materials for Li-ion batteries: preparation, structure, electrochemical properties and mechanism for lithium storage, RSC Advances 2(17) (2012) 6792-6799.
- [7] B. Jerliu, E. Hüger, L. Dörrer, B.K. Seidlhofer, R. Steitz, V. Oberst, U. Geckle, M. Bruns, H. Schmidt, Volume Expansion during Lithiation of Amorphous Silicon Thin Film Electrodes Studied by In-Operando Neutron Reflectometry, The Journal of Physical Chemistry C 118(18) (2014) 9395-9399.
- [8] J.-G. Ren, Q.-H. Wu, G. Hong, W.-J. Zhang, H. Wu, K. Amine, J. Yang, S.-T. Lee Silicon–Graphene Composite Anodes for High-Energy Lithium Batteries, 1(1) (2013) 77-84.
- [9] J.K. Lee, K.B. Smith, C.M. Hayner, H.H. Kung, Silicon nanoparticles–graphene paper composites for Li ion battery anodes, Chemical Communications 46(12) (2010) 2025-2027.

- [10] S. Das, D. Lahiri, D.-Y. Lee, A. Agarwal, W. Choi, Measurements of the adhesion energy of graphene to metallic substrates, *Carbon* 59 (2013) 121-129.
- [11] J. Torres, Y. Zhu, P. Liu, S.C. Lim, M. Yun, Adhesion Energies of 2D Graphene and MoS₂ to Silicon and Metal Substrates, 215(1) (2018) 1700512.
- [12] S.P. Koenig, N.G. Boddeti, M.L. Dunn, J.S. Bunch, Ultrastrong adhesion of graphene membranes, *Nature Nanotechnology* 6(9) (2011) 543-546.
- [13] N.G. Boddeti, S.P. Koenig, R. Long, J. Xiao, J.S. Bunch, M.L. Dunn, Mechanics of Adhered, Pressurized Graphene Blisters, *Journal of Applied Mechanics* 80(4) (2013).
- [14] W. Gao, P. Xiao, G. Henkelman, K.M. Liechti, R. Huang, Interfacial adhesion between graphene and silicon dioxide by density functional theory with van der Waals corrections, *Journal of Physics D: Applied Physics* 47(25) (2014) 255301.
- [15] P.Y. Huang, S. Kurasch, A. Srivastava, V. Skakalova, J. Kotakoski, A.V. Krashenninnikov, R. Hovden, Q. Mao, J.C. Meyer, J. Smet, D.A. Muller, U. Kaiser, Direct Imaging of a Two-Dimensional Silica Glass on Graphene, *Nano Letters* 12(2) (2012) 1081-1086.
- [16] R.F.W. Bader, *Atoms in Molecules: A Quantum Theory*, Clarendon Press, Oxford, UK, 1990.
- [17] G. Kresse, J. Hafner, Ab initio molecular dynamics for liquid metals, *Physical Review B* 47(1) (1993) 558-561.
- [18] G. Kresse, J. Hafner, Ab initio molecular-dynamics simulation of the liquid-metal-amorphous-semiconductor transition in germanium, *Physical Review B* 49(20) (1994) 14251-14269.
- [19] G. Kresse, J. Furthmüller, Efficiency of ab-initio total energy calculations for metals and semiconductors using a plane-wave basis set, *Computational Materials Science* 6(1) (1996) 15-50.
- [20] G. Kresse, J. Furthmüller, Efficient iterative schemes for ab initio total-energy calculations using a plane-wave basis set, *Physical Review B* 54(16) (1996) 11169-11186.
- [21] J.P. Perdew, K. Burke, M. Ernzerhof, Generalized Gradient Approximation Made Simple, *Physical Review Letters* 77(18) (1996) 3865-3868.
- [22] J.P. Perdew, K. Burke, M. Ernzerhof, Generalized Gradient Approximation Made Simple [Phys. Rev. Lett. 77, 3865 (1996)], *Physical Review Letters* 78(7) (1997) 1396-1396.
- [23] P.E. Blöchl, Projector augmented-wave method, *Physical Review B* 50(24) (1994) 17953-17979.
- [24] A. Tkatchenko, M. Scheffler, Accurate Molecular Van Der Waals Interactions from Ground-State Electron Density and Free-Atom Reference Data, *Physical Review Letters* 102(7) (2009) 073005.
- [25] H. Kim, J.-M. Choi, W.A. Goddard, Universal Correction of Density Functional Theory to Include London Dispersion (up to Lr, Element 103), *The Journal of Physical Chemistry Letters* 3(3) (2012) 360-363.
- [26] I. Hamada, van der Waals density functional made accurate, *Physical Review B* 89(12) (2014) 121103.
- [27] H.J. Monkhorst, J.D. Pack, Special points for Brillouin-zone integrations, *Physical Review B* 13(12) (1976) 5188-5192.

- [28] G. Henkelman, A. Arnaldsson, H. Jónsson, A fast and robust algorithm for Bader decomposition of charge density, *Computational Materials Science* 36(3) (2006) 354-360.
- [29] W. Tang, E. Sanville, G. Henkelman, A grid-based Bader analysis algorithm without lattice bias, *Journal of Physics: Condensed Matter* 21(8) (2009) 084204.
- [30] W. Wang, S. Dai, X. Li, J. Yang, D.J. Srolovitz, Q. Zheng, Measurement of the cleavage energy of graphite, *Nature communications* 6 (2015) 7853-7853.
- [31] S. Lebègue, J. Harl, T. Gould, J.G. Ángyán, G. Kresse, J.F. Dobson, Cohesive Properties and Asymptotics of the Dispersion Interaction in Graphite by the Random Phase Approximation, *Physical Review Letters* 105(19) (2010) 196401.
- [32] G. Çakmak, T. Öztürk, Continuous synthesis of graphite with tunable interlayer distance, *Diamond and Related Materials* 96 (2019) 134-139.
- [33] Y. Jing, X. Tan, Z. Zhou, P. Shen, Tuning electronic and optical properties of MoS₂ monolayer via molecular charge transfer, *Journal of Materials Chemistry A* 2(40) (2014) 16892-16897.

Summary

We investigated the work of adhesion associated with interfaces formed between systems of graphene and a bilayer-SiO₂, which has been recently synthesized[1], graphene and 15Si₂CO₂, and graphene and 16Si₂CO₂. Calculations were done with several different van der Waals correction methods and functionals to account for dispersion interactions. Results produced by all dispersion correction methods agreed well with experiment for our reference structure of graphite. Additionally, our calculated work of adhesion value for graphene-bilayer-SiO₂ agreed with experiment[2] We found that work of adhesion in graphene-Si₂CO₂ was larger than work of adhesion in graphene-bilayer-SiO₂. Consequently, we investigated the impact of charge transfer on the work of adhesion for our compound systems. Bader charge analysis[3] did indicate that there was charge depletion of graphene and charge increase on the Si₂CO₂/bilayer-SiO₂ surface in each system, but the magnitude of charge transfer was smaller than the charge transfer associated with the adsorption of small molecules on a surface.[4]

References

- [1] P.Y. Huang, S. Kurasch, A. Srivastava, V. Skakalova, J. Kotakoski, A.V. Krashenninnikov, R. Hovden, Q. Mao, J.C. Meyer, J. Smet, D.A. Muller, U. Kaiser, Direct Imaging of a Two-Dimensional Silica Glass on Graphene, *Nano Letters* 12(2) (2012) 1081-1086.
- [2] N.G. Boddeti, S.P. Koenig, R. Long, J. Xiao, J.S. Bunch, M.L. Dunn, Mechanics of Adhered, Pressurized Graphene Blisters, *Journal of Applied Mechanics* 80(4) (2013).
- [3] R.F.W. Bader, *Atoms in Molecules: A Quantum Theory*, Clarendon Press, Oxford, UK, 1990.
- [4] Y. Jing, X. Tan, Z. Zhou, P. Shen, Tuning electronic and optical properties of MoS₂ monolayer via molecular charge transfer, *Journal of Materials Chemistry A* 2(40) (2014) 16892-16897.

PART II: CALCULATION AND SIMULATION OF AMORPHOUS CERAMICS

CHAPTER 1: ANALYZING THE EFFECT OF COMPOSITION, DENSITY, AND THE MORPHOLOGY OF THE “FREE” CARBON PHASE ON ELASTIC MODULI IN SILICON OXYCARBIDE CERAMICS

Motivation and Scope

Several studies have been done on the mechanical properties of SiCO polymer-derived ceramics[1, 2]. Sorarù et al.[3] reported that Young's modulus of SiCO with free carbon increases with increasing free carbon content but decreases with decreasing density. However, synthesis of the samples conflated free carbon content and density. Through molecular dynamics simulations, we compute elastic properties of SiCO with varying compositions of the glass, free carbon content, density, and free carbon structure. By independently varying free carbon content and density, we calculate how each quantity impacts elastic properties. Additionally, by varying the free carbon morphology while keeping composition and density constant, we assess the impact of free carbon morphology on elastic properties.

References

- [1] T. Rouxel, G. Massouras, G.-D. Sorarù, High Temperature Behavior of a Gel-Derived SiOC Glass: Elasticity and Viscosity, *Journal of Sol-Gel Science and Technology* 14(1) (1999) 87-94.
- [2] S. Walter, G.D. Soraru, H. Bréquel, S. Enzo, Microstructural and mechanical characterization of sol gel-derived Si–O–C glasses, *Journal of the European Ceramic Society* 22(13) (2002) 2389-2400.
- [3] G.D. Sorarù, L. Kundanati, B. Santhosh, N. Pugno, Influence of free carbon on the Young's modulus and hardness of polymer-derived silicon oxycarbide glasses, *Journal of the American Ceramic Society* 102(3) (2019) 907-913.

Analyzing the Effect of Composition, Density, and the Morphology of the “free” Carbon Phase on Elastic Moduli in Silicon Oxycarbide Ceramics

Shariq Haseen and Peter Kroll*

Department of Chemistry and Biochemistry, The University of Texas at Arlington
700 Planetarium Place, Arlington, Texas 76019, United States.

*pkroll@uta.edu

Abstract

We perform atomistic simulations to model structures and calculate elastic properties of silicon oxycarbide ceramics. We explore individual parameters – composition, density, carbon content – to disentangle mutual dependencies that are difficult to separate in experimental studies. Each parameter is studied through dynamic simulations at finite temperatures for a wide range of temperatures. With multi-million atom models in simulation boxes as large as 40 nm, we reveal a hitherto “hidden” parameter: the morphology of the “free” carbon phase. Embedding, distribution, and interconnection of the carbon phase inside the amorphous matrix of SiCO severely impact the material's mechanical properties. As a consequence, we call for the development of new characterization techniques that will quantify the morphology of carbon in this and similar systems.

Keywords

silicon oxycarbide, free carbon morphology, elastic properties, molecular dynamics

Introduction

Silicon oxycarbide (SiCO) ceramics have attracted much interest over the last decades[1]. They exhibit remarkable structural stability and chemical durability[2, 3], oxidation resistance[4, 5], and unusual creep resistance[6-8]. There are a variety of potential applications for SiCO ceramics, including usage as anode material in Li-ion batteries[9, 10], as heating elements for pencil-type glow plugs[11], and as coatings[12]. The properties and structural characteristics of SiCO ceramics depend on the precursor materials and processing conditions, particularly on the maximum temperature reached during the pyrolysis step of the precursor-to-ceramic conversion process. Pyrolysis temperatures must reach around 1273 K to yield a single-phase amorphous SiC_xO_y [13]. Meanwhile, pyrolysis between 1273 K and 1723 K results in phase separation of the amorphous SiCO ceramic into crystalline SiC and amorphous SiO_2 [14, 15]. Furthermore, if the composition of the amorphous SiCO displays excess carbon besides SiC and SiO_2 , then a “free” carbon phase C_{free} , with carbon bonding (almost) exclusively to carbon, forms. The resulting composition is $\text{SiC}_x\text{O}_y = (y/2)\text{SiO}_2 + (1 - y/2)\text{SiC} + (x + y/2 - 1)\text{C}_{\text{free}}$. Exceeding a pyrolysis temperature of 1723 K usually results in amorphous SiO_2 and SiC nanocrystals encased by turbostratic carbon[14].

Multiple studies addressed the origin and structural evolution of the excess carbon phase[16, 17] A detailed summary of current understanding is presented in a recent review[18]. For pyrolysis temperatures lower than 1073 K, excess carbon has only begun to segregate and is amorphous, hydrogenated, and still dispersed in the ceramic matrix[19]. Increasing pyrolysis temperatures to 1073 K – 1273K results in a “free” carbon phase described as 2-3 layers thick turbostratic carbon saturated with hydrogen at the periphery[20]. Pyrolysis temperatures higher than 1273 K – 1473 K eliminate hydrogen from peripheral carbons and yield extended carbon layers. Above pyrolysis

temperatures of 1673 K, the excess carbon phase forms graphite nanocrystallites or an entangled network of single- or multi-layered graphene[18].

The mechanical properties of SiCO have been studied at ambient and elevated temperatures. Rouxel et al. were among the first to explore the high-temperature behavior of SiCO glasses[21]. They proposed that the Young's modulus of SiCO can be calculated using a simple rule of mixture using volume fractions of constituent phases. Since graphite has lower elastic moduli than SiC and SiO₂, it is generally inferred that SiCO with high free carbon content displays low moduli when compared to SiCO with low free carbon content – provided that the ratio SiC to SiO₂ is comparable. This trend appears to be supported by a recent study by Sorarù et al., who synthesized SiCO glasses with varying amounts of free carbon and provided a thorough comparative study of Young's modulus and hardness[22]. The impact of the pyrolysis temperature on mechanical properties is also of interest for ceramic matrix composites (CMCs) that use a SiCO matrix and/or SiCO fibers embedded into a ceramic matrix[23, 24].

In contrast to many experimental studies, only a few computational investigations relate to SiCO. Early on, we used density functional theory (DFT) and ab initio molecular dynamics to investigate structure and elastic moduli of amorphous SiCO[25]. Subsequent work addressed interfacial bonding between glassy SiCO and the free carbon phase[26]. Further atomistic simulations with empirical potentials investigated some temperature-dependency of mechanical properties[27, 28].

In this study, we focus on the elastic properties of amorphous SiCO, including different amounts of “free” carbon, C_{free} . We perform atomistic simulations using an empirical potential to investigate how elastic moduli depend on various parameters, namely composition of the amorphous SiCO glass matrix, density, C_{free} content, and the particular morphology the C_{free} attains. We also study the temperature dependency of moduli. Significant computer resources facilitate us to examine each parameter individually, enabling us to disentangle dependencies that are difficult to separate in

experimental studies. Anticipating our results, we show that – for the same composition and density – the impact of carbon morphology on mechanical properties is considerable.

Method

In previous work, we generated SiCO models using an approach based on the Wooten, Winer, and Waire (WWW) algorithm and optimized these models within density functional theory (DFT)[25, 26]. While DFT calculations are highly accurate, they are also computationally expensive, thus limiting the size of models and the extent of simulations. Calculations using the Tersoff potential, an empirical bond-order potential, are much faster than DFT calculations, and models can routinely be as large as millions of atoms. Simulations can extend for microseconds if needed. Models generated with the Tersoff potential, on the other side, display structural imperfections. Nevertheless, the Tersoff potential reproduces mechanical properties adequately[27, 28], even though the specific parametrization of the potential in some cases does impact the magnitude of trends[29].

Throughout this work, we perform molecular dynamics simulations implemented in the Large-scale Atomic/Molecular Massively Parallel Simulator (LAMMPS)[30]. Interactions are described via the Tersoff potential[31, 32]. Si–Si, Si–C, and C–C interactions are parameterized by Tersoff[31–33]. Si–O interactions are parameterized by Munetoh et al.[34]. Similar to previous studies, we treat interactions between O atoms or between C and O as repulsive only, based on spectroscopic evidence[2]. We generate SiCO models through a melt-quench process: randomly positioned Si, C, and O atoms are heated from 0 K to temperature T_{max} at a rate of 10 K/ps. For the critical parameter T_{max} , we choose temperatures between 2000 and 8000 K. At T_{max} , the system is equilibrated for 200 ps and then cooled to 300 K at a rate of 10 K/ps. All simulations are done at constant volume to fix density. We performed additional simulations using different equilibration times and cooling rates. Overall, we find that carbon morphology in models is almost

completely determined through T_{\max} . Longer equilibration times, we tested up to 100 ns at T_{\max} , have some impact. However, changes that occur when increasing T_{\max} by just 50 K are similar to an extension of equilibration time by a factor of 20 to 100. A slower cooling rate, e.g. 1 K/ps, does not change the morphology of carbon segregations but reduces the fraction of local defects in the final structure. Most importantly, it has a negligible impact on mechanical properties. Throughout our simulations, we use a time step of 1 fs to integrate the equations of motion.

In this study, we explore the impact of compositions and densities on the mechanical properties of SiCO. Addressing the composition of the stoichiometric SiCO glass matrix, we model three different compositions: SiO_2 , Si_5CO_8 ($=\text{SiC}_{0.2}\text{O}_{0.8}$), and Si_2CO_2 ($=\text{SiC}_{0.5}\text{O}$). This reflects 0, 20, and 50 mol-% SiC content, respectively. For each glass composition, we then build models with four different free carbon contents by adding as many C atoms as to achieve a ratio of $C_{\text{free}}:\text{Si}$ of 0.5, 1, 2, and 3. Thus, Si_5CO_8 with C_{free} corresponding to a ratio $C_{\text{free}}:\text{Si} = 2$ has the composition $\text{Si}_5\text{CO}_8:10 \cdot C_{\text{free}} = \text{Si}_5\text{C}_{11}\text{O}_8$. Overall, this yields $3 \cdot 4 = 12$ different compositions that we explore. Structures for each composition are then generated at five different densities ($1.4\text{--}2.2 \text{ g/cm}^3$). Furthermore, we generate models of each system for five different T_{\max} , 2000, 3000, 4000, 6000, and 8000K, to examine various free carbon morphologies. Finally, we generate three independent models by choosing different initial random numbers for each set of model parameters (glass composition, C_{free} content, density, T_{\max}). In total, this yields $(3 \cdot 4) \cdot 5 \cdot 5 \cdot 3 = 900$ models.

When developing models for this study, we realized that the simulation box size can constrain the morphology of the free carbon phase. This is particularly important for models with high carbon content and for models that display segregation. Modeling structural features of a particular dimension requires a simulation at a significantly larger length scale. For our study, models with a simulation box size between 7 and 10 nm are necessary to develop extended nano-sized carbon networks. Consequently, the models we

generate contain between 24,000 and 50,000 atoms in cubic boxes with side lengths between 7 and 10 nm. Figure 1 shows two models of $\text{Si}_2\text{CO}_2 + \text{C}_{\text{free}}$ (24,576 atoms) with different densities. For each model, we display once all atoms (Figure 1 **a, b**) and then the C atoms only (Figure 1 **c, d**). Subsequent models' figures will display the C atoms only to highlight characteristics of carbon morphology. For consistency checks and to explore the impact of periodic boundary conditions, we modeled one composition, $\text{Si}_5\text{CO}_8 + 10\text{C}_{\text{free}}$, with a density of 2.2 g/cm^3 in 8-fold and 64-fold sizes following the same simulation protocol as described above. The largest model, thus, comprises 2.52 million atoms and has a box length of $\sim 40 \text{ nm}$. We find through this scaling analysis that, albeit some subtle differences emerge and will be discussed, our choice of models is sufficient for exploring mechanical properties.

After model generation, we compute the elastic constants c_{ij} of each model through dynamic simulations at temperatures from 100 to 2000 K[35]. Temperatures for dynamic simulations of moduli are not to be confused with T_{max} , the temperature used for generating a particular model. For each model, 13 short simulations are performed: one for the initial state, six positive deformations, and six negative deformations. The first simulation is done to determine the initial state of the structure without deformation by equilibrating at a target temperature. During the other 12 simulations, models are deformed by 0.5% in a selected direction and equilibrated at the target temperature for 1.0 ps. Subsequently, the stress tensor is sampled 10 times every 0.1 ps within a 0.3 ps interval, and elastic constants are computed from the pressure tensor. The results of positive and negative deformations are averaged for each elastic constant. Application of the Voigt-Reuss-Hill approximation[36-38] to the calculated elastic constants yields values for bulk modulus, B_0 , shear modulus, G , and Young's modulus, E . Using this method, we calculate the bulk modulus of cubic SiC to be 225 GPa at 300 K, which agrees with the value reported by Tersoff (220 GPa)[32].

Results and Discussion

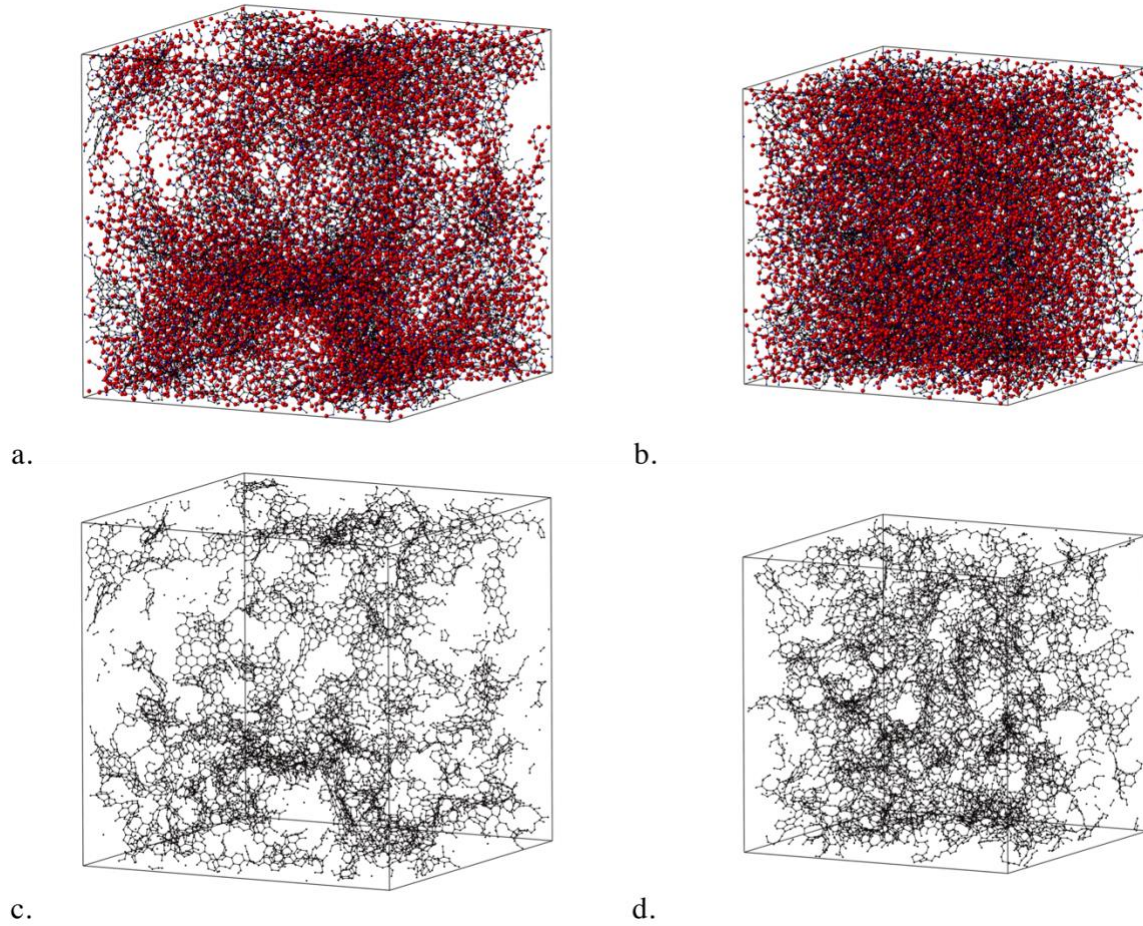


Figure 1: Models of $\text{Si}_2\text{CO}_2 + \text{C}_{\text{free}}$ (24,576 atoms) generated at $T_{\text{max}} = 4000 \text{ K}$ with a. density $\rho = 1.4 \text{ g/cm}^3$ and b. $\rho = 2.2 \text{ g/cm}^3$. Models from a. and b. shown without Si and O atoms and only C atoms with c. $\rho = 1.4 \text{ g/cm}^3$ and d. $\rho = 2.2 \text{ g/cm}^3$. C content $\text{C}_{\text{free}}:\text{Si} = 0.5$, density ρ , $T_{\text{max}} = 4000 \text{ K}$. Si atoms are blue, O atoms are red, and C atoms are black.

Impact of density

We start our investigation of the elastic properties of SiCO by comparing models with identical chemical compositions but different densities. Hence, in a system with the same glass composition and content $\text{C}_{\text{free}}:\text{Si}$, we only vary the volume of the simulation box. Furthermore, we compare only data for models generated using the same T_{max} . Comparison is also made only for data attained using the same simulation temperature

during dynamic simulations of moduli. Results are shown in Figure 2 for three selected compositions. In general, we find that the elastic response of SiO_2 and SiCO is aligned with predictions of elastic medium theory: more dense models exhibit higher elastic moduli[39]. Similar trends were computed previously for stoichiometric SiCO glass using DFT calculations[25]. In fact, Colombo et al. observed that Young's modulus increased with increasing density for SiCO ceramic foams[40]. Without quantifying dependencies in greater detail, we find that the slope of the relation moduli versus density depends on the composition of the glass phase, T_{max} used for model construction, and the temperature used for the dynamic simulation of elastic moduli.

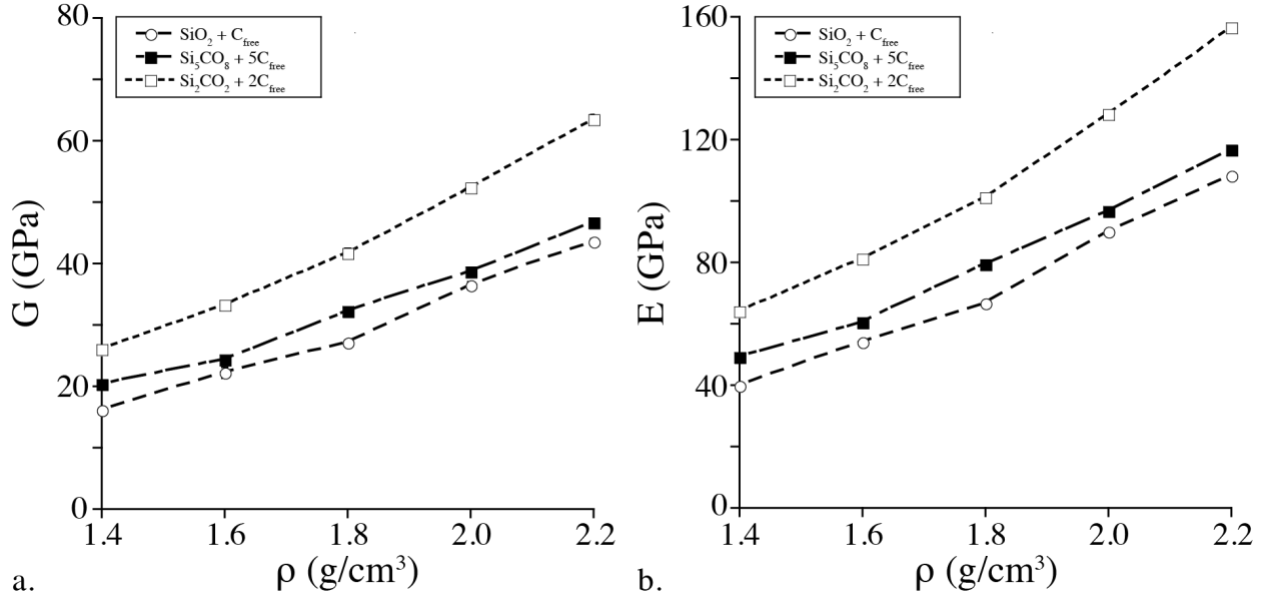


Figure 2: (Left) Shear modulus and (right) Young's modulus vs. density ρ for models with content $\text{C}_{\text{free}}:\text{Si} = 1$ and composition $\text{Si}_5\text{CO}_8 + 5\text{C}_{\text{free}}$, $\text{SiO}_2 + \text{C}_{\text{free}}$, and $\text{Si}_2\text{CO}_2 + 2\text{C}_{\text{free}}$ generated at $T_{\text{max}} = 3000$ K. Elastic constants are calculated in triplicate for each of 3 independently generated models. Error bars (if larger than the symbol used) represent standard error. Simulations are done at 300 K. Lines are provided to guide the eye.

Impact of glass composition

We next assess the impact of the composition of the glass matrix in SiCO on its elastic properties. Thus, for models comprising the same free carbon content $C_{\text{free}}:\text{Si}$ and density ρ , and generated using the same T_{max} , we analyze the dependency of elastic moduli on the composition of the glass matrix. In Figure 3, we show the temperature dependency of moduli (between 100 K and 2000 K) for models with a free carbon content $C_{\text{free}}:\text{Si} = 0.5$. Before discussing the trend, we note that the error margin increases significantly at higher temperatures. This error margin is considerably reduced in large models, as shown below.

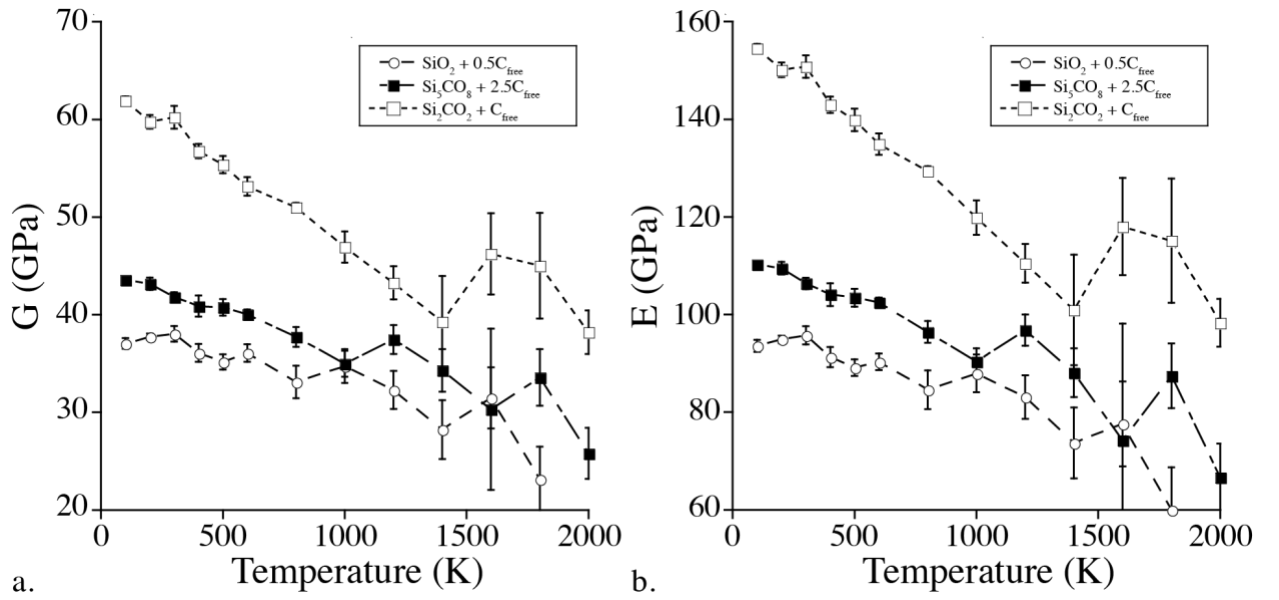


Figure 3: (a) Shear modulus and (b) Young's modulus for models with C content $C_{\text{free}}:\text{Si} = 0.5$, density $\rho = 2.2 \text{ g/cm}^3$, and composition $\text{SiO}_2 + 0.5C_{\text{free}}$, $\text{Si}_5\text{CO}_8 + 2.5C_{\text{free}}$, and $\text{Si}_2\text{CO}_2 + C_{\text{free}}$ generated using $T_{\text{max}} = 4000 \text{ K}$. Elastic constants are calculated in triplicate for each of 3 independently generated models. Error bars represent standard error. Lines are provided to guide the eye.

We observe that the higher the SiC content in the glass, the higher the elastic moduli. This trend is found for all combinations of C content, density, and T_{max} , albeit to a different extent in each case. The result is hardly surprising, given that both amorphous and crystalline SiC[41, 42] have higher elastic moduli than most amorphous and crystalline forms of SiO_2 [43, 44]. The glass matrix of SiCO can be regarded as a solid

solution of both components. For models of glassy SiCO without free carbon, this trend was previously reported based on DFT calculations, albeit for much smaller models[25].

Experimentally, SiCO samples with very low amounts of excess carbon ($\text{SiC}_{0.31}\text{O}_{1.39} + 0.07\text{C}$) have been synthesized and measured to have Young's modulus between 90 – 100 GPa[45]. The Young's moduli of SiCO samples with higher amounts of free carbon (12 – 54 wt% C_{free}) are 77 – 108 GPa[22]. Under high load, the Young's modulus of SiCO with composition $\text{SiC}_{0.8}\text{O}_{1.6}$ has been measured at 180 ± 30 GPa[46]. Our computed values of Young's modulus for the selected SiCO compositions fall within experimental ranges. However, elastic moduli for the $\text{Si}_2\text{CO}_2 + \text{C}_{\text{free}}$ are higher due to the high SiC content in the SiCO glass.

We observe that elastic moduli decrease with increasing simulation temperature for the selected SiCO compositions. Generally, elastic properties of materials decrease with increasing temperature[47, 48]. However, SiO_2 glass displays a peculiar anomalous behavior since its moduli tend to increase with increasing temperature.[49, 50] Interestingly, work from Rouxel et al.[21] indicates a similar increase of Young's modulus of SiCO glass with increasing temperature.

Impact of free carbon content

We then investigate models with different free carbon content $\text{C}_{\text{free}}:\text{Si}$, while keeping the model density and composition of the glass matrix identical. Results of shear modulus G and Young's modulus E for a series of such models generated at the same T_{max} are shown in Figure 4. We find that elastic moduli increase as the free carbon content increases as long as other parameters remain constant. The relation between modulus and carbon content appears approximately linear within the range of compositions studied here. These results seem to contradict recent experimental studies by Sorarù et al.[22]. The authors concluded that Young's modulus of SiCO ceramics decreases with increasing C_{free} content. We note, however, that the densities of the investigated samples decreased

with increasing C_{free} content. Therefore, their C_{free} content is strongly correlated to density, and the impact of one variable cannot be distinguished from the effects of the other. As we pointed out in the preceding section, decreasing density causes decreasing moduli, and the apparent disagreement can be remedied this way.

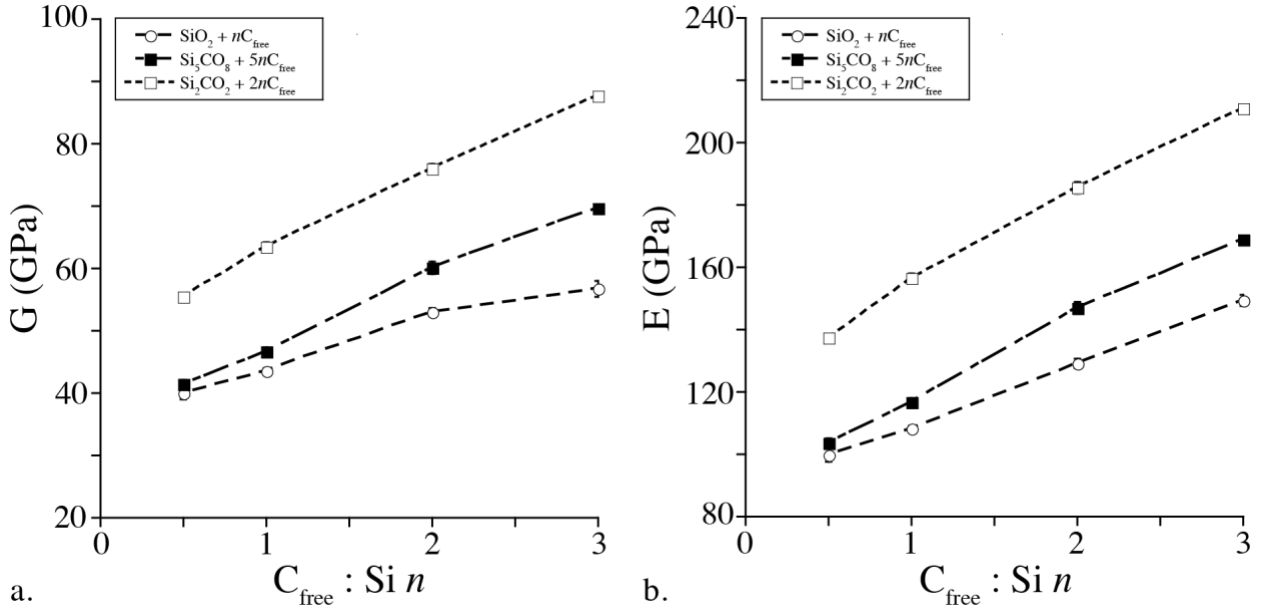


Figure 4: a. Shear modulus and b. Young's modulus vs free carbon content, $C_{\text{free}}:\text{Si}$ ratio n , for models of $\text{Si}_5\text{CO}_8 + 5nC_{\text{free}}$, $\text{SiO}_2 + nC_{\text{free}}$, $\text{Si}_2\text{CO}_2 + 2nC_{\text{free}}$ generated at $T_{\text{max}} = 3000$ K with $\rho = 2.2 \text{ g/cm}^3$. C content $C_{\text{free}}:\text{Si } n$, density $\rho = 2.2 \text{ g/cm}^3$, $T_{\text{max}} = 3000$ K. Elastic constants are calculated in triplicate for each of 3 independently generated models. Error bars (if larger than the symbol) represent standard error. Simulations are done at 300 K. Lines are provided to guide the eye.

To gain further insight into the impact of the free carbon on a modulus M , we seek the contribution of the carbon phase to moduli of the compound models. We analyze this through a simple mixing model: $M_{\text{SiCO:Cfree}} = x_{\text{SiCO}} * M_{\text{SiCO}} + x_{\text{Cfree}} * M_{\text{Cfree}}$ (x_i is the mass fraction of glass and free carbon phase), into which we insert moduli for the SiCO glass to extract moduli of the carbon phase. To obtain moduli M_{SiCO} of SiCO glass phases, we extrapolate the data shown in Figure 4 to zero C_{free} content. For SiO_2 this procedure yields $B_0 = 64$ GPa, $G = 37$ GPa, and $E = 89$ GPa. (each ± 2 GPa) Performing simulations

for pure SiO₂ (24,600 atoms, $T_{\text{max}}=2000$ K, $\rho = 2.2$ g/cm³) under conditions similar to those used for SiCO:C_{free} models, we find $B_0 = 58$ GPa, $G = 34$ GPa, $E = 85$ GPa (each ± 2 GPa). These results are well aligned with the extrapolation towards zero C content. We note that the computed bulk modulus for SiO₂ glass is considerably higher than experimentally reported ($B_0 \approx 36$ GPa, [49]). A similar extrapolation analysis yields B , G , and E of 66, 36, and 91 GPa, respectively, for Si₅CO₈. For Si₂CO₂, we obtain 84, 50, and 125 GPa for B , G , and E , respectively. We then insert the extrapolated data into the mixing model and apply it to the data shown in Figure 4. The (hypothetical) moduli M_{Cfree} of the carbon phase are obtained through best fits. We obtain reasonable agreement for a bulk modulus of the carbon phase B_{Cfree} between 90 – 111 GPa, a shear modulus G_{Cfree} within 70 – 93 GPa, and a Young's modulus E_{Cfree} between 200 – 250 GPa. Note that these values are extracted under the assumption of a mixing model based on mass fraction. The moduli extracted from the compound models can then be compared to data computed through simulations of a large model of graphite: $B = 55$ GPa, $G = 87$ GPa, and $E = 171$ (all ± 1 GPa). We also simulated (glass-free) models of amorphous carbon along the same protocol and received $B = 166$ GPa, $G = 176$ GPa, and $E = 390$ GPa (all ± 1 GPa) – in agreement with recently reported values[51]. We find that – within a simple mixing model – the free carbon phase's impact on a compound model's elastic moduli is larger than expected from mixing graphite but smaller than expected by mixing pure amorphous carbon to glassy SiCO. Overall, its impact falls between contributions expected from adding graphite or amorphous carbon.

Increasing the simulation temperature at which elastic moduli are computed, we find that all moduli decrease with increasing temperature. This is shown in Figure 5 for shear modulus and Young's modulus of selected models of SiCO (compare Figure 3 as well). The trend holds regardless of the amount of free carbon, as simulation temperature does not change the impact of free carbon on elastic properties. Models with higher free carbon content generally have higher shear and Young's modulus for any given

temperature in the investigated range. Increasing the carbon content from $C_{\text{free}}:\text{Si}$ ratio = 0.5 to $C_{\text{free}}:\text{Si}$ ratio = 3 results in almost doubling shear and Young's modulus.

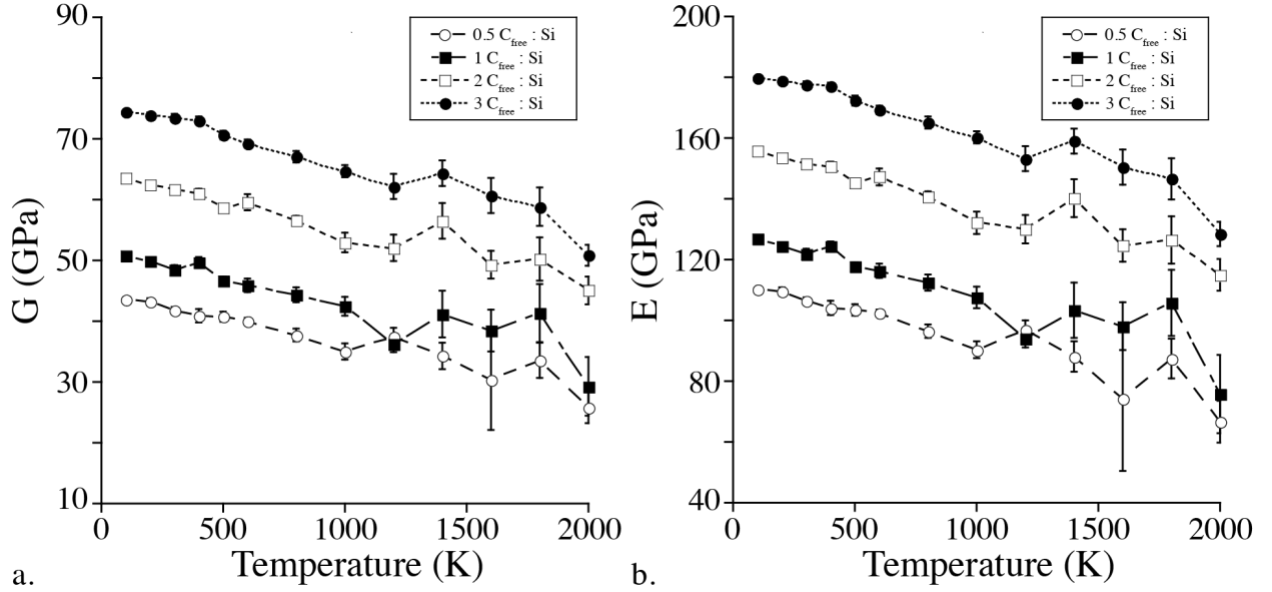


Figure 5: a. Shear modulus and b. Young's modulus of $\text{Si}_5\text{CO}_8 + 10C_{\text{free}}$ models (39,360 atoms, $a=7.9$ nm, 2.2 g/cm³) generated at $T_{\text{max}} = 4000$ K. C content $C_{\text{free}}:\text{Si} = 0.5, 1, 2, 3$, density $\rho = 2.2$ g/cm³, $T_{\text{max}} = 4000$ K. Elastic constants are calculated in triplicate for each of 3 independently generated models. Error bars represent standard error. Lines are provided to guide the eye.

Impact of carbon morphology

The most striking result we found in our investigation is the impact of the morphology of free carbon on elastic properties. Different carbon morphologies can be attained by using different maximum temperatures T_{max} during structure generation while keeping all other parameters (composition, density) identical. For instance, generating a structure at $T_{\text{max}} = 2000$ K yields a model with small groups of carbon atoms, including C_6 -rings (like benzene) and short chains, see Figure 6a. The groups are dispersed and isolated within the surrounding glass matrix. Thus, the carbon structure is not extended, and C-C bonds do not form a continuous path throughout the model. Increasing T_{max} to 4000 K yields an

extended C–C bond network with continuous paths connecting almost all C atoms. Only a minor portion of C atoms remain isolated. Indeed, most C atoms are three-connected (sp^2 -like) and found within six-membered carbon rings, like aromatic carbon segregations (Figure 6b). The network is best characterized as “sheet-like”. Notably, small amounts of SiCO glass phase separate the curved 2D sheets of carbon from each other. Generating the structure at an even higher T_{\max} (6000 K or 8000 K) results in the formation of predominantly tubular networks (Figures 6c and 6d). Details of this “genesis” of the carbon structure within SiCO and how it depends on composition, heating rate, and other simulation parameters will be given elsewhere. Note that all models shown in Figure 6 have the same composition and density.

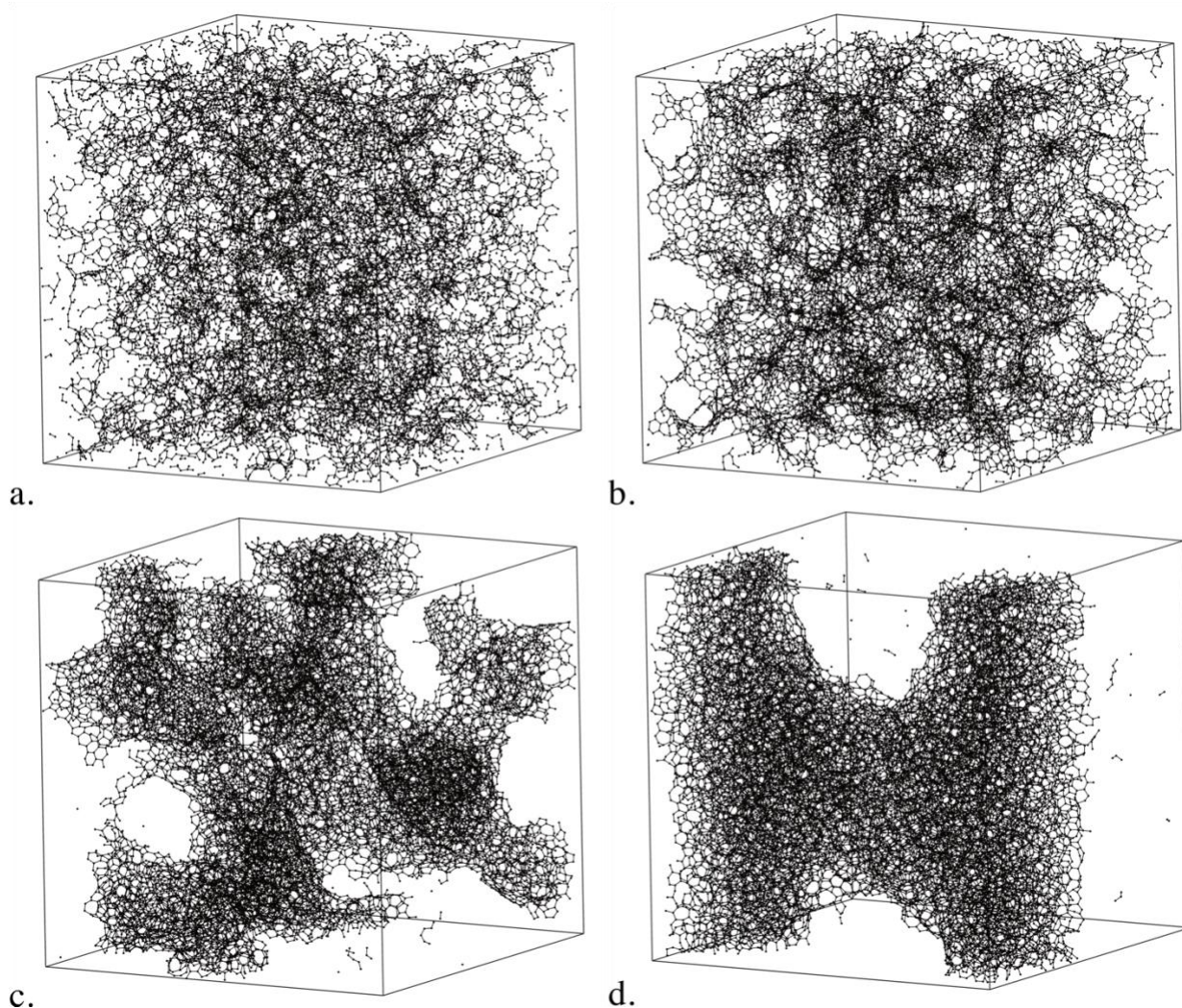


Figure 6: $\text{Si}_5\text{CO}_8 + 10\text{C}_{\text{free}}$ models (39,360 atoms; $a=7.9$ nm; 2.2 g/cm³) annealed at a. 2000 K, b. 4000 K, c. 6000 K, d. 8000 K. C content $\text{C}_{\text{free}}:\text{Si} = 2$, density $\rho = 2.2$ g/cm³, T_{max} . Only C atoms (black) are shown.

We then computed elastic moduli for these models with identical composition, carbon content, and density but different carbon morphology (as directed via T_{max}). Results, exemplified for structures with glass composition Si_5CO_8 and different amounts of free carbon, are presented in Figure 7. The data shows that elastic moduli in SiCO structures can vary by up to 25% only by changing the morphology of the carbon segregation. The impact of morphology is more pronounced the higher the carbon content is. At low free carbon content, $\text{C}_{\text{free}}:\text{Si} = 0.5$, only minor differences in moduli appear; thus, the amorphous glass matrix dominates elastic properties. Conversely, at high free carbon content, $\text{C}_{\text{free}}:\text{Si} = 3$, the impact of free carbon morphology is substantial, with up to 25% difference (136 GPa vs. 172 GPa for $\text{C}:\text{Si}=2$; 157 GPa vs. 200 GPa for $\text{C}:\text{Si}=3$).

Therefore, at high C_{free} content – when a contribution of carbon to mechanical properties is more substantial – the spatial distribution of carbon and its morphology within the compound is essential. Overall, we find that amorphous SiCO –with identical composition and density – exhibits significant variation in its mechanical properties depending on the extent and morphology of carbon segregations.

Our results highlight that caution must be applied when using a “rule-of-mixture” to estimate or analyze properties in SiCO compound systems. Rouxel et al.[21] followed such an approach when comparing elastic properties of SiCO with a volume-weighted sum of elastic properties of constituent phases. Such an approach will yield only a rough approximation since it neglects a possible impact of the morphology of the phases. Our calculations predict that the morphology of the free carbon phase does have a significant effect on elastic properties. Therefore, even when model composition and density are identical, a simple rule-of-mixture may not be sufficient in estimating the elastic properties of SiCO.

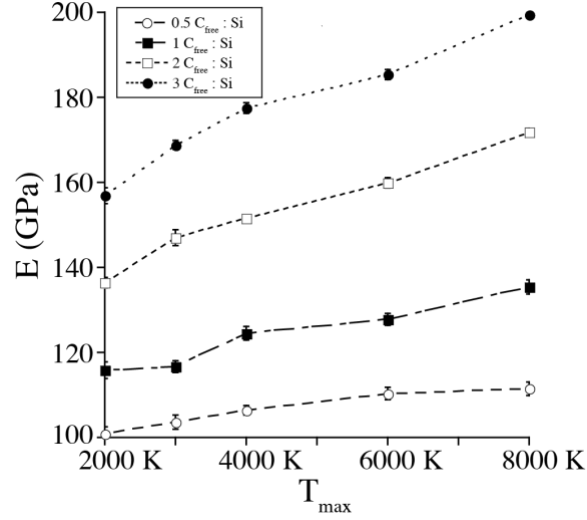


Figure 7: Young's modulus plotted as a function of T_{\max} used in model generation. $\text{Si}_5\text{CO}_8 + 5nC_{\text{free}}$ models with $\rho = 2.2 \text{ g/cm}^3$ and $C_{\text{free}}:\text{Si} = n$, with $n = 0.5, 1, 2$, and 3 . Elastic constants are calculated in triplicate for each of 3 independently generated models. Error bars represent standard error. Simulations are done at 300 K. Lines are provided to guide the eye.

We also investigated the temperature dependence of elastic properties of models with different carbon morphology, see Figure 8. Consistent with the results shown above, we find that the moduli of SiCO generally decrease with increasing temperature. At low free carbon content, here $C_{\text{free}}:\text{Si} = 0.5$, elastic properties decrease by 10 – 40% when comparing data obtained at 300K to that computed at 2000K. At high free carbon content, $C_{\text{free}}:\text{Si} = 3$, elastic properties decrease between 20 – 40 % within the investigated temperature range. There is a subtle impact of carbon morphology, identified through T_{\max} (the temperature at which models have been generated), on the “consistency” or “thermal stability” of elastic moduli. Models generated at $T_{\max} = 6000 \text{ K}$ and 8000 K have more consistent elastic properties and tend to decrease less at higher temperatures than models generated at $T_{\max} = 2000 \text{ K}$, 3000 K , and 4000 K .

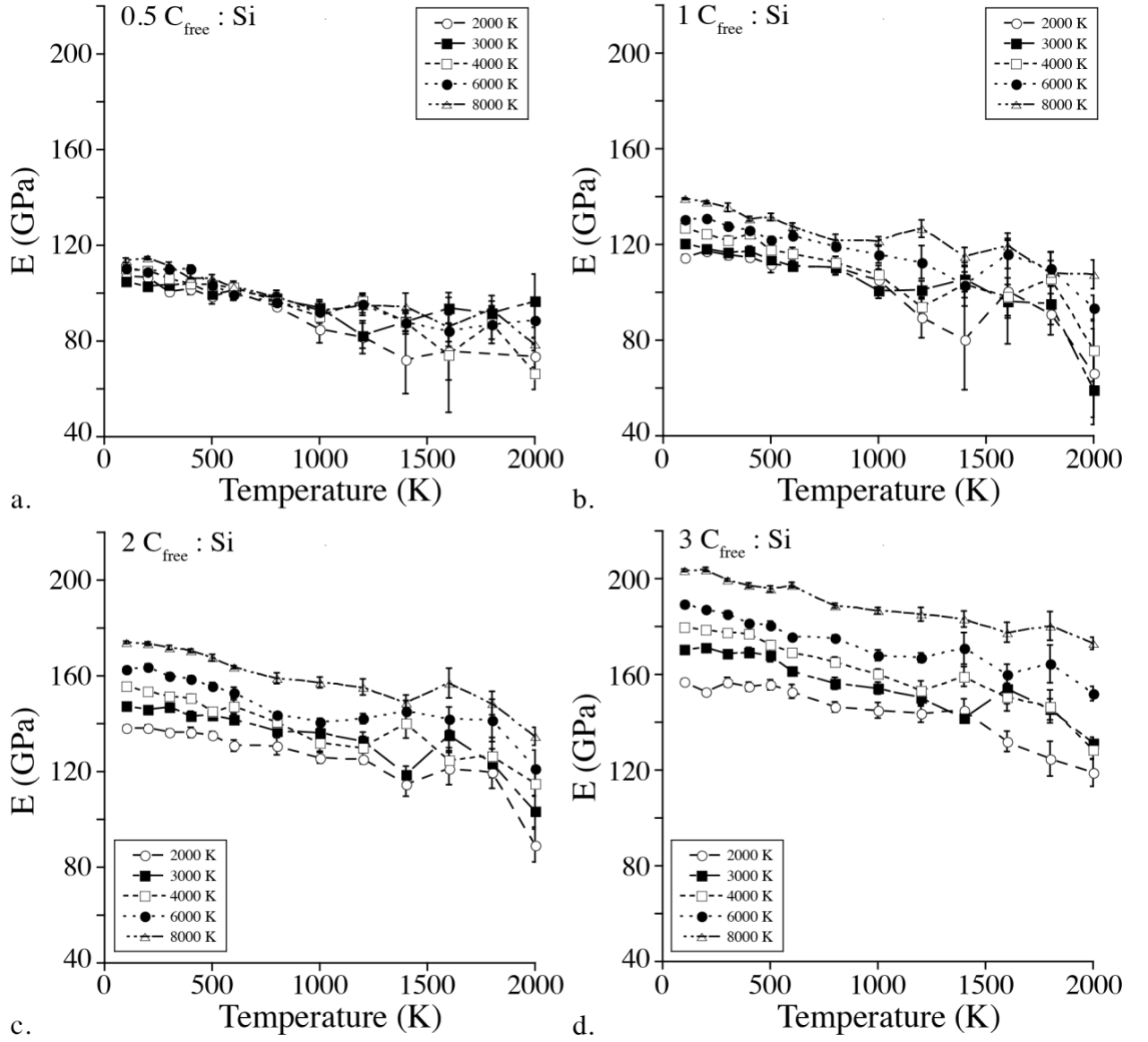


Figure 8: Young's modulus vs. simulation temperature for models of $\text{Si}_5\text{CO}_8 + 5nC_{\text{free}}$ annealed between 2000 K – 8000 K with a. $n = 0.5$, b. $n = 1.0$, c. $n = 2.0$, d. $n = 3.0$ where $n = C_{\text{free}} : \text{Si}$. density $\rho = 2.2 \text{ g/cm}^3$, T_{max} . Elastic constants are calculated in triplicate for each of 3 independently generated models. Error bars represent standard error. Lines are provided to guide the eye.

Finite-size effects

Our final investigation addresses the size of models used in this study. The initial series of our models had a characteristic unit cell extension (box dimension) of 10 nm and contained 24,000 – 50,000 atoms, depending on composition. A close look at the tubular segregations emerging for T_{max} of 6000K and 8000K, see Figures 6c and 6d, shows that these segregations have diameters of about 2 nm and 4 nm, respectively. Since these fall well into the size of the simulation cell, the periodic boundary conditions are likely to impact structure generation and property calculations. To investigate such finite-size effects, we considered the composition $\text{Si}_5\text{CO}_8 + 10\text{C}_{\text{free}}$ with a density of 2.2 g/cm^3 and generated 8 times and 64 times larger models. These comprise simulation box dimensions of approximately 20 nm and 40 nm, respectively. Three different series of 20 nm models and one series of 40 nm models were generated. We maintained all procedural parameters, including heating rates, as outlined in the method section for these simulations. In Figure 9, we show 40 nm models generated at $T_{\text{max}} = 6000 \text{ K}$ and 8000 K . The model obtained at $T_{\text{max}} = 6000 \text{ K}$ still resembles its smaller counterpart in carbon morphology. The same trend holds for models obtained at even lower temperatures. On the other side, the 40 nm model generated at $T_{\text{max}} = 8000 \text{ K}$ exhibits a 3D tubular network, which is different from the 2D tubular networks the smaller 10 nm models generated at the same T_{max} exhibit (see Figure 6d).

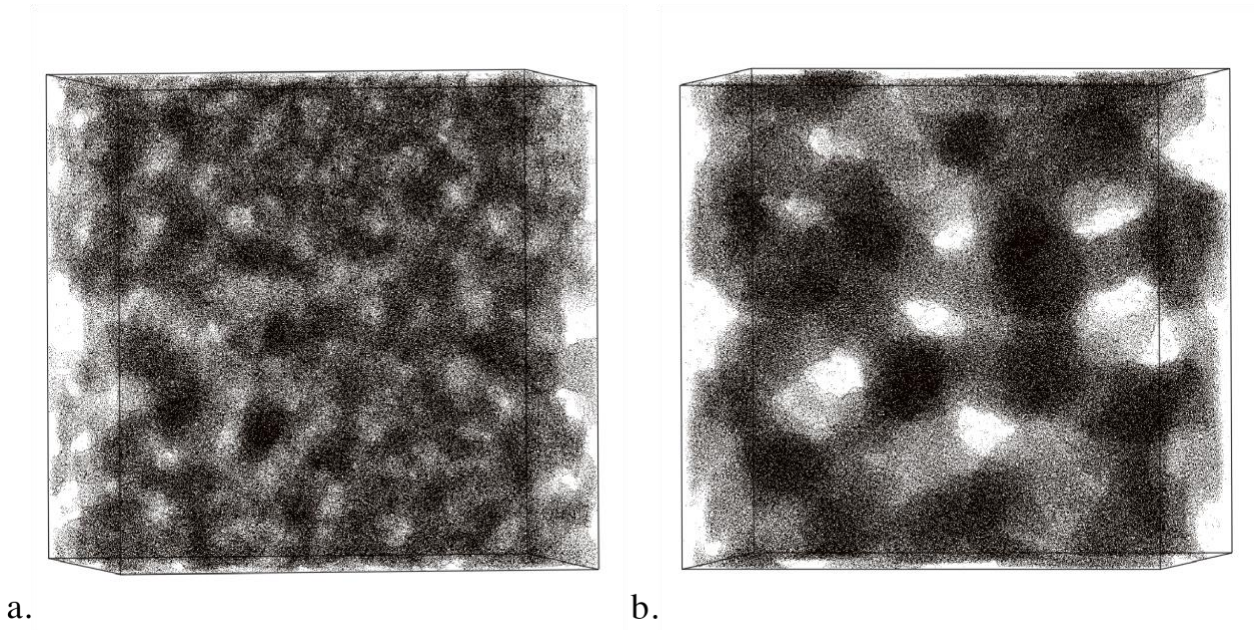


Figure 9: $\text{Si}_5\text{CO}_8 + 10\text{C}_{\text{free}}$ with $\text{C}_{\text{free}}:\text{Si} = 2$ and density $\rho = 2.2 \text{ g/cm}^3$) generated at a. $T_{\text{max}} = 6000 \text{ K}$ and b. $T_{\text{max}} = 8000 \text{ K}$. The models comprise about 2.5 million atoms within a simulation box of approximately 40 nm.

We computed Young's moduli of $\text{Si}_5\text{CO}_8 + 10\text{C}_{\text{free}}$ models in three different sizes, 10, 20, and 40 nm, generated using $T_{\text{max}} = 2000 \text{ K}$ and $T_{\text{max}} = 8000 \text{ K}$ and compared them with each other, see Figure 10. Young's moduli calculated for 20 nm and 40 nm models agree with data previously obtained for the 10 nm model. We corroborate the ~20% difference in Young's moduli between models with identical composition and density but generated at different T_{max} (2000 K vs. 8000 K). Therefore, the impact of carbon morphology on elastic properties persists for models in larger simulation boxes. On the other side, a noticeable structural difference between the 10 nm and the larger models generated at $T_{\text{max}} = 8000 \text{ K}$ relates to a 2D tubular network present in the former and 3D tubular networks found in the latter.

The most apparent benefit of simulating models of larger size emerges in simulations at elevated temperatures. The uncertainty obtained for data of a single model is much smaller, and the consistency between different models obtained through the same

protocol is much higher. The data shown in Figure 10 exemplifies this for a composition $\text{Si}_5\text{CO}_8 + 10\text{C}_{\text{free}}$: above 500 K. Young's moduli of 10 nm models generated with $T_{\text{max}} = 2000$ K exhibit substantial uncertainty. In contrast, 20 nm models provide consistent results and agree with the data of the 40 nm model. Trends are similar for models generated at $T_{\text{max}} = 8000$ K, which exhibit larger carbon segregations. Young's moduli computed for the larger models carry smaller errors and are consistent with each other. However, while the larger size models exhibit higher fidelity, we notice that all trends observed for small models are found in larger models as well – with the latter corroborating the results of the former.

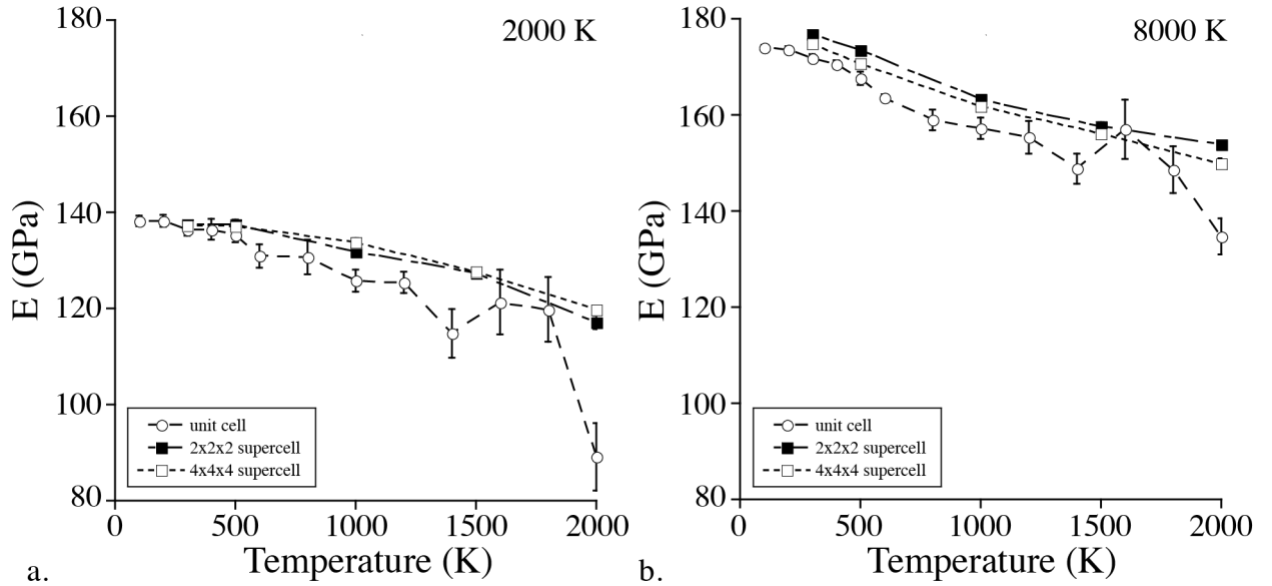


Figure 10: Young's modulus of $\text{Si}_5\text{CO}_8 + 10\text{C}_{\text{free}}$ ($\text{C}_{\text{free}}:\text{Si} = 2$, density $\rho = 2.2 \text{ g/cm}^3$) as a function of simulation temperature for models of different size attained at a. $T_{\text{max}} = 2000$ K and b. $T_{\text{max}} = 8000$ K. A unit cell of a 10 nm model contains 39,360 atoms, a 20 nm model contains 314,880 atoms, and a 40 nm model contains 2,519,040 atoms. Three models each are generated for 10 and 20 nm, while only a single model is generated with a size of 40 nm. Elastic constant calculations for all models are done in triplicate. Error bars represent standard error. Lines are provided to guide the eye.

Conclusions

Using molecular dynamics simulations with the Tersoff potential, we calculate elastic properties of SiCO models with different glass compositions, densities, C_{free} content, and carbon morphology. We examine each parameter individually and disentangle dependencies that are difficult to separate in experimental studies. In general, our results align well with expectations and previous experimental observations. In particular, higher elastic moduli are found for models with higher SiC content in the SiCO glass and for models with higher density. Dynamic simulations at finite temperatures show that for any given composition of SiCO, the elastic moduli decrease with increasing temperature. Our results then indicate that – when maintaining the density of a system – increasing the amount of C_{free} yields higher elastic moduli. While this appears to contradict previous experimental results[22], we show that density variations dominate the underlying experimental data in this study.

Finally, we uncover a “hidden” parameter – the morphology of the C_{free} phase – that impacts the mechanical properties of SiCO. Models with identical composition and density but different morphology of the same amount of C_{free} exhibit different mechanical properties. In general, models with dispersed small fragments of C_{free} have lower moduli than models with extended networks or tubular segregations of C_{free} . The effect can reach up to 25% of the mechanical property for models comprising large amounts of “free” carbon. As a consequence, caution has to be exerted if a simple rule-of-mixture based on the composition or volume content is used to predict the mechanical properties of SiCO. At this time, we are not aware of any experimental method that can quantify the morphology of “free” carbon embedded in the amorphous matrix of SiCO. Hence, we term it “hidden” and direct approaches for experimental characterization need to be developed to attain quantitative measures.

Acknowledgments

This work was supported by the National Science Foundation (NSF) through the award OISE-1743701. This work used the Extreme Science and Engineering Discovery Environment (XSEDE), supported by NSF grant number ACI-1548562. The authors acknowledge the Texas Advanced Computing Center (TACC) at The University of Texas at Austin for providing HPC resources, training, and support. Additional computational work was achieved at High-Performance Computing facilities at UTA.

References

- [1] C. Stabler, E. Ionescu, M. Graczyk-Zajac, I. Gonzalo-Juan, R. Riedel, Silicon oxycarbide glasses and glass-ceramics: “All-Rounder” materials for advanced structural and functional applications, *Journal of the American Ceramic Society* 101(11) (2018) 4817-4856.
- [2] G.M. Renlund, S. Prochazka, R.H. Doremus, Silicon oxycarbide glasses: Part II. Structure and properties, *Journal of Materials Research* 6(12) (1991) 2723-2734.
- [3] G.D. Sorarù, S. Modena, E. Guadagnino, P. Colombo, J. Egan, C. Pantano, Chemical Durability of Silicon Oxycarbide Glasses, *Journal of the American Ceramic Society* 85(6) (2002) 1529-1536.
- [4] L. Bois, J. Maquet, F. Babonneau, D. Bahloul, Structural Characterization of Sol-Gel Derived Oxycarbide Glasses. 2. Study of the Thermal Stability of the Silicon Oxycarbide Phase, *Chemistry of Materials* 7(5) (1995) 975-981.
- [5] C.M. Brewer, D.R. Bujalski, V.E. Parent, K. Su, G.A. Zank, Insights into the Oxidation Chemistry of SiOC Ceramics Derived from Silsesquioxanes, *Journal of Sol-Gel Science and Technology* 14(1) (1999) 49-68.
- [6] T. Rouxel, G.-D. Sorarù, J. Vicens, Creep Viscosity and Stress Relaxation of Gel-Derived Silicon Oxycarbide Glasses, 84(5) (2001) 1052-1058.
- [7] C. Stabler, F. Roth, M. Narisawa, D. Schliephake, M. Heilmaier, S. Lauterbach, H.-J. Kleebe, R. Riedel, E. Ionescu, High-temperature creep behavior of a SiOC glass ceramic free of segregated carbon, *Journal of the European Ceramic Society* 36(15) (2016) 3747-3753.
- [8] A. Scarmi, G.D. Sorarù, R. Raj, The role of carbon in unexpected visco(an)elastic behavior of amorphous silicon oxycarbide above 1273K, *Journal of Non-Crystalline Solids* 351(27) (2005) 2238-2243.
- [9] D. Ahn, R. Raj, Thermodynamic measurements pertaining to the hysteretic intercalation of lithium in polymer-derived silicon oxycarbide, *Journal of Power Sources* 195(12) (2010) 3900-3906.
- [10] W. Xing, A.M. Wilson, K. Eguchi, G. Zank, J.R. Dahn, Pyrolyzed Polysiloxanes for Use as Anode Materials in Lithium-Ion Batteries, *Journal of The Electrochemical Society* 144(7) (1997) 2410-2416.
- [11] A. Geissinger, J. Oberle, W. Teschner, H. Boeder, K.-H. Heussner, Ceramic electric resistor, Robert Bosch GmbH, Stuttgart, Germany, United States, 1999.

- [12] M. Harris, T. Chaudhary, L. Drzal, R.M. Laine, Silicon oxycarbide coatings on graphite fibers: chemistry, processing, and oxidation resistance, *Materials Science and Engineering: A* 195 (1995) 223-236.
- [13] H.-J. Kleebe, C. Turquat, G.D. Sorarù, Phase Separation in an SiCO Glass Studied by Transmission Electron Microscopy and Electron Energy-Loss Spectroscopy, *Journal of the American Ceramic Society* 84(5) (2001) 1073-1080.
- [14] H.-J. Kleebe, Y.D. Blum, SiOC ceramic with high excess free carbon, *Journal of the European Ceramic Society* 28(5) (2008) 1037-1042.
- [15] G.T. Burns, R.B. Taylor, Y. Xu, A. Zangvil, G.A. Zank, High-temperature chemistry of the conversion of siloxanes to silicon carbide, *Chemistry of Materials* 4(6) (1992) 1313-1323.
- [16] H.-J. Kleebe, G. Gregori, F. Babonneau, Y.D. Blum, D.B. MacQueen, S. Masse, Evolution of C-rich SiOC ceramics: Part I. Characterization by integral spectroscopic techniques: Solid-state NMR and Raman spectroscopy: Dedicated to Professor Dr. Fritz Aldinger on the occasion of his 65th birthday, *International Journal of Materials Research* 97(6) (2006) 699-709.
- [17] Y. Cao, X. Yang, L. An, Electric conductivity and microstructure evolution of polymer-derived SiAlCO ceramics, *Ceramics International* 42(3) (2016) 4033-4038.
- [18] Q. Wen, Z. Yu, R. Riedel, The fate and role of in situ formed carbon in polymer-derived ceramics, *Progress in Materials Science* 109 (2020) 100623.
- [19] S. Trassl, G. Motz, E. Rössler, G. Ziegler, Characterisation of the free-carbon phase in precursor-derived SiCN ceramics, *Journal of Non-Crystalline Solids* 293-295 (2001) 261-267.
- [20] M. Monthieux, O. Delverdier, Thermal behavior of (organosilicon) polymer-derived ceramics. V: Main facts and trends, *Journal of the European Ceramic Society* 16(7) (1996) 721-737.
- [21] T. Rouxel, G. Massouras, G.-D. Sorarù, High Temperature Behavior of a Gel-Derived SiOC Glass: Elasticity and Viscosity, *Journal of Sol-Gel Science and Technology* 14(1) (1999) 87-94.
- [22] G.D. Sorarù, L. Kundanati, B. Santhosh, N. Pugno, Influence of free carbon on the Young's modulus and hardness of polymer-derived silicon oxycarbide glasses, *Journal of the American Ceramic Society* 102(3) (2019) 907-913.
- [23] R. Gadow, F. Kern, H. Ulutas, Mechanical properties of ceramic matrix composites with siloxane matrix and liquid phase coated carbon fiber reinforcement, *Journal of the European Ceramic Society* 25(2) (2005) 221-225.
- [24] P. Weichand, R. Gadow, Basalt fibre reinforced SiOC-matrix composites: Manufacturing technologies and characterisation, *Journal of the European Ceramic Society* 35(14) (2015) 4025-4030.
- [25] P. Kroll, Modelling and simulation of amorphous silicon oxycarbide, *Journal of Materials Chemistry* 13(7) (2003) 1657-1668.
- [26] P. Kroll, Searching insight into the atomistic structure of SiCO ceramics, *Journal of Materials Chemistry* 20(46) (2010) 10528-10534.
- [27] D. Marshall, B. Cox, P. Kroll, G. Hilmas, W. Fahrenholtz, R. Raj, R. Ritchie, Q. Yang, F. Zok, National Hypersonic Science Center for Materials and Structures, 2014, p. 61.

- [28] N. Liao, M. Zhang, H. Zhou, W. Xue, Modeling of amorphous SiC_xO_{6/5} by classical molecular dynamics and first principles calculations, *Scientific Reports* 7(1) (2017) 42705.
- [29] T.A. West, Investigation of Computational Determination of Elastic Properties for Silicon Nitride and Silicon Carbonitride Materials, Chemistry and Biochemistry, The University of Texas at Arlington, 2020.
- [30] S. Plimpton, Fast Parallel Algorithms for Short-Range Molecular Dynamics, *Journal of Computational Physics* 117(1) (1995) 1-19.
- [31] J. Tersoff, New empirical approach for the structure and energy of covalent systems, *Physical Review B* 37(12) (1988) 6991-7000.
- [32] J. Tersoff, Modeling solid-state chemistry: Interatomic potentials for multicomponent systems, *Physical Review B* 39(8) (1989) 5566-5568.
- [33] J. Tersoff, Empirical Interatomic Potential for Carbon, with Applications to Amorphous Carbon, *Physical Review Letters* 61(25) (1988) 2879-2882.
- [34] S. Munetoh, T. Motooka, K. Moriguchi, A. Shintani, Interatomic potential for Si–O systems using Tersoff parameterization, *Computational Materials Science* 39(2) (2007) 334-339.
- [35] A. Thompson, ELASTIC_T LAMMPS scripts.
- [36] W. Voigt, *Lehrbuch der Kristallphysik*, B. B. Teubner, Leipzig, 1928.
- [37] A. Reuss, Berechnung der Fließgrenze von Mischkristallen auf Grund der Plastizitätsbedingung für Einkristalle, *ZAMM - Journal of Applied Mathematics and Mechanics / Zeitschrift für Angewandte Mathematik und Mechanik* 9(1) (1929) 49-58.
- [38] R. Hill, The Elastic Behaviour of a Crystalline Aggregate, *Proceedings of the Physical Society. Section A* 65(5) (1952) 349-354.
- [39] M.F. Ashby, *Materials Selection in Mechanical Design*, 2nd ed., Butterworth-Heinemann, Linacre House, Jordan Hill, Oxford, 1999.
- [40] P. Colombo, J.R. Hellmann, D.L. Shelleman, Mechanical Properties of Silicon Oxycarbide Ceramic Foams, *Journal of the American Ceramic Society* 84(10) (2001) 2245-2251.
- [41] I.V. Aleksandrov, A.F. Goncharov, S.M. Stishov, E.V. Iakovenko, Equation of state and Raman scattering of light in cubic BN and SiC at high pressures, *Pisma v Zhurnal Eksperimentalnoi i Teoreticheskoi Fiziki* 50 (1989) 116-120.
- [42] V. Kulikovskiy, V. Vorlíček, P. Boháč, M. Stranyánek, R. Čtvrtlík, A. Kurdyumov, L. Jastrabík, Hardness and elastic modulus of amorphous and nanocrystalline SiC and Si films, *Surface and Coatings Technology* 202(9) (2008) 1738-1745.
- [43] T. Deschamps, J. Margueritat, C. Martinet, A. Mermet, B. Champagnon, Elastic moduli of permanently densified silica glasses, *Scientific Reports* 4 (2014) 7193-7193.
- [44] L.-g. Liu, Bulk moduli of SiO₂ polymorphs: Quartz, coesite and stishovite, *Mechanics of Materials* 14(4) (1993) 283-290.
- [45] S. Walter, G.D. Soraru, H. Bréquel, S. Enzo, Microstructural and mechanical characterization of sol gel-derived Si–O–C glasses, *Journal of the European Ceramic Society* 22(13) (2002) 2389-2400.
- [46] C. Moysan, R. Riedel, R. Harshe, T. Rouxel, F. Augereau, Mechanical characterization of a polysiloxane-derived SiOC glass, *Journal of the European Ceramic Society* 27(1) (2007) 397-403.

- [47] J.B. Wachtman Jr., D.G. Lam Jr., Young's Modulus of Various Refractory Materials as a Function of Temperature, *Journal of the American Ceramic Society* 42(5) (1959) 254-260.
- [48] R. Farraro, R.B. McLellan, Temperature dependence of the Young's modulus and shear modulus of pure nickel, platinum, and molybdenum, *Metallurgical Transactions A* 8(10) (1977) 1563-1565.
- [49] A. Polian, D. Vo-Thanh, P. Richet, Elastic properties of a-SiO₂ up to 2300 K from Brillouin scattering measurements, *Europhysics Letters (EPL)* 57(3) (2002) 375-381.
- [50] M.K. Rabia, S. Degioanni, C. Martinet, J. Le Brusq, B. Champagnon, D. Vouagner, A-thermal elastic behavior of silicate glasses, *Journal of Physics: Condensed Matter* 28(7) (2016) 075402.
- [51] R. Jana, D. Savio, V.L. Deringer, L. Pastewka, Structural and elastic properties of amorphous carbon from simulated quenching at low rates, *Modelling and Simulation in Materials Science and Engineering* 27(8) (2019) 085009.

Summary

Through finite temperature molecular dynamics simulations, we computed elastic properties of SiCO with varying compositions of the glass, free carbon content, density, and free carbon morphology. We found that increasing simulation temperature resulted in decreasing elastic moduli. By independently varying free carbon content and density, we calculated that elastic properties of SiCO generally increase when only free carbon content is increased and when only density is increased contradicting Sorarù et al.[1]. By varying the free carbon morphology while keeping composition and density constant, we calculated that elastic properties increase with increasing segregation of the free carbon phase. Models with small dispersed carbon fragments had lower elastic moduli than models with extended free carbon networks. Thus, controlling the morphology of the free carbon phase can be used to tailor elastic properties of SiCO PDCs. Finally, we verified our results using substantially larger, million atom models for the $\text{Si}_5\text{CO}_8 + 10\text{C}_{\text{free}}$ composition, and we found that general trends agree with the trends we computed with smaller models.

References

[1] G.D. Sorarù, L. Kundanati, B. Santhosh, N. Pugno, Influence of free carbon on the Young's modulus and hardness of polymer-derived silicon oxycarbide glasses, *Journal of the American Ceramic Society* 102(3) (2019) 907-913.

CHAPTER 2: QUANTIFICATION OF FREE CARBON PHASE MORPHOLOGY

Substantial work has been done on investigating the structural evolution of “free” carbon in polymer-derived ceramics[1-3]. From our own work in Part II Chapter 1, we identify a need to quantify the free carbon phase morphology in amorphous SiCO/SiCN ceramics in atomistic systems used in computational investigations. So, we propose a method to quantify, in part, free carbon phase morphology. We develop our method to discriminate between different free carbon morphologies by calculating the “extent” of the 3-coordinated carbon network.

In order to differentiate between free carbon morphologies, we focus on a topological shell counting method. The topological shell counting method determines the 3-coordinated carbon character of “free” carbon structures. This method calculates the fraction of 3-coordinated carbons that are themselves coordinated to 3-coordinated carbon for n th successive fractions. Essentially, the topological shell counting method measures the topological shell to which the free carbon network extends to. Carbon allotropes, such as graphite and carbon nanotubes, which only consist of 3-coordinated carbons will always yield a value of unity (1) for the “ n th fraction” as the counted topological shell approaches its maximal value; however, the “free” carbon phase in SiCO ceramics contains a mixture of differently coordinated carbons resulting in a decrease of the “ n th fraction” to zero as the counted topological shell approaches larger values. The relationship between the “ n th fraction” and the topological shell differs based on “free” carbon structure and, consequently, can provide limited differentiation between “free” carbon structures.

Models of SiCO are generated following the approach detailed in Part II Chapter 1. Molecular dynamics simulations are performed with LAMMPS[4] and interactions are described via the Tersoff potential[5, 6]. Si–Si, Si–C, and C–C interactions are parameterized by Tersoff[5-7] and Si–O interactions are parameterized by Munetoh et

al.[8] Based on spectroscopic evidence[9], interactions between O atoms and between C and O are left as repulsive only. We generate SiCO models through a melt-quench process where the parameter T_{\max} , the maximum temperature the system is exposed to, determines the morphology of the free carbon phase as long as composition and density are fixed. The system is equilibrated for 200 ps at T_{\max} , and then cooled to 300 K at a rate of 10 K/ps. All simulations are done at constant volume so models have fixed density.

We choose a composition of $\text{Si}_5\text{CO}_8 + 10\text{C}_{\text{free}}$ and T_{\max} of 2000 K, 4000 K, 6000 K, and 8000 K to generate four models with over 300,000 atoms (see Figure 1) for each T_{\max} (12 models total). Models contain 144,320 carbons atoms. For lower T_{\max} , we observe more dispersed carbon chunks and carbon six-rings (see Figure 1a and Figure 1b). Increasing T_{\max} leads to the formation of extended tubular networks (see Figure 1c and Figure 1d).

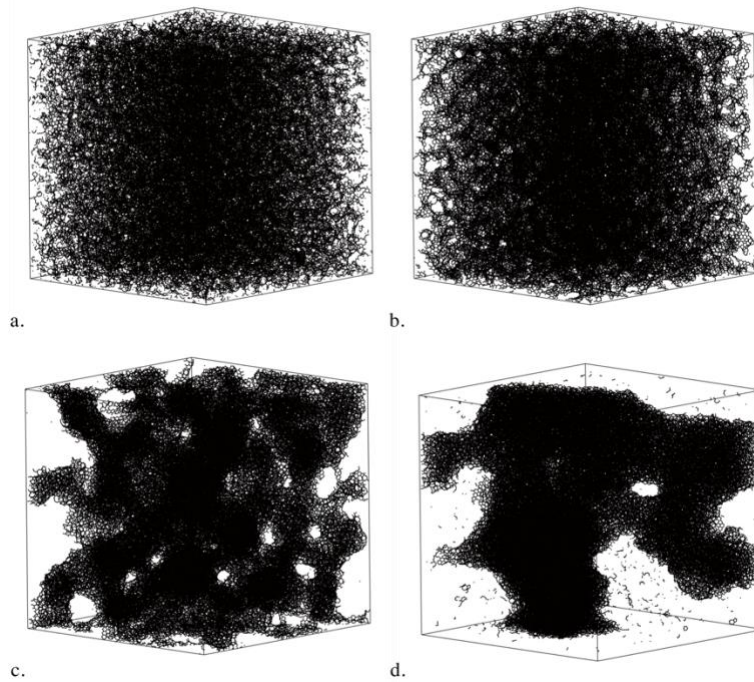


Figure 1: $\text{Si}_5\text{CO}_8 + 10\text{C}_{\text{free}}$ (314,880 atoms; 144,320 C atoms; $a = 15.8$ nm; $\rho = 2.2$ g/cm³). Generated at T_{\max} equals a. 2000 K, b. 4000 K, c. 6000 K, and d. 8000 K. Only C atoms (black) are shown.

We apply our topological shell counting method on the free carbon phase of the 12 models we generated (see Figure 2). While models produced at $T_{\max} = 2000$ K and $T_{\max} = 4000$ K have C_{free} morphologies that appear visually similar, the extents of their free carbon networks differ substantially: the free carbon network of $\text{Si}_5\text{CO}_8 + 10C_{\text{free}}$ generated with $T_{\max} = 2000$ K does not extend past the 40th topological shell while the free carbon network of $\text{Si}_5\text{CO}_8 + 10C_{\text{free}}$ generated with $T_{\max} = 4000$ K extends past the 100th topological shell. Additionally, we find that models generated at $T_{\max} = 6000$ K, and not at $T_{\max} = 8000$ K, exhibit the most extended free carbon networks of the models investigated; however, it is likely that the “small” size of the box used to generate models inhibits the extent of the free carbon phase generated at $T_{\max} = 8000$ K. Increasing the size of the simulation box could result in the true extent of the free carbon network being realized for models generated at $T_{\max} = 8000$ K.

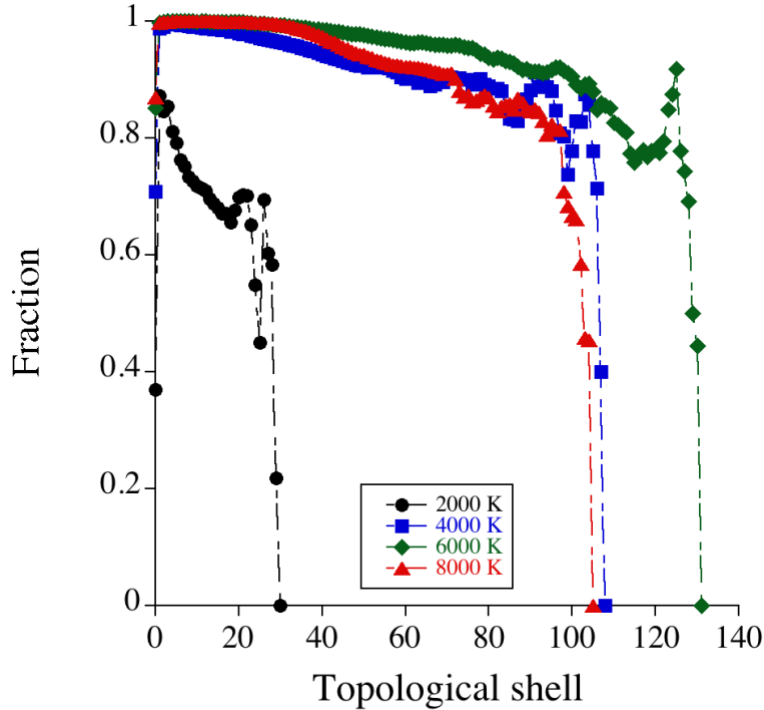


Figure 2: Topological shell counting method applied to carbon atoms in $\text{Si}_5\text{CO}_8 + 10C_{\text{free}}$ generated at $T_{\max} = 2000$ K, 4000 K, 6000 K, and 8000 K. The topological shell counting method is averaged over the results of three models for each T_{\max} .

In summary, we develop a method to partially quantify the free carbon phase morphology in carbon-containing amorphous materials by determining the extent of the three-coordinated carbon network. Using amorphous models of SiCO with different free carbon phase morphologies we demonstrate how much the extent of the free carbon phase can vary depending on the conditions used to produce the model. Our method may have application in quantitatively relating properties that depend on the free carbon phase, like elastic properties, to the morphologies of the free carbon phase.

References

- [1] H.-J. Kleebe, G. Gregori, F. Babonneau, Y.D. Blum, D.B. MacQueen, S. Masse, Evolution of C-rich SiOC ceramics: Part I. Characterization by integral spectroscopic techniques: Solid-state NMR and Raman spectroscopy: Dedicated to Professor Dr. Fritz Aldinger on the occasion of his 65th birthday, *International Journal of Materials Research* 97(6) (2006) 699-709.
- [2] Y. Cao, X. Yang, L. An, Electric conductivity and microstructure evolution of polymer-derived SiAlCO ceramics, *Ceramics International* 42(3) (2016) 4033-4038.
- [3] S. Trassl, G. Motz, E. Rössler, G. Ziegler, Characterisation of the free-carbon phase in precursor-derived SiCN ceramics, *Journal of Non-Crystalline Solids* 293-295 (2001) 261-267.
- [4] S. Plimpton, Fast Parallel Algorithms for Short-Range Molecular Dynamics, *Journal of Computational Physics* 117(1) (1995) 1-19.
- [5] J. Tersoff, New empirical approach for the structure and energy of covalent systems, *Physical Review B* 37(12) (1988) 6991-7000.
- [6] J. Tersoff, Modeling solid-state chemistry: Interatomic potentials for multicomponent systems, *Physical Review B* 39(8) (1989) 5566-5568.
- [7] J. Tersoff, Empirical Interatomic Potential for Carbon, with Applications to Amorphous Carbon, *Physical Review Letters* 61(25) (1988) 2879-2882.
- [8] S. Munetoh, T. Motooka, K. Moriguchi, A. Shintani, Interatomic potential for Si–O systems using Tersoff parameterization, *Computational Materials Science* 39(2) (2007) 334-339.
- [9] L. Bois, J. Maquet, F. Babonneau, D. Bahloul, Structural Characterization of Sol-Gel Derived Oxycarbide Glasses. 2. Study of the Thermal Stability of the Silicon Oxycarbide Phase, *Chemistry of Materials* 7(5) (1995) 975-981.

CHAPTER 3: DEVELOPMENT OF A REACTIVE FORCE FIELD FOR SIMULATIONS OF SiCNH POLYMER-DERIVED CERAMICS

Motivation and Scope

DFT calculations to study structural features of polymer-derived ceramics along with the polymer-to-ceramic conversion process can extend from months to year with current computational resources. Additionally, systems sizes are too limited by DFT in order to study and characterize the evolution of the free carbon phase during the polymer-to-ceramic conversion process which can require models tens of nanometers large. ReaxFF can be parametrized to have DFT-like accuracy for simulations with systems 10-100 times larger than currently possible in DFT. Previous work has been done parameterizing ReaxFF for investigating mechanical properties[1] and the polymer-to-ceramic conversion process involved in the synthesis of silicon oxycarbide[2, 3]. There are no complete parameter sets in literature for performing simulations of silicon carbonitrides, and existing SiCNH parameter sets were parameterized for studying different phenomena and are unsuitable for simulations of silicon carbonitride[4, 5]. We parameterize ReaxFF in order to investigate the polymer-to-ceramic conversion during the pyrolysis of polysilazanes.

References

- [1] A. Vashisth, S. Khatri, S.H. Hahn, W. Zhang, A.C.T. van Duin, M. Naraghi, Mechanical size effects of amorphous polymer-derived ceramics at the nanoscale: experiments and ReaxFF simulations, *Nanoscale* 11(15) (2019) 7447-7456.
- [2] H. Gao, H. Wang, Z. Zhao, M. Niu, L. Su, Y. Wei, Reactive Dynamics Simulation Study on the Pyrolysis of Polymer Precursors To Generate Amorphous Silicon Oxycarbide Structures, *The Journal of Physical Chemistry C* 122(10) (2018) 5767-5773.

- [3] I. Ponomarev, A.C.T. van Duin, P. Kroll, Reactive Force Field for Simulations of the Pyrolysis of Polysiloxanes into Silicon Oxycarbide Ceramics, *The Journal of Physical Chemistry C* 123(27) (2019) 16804-16812.
- [4] A.D. Kulkarni, D.G. Truhlar, S. Goverapet Srinivasan, A.C.T. van Duin, P. Norman, T.E. Schwartzentruer, Oxygen Interactions with Silica Surfaces: Coupled Cluster and Density Functional Investigation and the Development of a New ReaxFF Potential, *The Journal of Physical Chemistry C* 117(1) (2013) 258-269.
- [5] Y. Wang, Y. Shi, Q. Sun, K. Lu, M. Kubo, J. Xu, Development of a Transferable ReaxFF Parameter Set for Carbon- and Silicon-Based Solid Systems, *The Journal of Physical Chemistry C* 124(18) (2020) 10007-10015.

DEVELOPMENT OF A REACTIVE FORCE FIELD FOR SIMULATIONS OF SiCNH POLYMER-DERIVED CERAMICS

Introduction

SiCN polymer-derived ceramics (PDCs) exhibit interesting properties including corrosion resistance[1] and oxidation resistance[2]. Currently, SiCN ceramics are under investigation for a variety of applications including being used as anodes in lithium-ion batteries[3], as coatings with excellent mechanical properties[4, 5], and as low- κ dielectric thin films serving as diffusion barriers for Cu in microelectronic devices[6]. SiCN ceramics can be synthesized through the polymer-to-ceramic conversion of polysilazanes. During the polymer-to-ceramic conversion process, if a pyrolysis temperature between 1073 – 1573 K is reached and the starting polymer precursors contain enough excess carbon then the resulting SiCN ceramic can be described as a mixture of Si_3N_4 , SiC, and a “free” carbon phase, C_{free} , which consists of carbon that is almost completely bonded to other carbon. The composition of the SiCN ceramic is $\text{SiC}_x\text{N}_y = (y/4)\text{Si}_3\text{N}_4 + (1 - 3y/4)\text{SiC} + (x + 3y/4 - 1)\text{C}_{\text{free}}$.

Although, DFT has been instrumental in investigating the structural features of amorphous ceramics[7, 8], system sizes are limited to thousands of atoms and the computational expense and time of doing molecular dynamics simulations is extraordinary. Classical potentials, like the Tersoff potential[9], can perform molecular dynamics simulations for systems more than hundreds of millions of atom large and are useful in studying specific properties[10]; however, the outcome of empirical potential simulations can exhibit poor local bonding environments[11] and can lack proper description of bond breaking. The reactive force field ReaxFF[12] is meant to bridge the gap between the quantum chemical accuracy of DFT and the large system size limit of empirical potentials. ReaxFF can be parametrized to have quantum chemical accuracy[12, 13] while being able to simulate systems thousands of times the size of what

DFT can do. The principle on which ReaxFF is formulated is that all terms leading to the total ReaxFF energy of system depend on the bond order[12]. Thus, varying the bond order can result in the “formation” and “breaking” of bonds.

As far as we know, there exists no ReaxFF Si-C-N-H parameter set suitable for simulations involving the polymer-to-ceramic conversion of polysilazanes, but several ReaxFF parameter sets have been used to investigate SiCO PDCs which are similar to SiCN PDCs. Vashisth et al.[14] investigated mechanical properties of polymer-derived SiCO nanofibers within ReaxFF. Meanwhile, Gao et al.[15] studied the pyrolysis of the polymethylhydrosiloxane-hydridopolycarbosilane system using parameters developed by Newsome et al[16]. Ponomarev et al.[17] improved on the parameter set of Newsome et al.[16] and developed new ReaxFF parameters to study the pyrolysis of polysiloxanes into ceramics, including the pyrolysis of the cross-linked polymethylhydrosiloxane-divinylbenzene system.

Certain parameter sets in literature do contain Si-C-N-H parameters in various forms. Kulkarni et al.[18] developed ReaxFF parameters to study oxygen interactions with SiO₂ surfaces though their parameter set also happened to contain Si-N-H parameters. Meanwhile, a Si-C-N-O-H parameter set was trained to study carbon-based and silicon-based lubricating systems[19]. However, these parameter sets lack critical Si-C-N angle parameters.

We develop ReaxFF Si-C-N-H parameters in order to perform atomistic simulations of Si-C-N-H structures. Parameters are trained on a variety of SiC, Si₃N₄, SiCN, and SiCNH structures calculated with DFT total energy calculations and simulated with DFT ab initio molecular dynamics. The resulting parameters are used to investigate the polymer-to-ceramic conversion process of the polysilazane Ceraset.

Method

Parameter fitting

We started with the parameter set of Kulkarni et al.[18]. For C and Si atomic parameters and Si-C, C-C, and C-H parameters we substituted in parameters from Ponomarev et al.[17]. The training set consisted of amorphous and crystalline structures of Si₃N₄, SiC, C₃N₄ and C₂N, SiCN with and without C_{free}, and SiCNH polymers. Additionally, NH₃, SiH₄, and CH₄ structures comprised part of the training set. A critical part of the training set were trajectories obtained from ab initio molecular dynamics.

DFT calculations were performed with VASP[20-23] with exchange-correlation described by the PBE functional[24, 25]. Calculations utilized the projector-augmented wave (PAW) method[26, 27] with a plane wave kinetic energy cutoff of 500 eV, and forces were converged to 5 meV/Å. ab initio molecular dynamics (aiMD) were performed within the NVT ensemble using a time step of 1.0 fs and a lower plane wave kinetic energy cutoff was used. Grimme's DFT-D2 method[28] was applied to describe dispersion interactions during aiMD .

ReaxFF parameters were optimized using a custom C-code following the approach of the ReaxFF FORTRAN program of the van Duin group[12]. Parameter fitting was done through a single-parameter search using parabolic interpolation[29]. ReaxFF energies differences were fit to corresponding DFT energy differences (see Equation 1). Additionally, ReaxFF atomic forces were fit to corresponding DFT atomic forces (see Equation 2) following the approach of Ercolessi et al.[30]. The error due to energy difference mismatch and the error due to force mismatch was added, in weighted manner, into a total objective error that was minimized (see Equation 3).

$$\text{energy error} = \sum_i \frac{(E_i^{\text{ReaxFF}} - E_i^{\text{DFT}})^2}{\text{weight}^2} \quad (1)$$

$$\text{force error} = \sum_j \frac{1}{3N_j} \sum_i \frac{(F_{x,i}^{\text{ReaxFF}} - F_{x,i}^{\text{DFT}})^2 + (F_{y,i}^{\text{ReaxFF}} - F_{y,i}^{\text{DFT}})^2 + (F_{z,i}^{\text{ReaxFF}} - F_{z,i}^{\text{DFT}})^2}{\text{weight}^2} \quad (2)$$

$$\text{total error} = 100 \times \text{energy error} + \text{force error} \quad (3)$$

ReaxFF is comprised of seven types of parameters: general parameters, atom parameters, bond parameters, off-diagonal terms, valence angle parameters, torsion angle parameters, and hydrogen bond parameters. For our purposes we only optimized Si and N atomic parameters, all bonding parameters and off-diagonal terms resulting from any combination of two elements in Si-C-N-H, and all valence angle parameters resulting from any combination of three elements in Si-C-N-H. Parameter fitting was done in batches by optimizing a subset of randomly chosen parameters along with a subset of the training set.

ReaxFF calculations and simulations were done in LAMMPS[31] using the USER-REAXC package[32]. Charge equilibration was done every step and momentum was rescaled every step. A time step of 0.4 fs was used for all calculations.

Results and Discussions

Evaluation of the new parameter set

We evaluate our final parameter set by determining how well ReaxFF energy differences correspond to DFT energy differences for a set of hypothetical crystalline Si-C-N structures (see Figure 1). Energy correspondence is examined for DFT-optimized structures by calculating the corresponding energies in ReaxFF before constant volume relaxation and after constant volume relaxation. A slope of 1 indicates ideal energy correspondence. Following our approach to fitting parameters, ReaxFF energies before constant volume relaxation exhibit strong correlation with DFT energies with slopes near or around 1. Even ReaxFF energies calculated after constant volume relaxation exhibit moderately strong correlation with DFT energies.

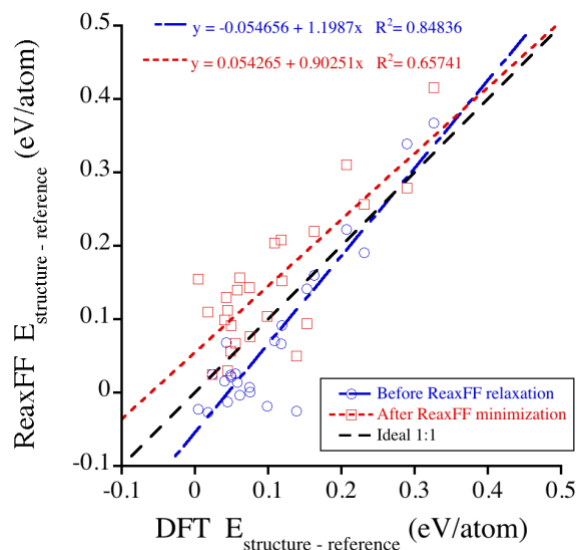


Figure 1: Energy correspondence between ReaxFF and DFT energy differences for $15\text{SiC} + 3\text{Si}_3\text{N}_4$ ($\text{Si}_3\text{N}_4:\text{SiC} = 0.2$). Static energies are calculated within ReaxFF without relaxation of DFT-optimized structures, and minimized energies are calculated within ReaxFF after constant volume optimization of DFT-optimized structures within ReaxFF. Energies are relative to the lowest energy Si-C-N structure calculated with the corresponding method (Reference structure ReaxFF energies before minimization: -6.07 eV/atom and after minimization: -6.38 eV/atom). The ideal 1:1 energy correspondence is indicated with a dashed line.

Simulation of Ceraset

We perform a simulation of KiON Ceraset Polysilazane 20, or Ceraset for short, within ReaxFF. Ceraset consists of an alternating backbone of Si and N with vinyl and methyl groups on 20% of the silicon and methyl groups on the remaining 80% of silicon. Markel et al. [33] studied the pyrolysis of two Ceraset brands, PSZ10 and PSZ20, under inert atmosphere and found the primary gaseous products evolved are H_2 and CH_4 with a significant amount of N_2 being evolved above 1484°C due to the reaction between Si_3N_4 and C.

We model Ceraset using an infinitely long strand (132 atoms) (see Figure 2a) and then create a $4 \times 4 \times 4$ supercell of the single-strand model to get 64 infinitely long strands

(8448 atoms) for simulation purposes (see Figure 2b). Simulations are done with an NpT ensemble using a pressure of 2000 bar to prevent foaming of the polymer following the approach of Ponomarev et al.[17] The Ceraset system is equilibrated at 2000 K for 20 ps and the evolution of different gaseous species is observed.

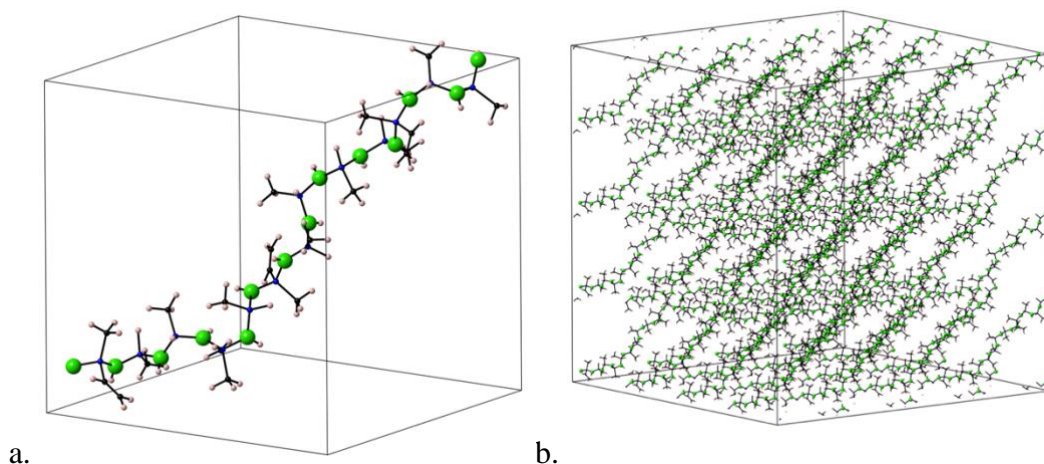


Figure 2: a. Infinite single strand of Ceraset $\text{Si}_{15}\text{C}_{21}\text{N}_{15}\text{H}_8$ ($a=21 \text{ \AA}$; $\rho = 0.17 \text{ g/cm}^3$) b. $4 \times 4 \times 4$ supercell of single strand of Ceraset $\text{Si}_{960}\text{C}_{1344}\text{N}_{960}\text{H}_{5184}$ ($a=84 \text{ \AA}$, $\rho = 0.17 \text{ g/cm}^3$). Blue atoms are Si, green balls atom N, black atoms are C, and pink atoms are H. Models displayed with CrystalMaker[34].

We observe the formation of different gaseous species including H_2 , CH_4 , and NH_3 ; the most common abundant gaseous species evolved are CH_4 and H_2 similar to what Markel et al.[33] observed. After equilibration at 2000 K, the Ceraset system is heated to 3000 K at 10 K/ps and equilibrated for 400 ps in order to expedite reactions. Afterward, the system is cooled at 10 K/ps. The outcome of the simulation (see Figure 3) is a ternary spheroid structure with surrounding unreacted gaseous species. The spheroid structure is an agglomeration of Si-C-N-H and contains Si-Si, Si-C, Si-N, C-C, and C-N bonds (with H on the periphery) thus at least agreeing qualitatively with experiment[35] though there is an overabundance of single C-N bonds. Gaseous species formed during simulation at elevated temperatures mostly persist to the end of the simulation at 300 K.

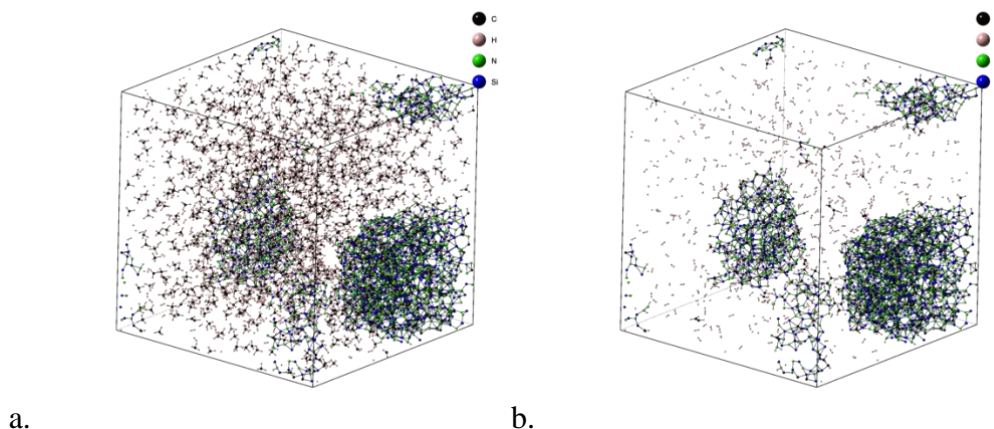


Figure 3: Ceraset $\text{Si}_{960}\text{C}_{1344}\text{N}_{960}\text{H}_{5184}$ at 900 K after constant pressure simulation up to 3000 K ($a=54.6 \text{ \AA}$, $\rho = 0.63 \text{ g/cm}^3$) with a. all atoms displayed and b. methane removed from display. Models displayed with CrystalMaker[34].

Summary

We optimize a new Si-C-N-H ReaxFF parameter set for simulation of the pyrolysis of polysilazane into amorphous SiCN ceramics. The new parameter set is trained on a diverse set of hypothetical and crystalline structures optimized in DFT. Upon evaluating the new parameter set, we find that ReaxFF and DFT energies are correlated, and energy correspondence is close to 1:1. Simulation of the polysilazane polymer Ceraset at elevated temperature is done in order to determine the types of gaseous species that evolve and what final structure may result. We find that the major gaseous species evolved during simulation of Ceraset, CH_4 and H_2 , agree with experiment[33].

Additionally, the resulting ternary agglomerate that forms at the end of the simulation exhibits bonding found in amorphous SiCN ceramics[35]. However, the abundance of C-N bonds indicates that further improvement of the parameters is required before meaningful results can be produced, including pyrolysis simulations with gas removal.

References

- [1] W. Weibelzahl, G. Motz, D. Suttor, G. Ziegler, Corrosion Stability and Mechanical Properties of Polysilazane-Derived SiCN-Ceramics, *Key Engineering Materials* 161-163 (1998) 111-114.
- [2] X. Long, C. Shao, S. Zhang, Y. Wang, Effects of C/N ratios on the oxidation resistance of SiCN fibers in air, *Corrosion Science* 182 (2021) 109270.
- [3] M. Graczyk-Zajac, L.M. Reinold, J. Kaspar, P.V.W. Sasikumar, G.-D. Soraru, R. Riedel, New Insights into Understanding Irreversible and Reversible Lithium Storage within SiOC and SiCN Ceramics, 5(1) (2015) 233-245.
- [4] P. Jedrzejowski, J. Cizek, A. Amassian, J.E. Klemberg-Sapieha, J. Vlcek, L. Martinu, Mechanical and optical properties of hard SiCN coatings prepared by PECVD, *Thin Solid Films* 447-448 (2004) 201-207.
- [5] A. Bendeddouche, R. Berjoan, E. Bêche, R. Hillel, Hardness and stiffness of amorphous SiC_xN_y chemical vapor deposited coatings, *Surface and Coatings Technology* 111(2) (1999) 184-190.
- [6] C. Jung, S. Song, H. Park, Y. Kim, E.J. Lee, S.G. Lee, H. Jeon, Characteristics of carbon-containing low-k dielectric SiCN thin films deposited via remote plasma atomic layer deposition, 39(4) (2021) 042404.
- [7] P. Kroll, Modelling and simulation of amorphous silicon oxycarbide, *Journal of Materials Chemistry* 13(7) (2003) 1657-1668.
- [8] P. Kroll, Searching insight into the atomistic structure of SiCO ceramics, *Journal of Materials Chemistry* 20(46) (2010) 10528-10534.
- [9] J. Tersoff, New empirical approach for the structure and energy of covalent systems, *Physical Review B* 37(12) (1988) 6991-7000.
- [10] Y.-Y. Zhang, Q.-X. Pei, Z.-D. Sha, Y.-W. Zhang, A molecular dynamics study of the mechanical properties of h-BCN monolayer using a modified Tersoff interatomic potential, *Physics Letters A* 383(23) (2019) 2821-2827.
- [11] A. Dasmahapatra, P. Kroll, Modeling amorphous silicon nitride: A comparative study of empirical potentials, *Computational Materials Science* 148 (2018) 165-175.
- [12] A.C.T. van Duin, S. Dasgupta, F. Lorant, W.A. Goddard, ReaxFF: A Reactive Force Field for Hydrocarbons, *The Journal of Physical Chemistry A* 105(41) (2001) 9396-9409.
- [13] S.G. Srinivasan, A.C.T. van Duin, P. Ganesh, Development of a ReaxFF Potential for Carbon Condensed Phases and Its Application to the Thermal Fragmentation of a Large Fullerene, *The Journal of Physical Chemistry A* 119(4) (2015) 571-580.
- [14] A. Vashisth, S. Khatri, S.H. Hahn, W. Zhang, A.C.T. van Duin, M. Naraghi, Mechanical size effects of amorphous polymer-derived ceramics at the nanoscale: experiments and ReaxFF simulations, *Nanoscale* 11(15) (2019) 7447-7456.
- [15] H. Gao, H. Wang, Z. Zhao, M. Niu, L. Su, Y. Wei, Reactive Dynamics Simulation Study on the Pyrolysis of Polymer Precursors To Generate Amorphous Silicon Oxycarbide Structures, *The Journal of Physical Chemistry C* 122(10) (2018) 5767-5773.
- [16] D.A. Newsome, D. Sengupta, H. Foroutan, M.F. Russo, A.C.T. van Duin, Oxidation of Silicon Carbide by O₂ and H₂O: A ReaxFF Reactive Molecular Dynamics Study, Part I, *The Journal of Physical Chemistry C* 116(30) (2012) 16111-16121.
- [17] I. Ponomarev, A.C.T. van Duin, P. Kroll, Reactive Force Field for Simulations of the Pyrolysis of Polysiloxanes into Silicon Oxycarbide Ceramics, *The Journal of Physical Chemistry C* 123(27) (2019) 16804-16812.

- [18] A.D. Kulkarni, D.G. Truhlar, S. Goverapet Srinivasan, A.C.T. van Duin, P. Norman, T.E. Schwartzentruber, Oxygen Interactions with Silica Surfaces: Coupled Cluster and Density Functional Investigation and the Development of a New ReaxFF Potential, *The Journal of Physical Chemistry C* 117(1) (2013) 258-269.
- [19] Y. Wang, Y. Shi, Q. Sun, K. Lu, M. Kubo, J. Xu, Development of a Transferable ReaxFF Parameter Set for Carbon- and Silicon-Based Solid Systems, *The Journal of Physical Chemistry C* 124(18) (2020) 10007-10015.
- [20] G. Kresse, J. Hafner, Ab initio molecular dynamics for liquid metals, *Physical Review B* 47(1) (1993) 558-561.
- [21] G. Kresse, J. Hafner, Ab initio molecular-dynamics simulation of the liquid-metal-amorphous-semiconductor transition in germanium, *Physical Review B* 49(20) (1994) 14251-14269.
- [22] G. Kresse, J. Furthmüller, Efficiency of ab-initio total energy calculations for metals and semiconductors using a plane-wave basis set, *Computational Materials Science* 6(1) (1996) 15-50.
- [23] G. Kresse, J. Furthmüller, Efficient iterative schemes for ab initio total-energy calculations using a plane-wave basis set, *Physical Review B* 54(16) (1996) 11169-11186.
- [24] J.P. Perdew, K. Burke, M. Ernzerhof, Generalized Gradient Approximation Made Simple, *Physical Review Letters* 77(18) (1996) 3865-3868.
- [25] J.P. Perdew, K. Burke, M. Ernzerhof, Generalized Gradient Approximation Made Simple [Phys. Rev. Lett. 77, 3865 (1996)], *Physical Review Letters* 78(7) (1997) 1396-1396.
- [26] P.E. Blöchl, Projector augmented-wave method, *Physical Review B* 50(24) (1994) 17953-17979.
- [27] G. Kresse, D. Joubert, From ultrasoft pseudopotentials to the projector augmented-wave method, *Physical Review B* 59(3) (1999) 1758-1775.
- [28] S. Grimme, Semiempirical GGA-type density functional constructed with a long-range dispersion correction, *Physical Review Letters* 92(7) (2006) 1787-1799.
- [29] A.C.T. van Duin, J.M.A. Baas, B. van de Graaf, Delft molecular mechanics: a new approach to hydrocarbon force fields. Inclusion of a geometry-dependent charge calculation, *Journal of the Chemical Society, Faraday Transactions* 90(19) (1994) 2881-2895.
- [30] F. Ercolessi, J.B. Adams, Interatomic Potentials from First-Principles Calculations: The Force-Matching Method, *Europhysics Letters (EPL)* 26(8) (1994) 583-588.
- [31] S. Plimpton, Fast Parallel Algorithms for Short-Range Molecular Dynamics, *Journal of Computational Physics* 117(1) (1995) 1-19.
- [32] H.M. Aktulga, J.C. Fogarty, S.A. Pandit, A.Y. Grama, Parallel reactive molecular dynamics: Numerical methods and algorithmic techniques, *Parallel Computing* 38(4) (2012) 245-259.
- [33] I.J. Markel, J. Glaser, M. Steinbrück, H.J. Seifert, Experimental and computational analysis of PSZ 10- and PSZ 20-derived Si-C-N ceramics, *Journal of the European Ceramic Society* 39(2) (2019) 195-204.
- [34] C. Palmer David, Visualization and analysis of crystal structures using CrystalMaker software, *Zeitschrift für Kristallographie - Crystalline Materials* 230(9-10) (2015) 559.

[35] K. Yamamoto, Y. Koga, S. Fujiwara, XPS studies of amorphous SiCN thin films prepared by nitrogen ion-assisted pulsed-laser deposition of SiC target, *Diamond and Related Materials* 10(9) (2001) 1921-1926.

Summary

We optimized ReaxFF parameters for Si-C-N-H for simulation of the pyrolysis of polysilazane into amorphous SiCN ceramics. The new parameter set is evaluated on how well it reproduces the DFT potential energy surface in ReaxFF. We find that energy correspondence between ReaxFF and DFT energies is close to 1:1. Simulation of the polysilazane polymer Ceraset at elevated temperature is done and the evolution of different gaseous species is observed. The major gaseous species evolved during simulation of Ceraset are H₂, CH₄, and NH₃ to a lesser degree. While H₂ and CH₄ match what is produced in pyrolysis experiments[1], further work is needed to be sure that the quantity of each gaseous species agree with what should be produced in quantum chemical simulations. A ternary agglomerate is the outcome of simulation of Ceraset, and the agglomerate exhibits the type of bonding to what is expected in amorphous SiCN ceramics. Significant amounts of C-N bonding within the ternary agglomerate do indicate that further improvement of parameters is needed before any meaningful pyrolysis simulations can be done.

References

[1] I.J. Markel, J. Glaser, M. Steinbrück, H.J. Seifert, Experimental and computational analysis of PSZ 10- and PSZ 20-derived Si-C-N ceramics, *Journal of the European Ceramic Society* 39(2) (2019) 195-204.

CONCLUSIONS

The first part of this work, Part I, focuses on high-pressure and materials chemistry. We investigate materials typically synthesized at high pressures and do calculations on the work of adhesion in compound graphene-SiO₂/Si₂CO₂ systems.

In Chapter 1, we study the transformation between α -cristobalite-type and rutile-type for SiO₂, GeO₂, and TiO₂ using two different concerted mechanisms and conducting the transformation at different external pressures. Increasing external pressure favors the rutile-structure type while decreasing pressure favors the cristobalite structure-type. Based on the pressures at which the cristobalite structure-type of GeO₂ and TiO₂ becomes favorable, we predict that cristobalite-GeO₂ and cristobalite-TiO₂ can be synthesized with moderate tensile stresses.

Chapter 2 and Chapter 3 are dedicated to calculations supporting experimental discovery of structures in high pressure experiments. To rationalize the synthesis of *Pbcn*-Sn₂N₂O, we perform enthalpy-pressure calculations and determine that at ambient pressure *Pbcn*-Sn₂N₂O is thermodynamically favored to decompose into its binary phases. Thus, *Pbcn*-Sn₂N₂O must be metastable since it is experimentally recovered at ambient conditions. In the lucky discovery of spinel-type ternary silicon titanium nitride, we predict preferential sites where Ti would substitute in spinel-Si₃N₄. and determine that the lowest energy configurations of ternary silicon titanium nitride exhibit Ti in octahedral sites clustered together. Calculation of enthalpies of formation indicated that ternary silicon titanium nitride is thermodynamically favored to decompose into its binary phases at ambient conditions but was likely recovered in experiment due to kinetics.

In Chapter 4, we calculate the work of adhesion for compound graphene and bilayer-SiO₂ and graphene and Si₂CO₂ systems. To get around the poor description of dispersion interactions in PBE[1, 2] we use different dispersion correction methods which

all yield results that agree with experiment for graphite. We find that the work of adhesion is much higher in graphene-Si₂CO₂ systems than in the graphene-bilayer-SiO₂ system. Analysis of charges rules out charge transfer as significantly impacting work of adhesion in these systems, so we conclude that another phenomena is responsible for the different work of adhesion values.

Part II is about investigations of amorphous ceramics with a classical potential and force field.

Using the Tersoff potential[3] we calculate elastic properties of amorphous SiCO ceramics in Chapter 1. By independently varying parameters, we predict that increasing free carbon content increases elastic properties and increasing density also increases elastic properties contradicting Sorarù et al[4] who could not independently vary free carbon content and density. Additionally, we determine that the morphology of the free carbon phase can impact elastic properties, and when composition is fixed models with more segregated free carbon morphologies exhibit higher elastic moduli.

In Chapter 2, we develop a new method to quantify the morphology of free carbon in carbon-containing amorphous ceramics by counting the extent of three-coordinated carbon through topological shells. This topological shell counting method can be used to differentiate between amorphous ceramics containing different free carbon morphologies.

Chapter 3 involves the development of a new ReaxFF parameter set to study the polymer-to-ceramic conversion process of polysilazanes into amorphous SiCN ceramics. There are no complete SiCNH parameter sets in literature so we start from parameters from Kulkarni et al.[5] and Ponomarev et al.[6] and train them on DFT calculations and ab initio molecular dynamics. The resulting parameter set is evaluated for good reproduction of the DFT potential energy surface for Si-C-N-H materials and would likely perform well on simulations of SiCNH materials; however, issues observed during

simulation of Ceraset means that the parameter set must be improved before pyrolysis simulations, and essentially the polymer-to-ceramic conversion process, can be studied.

References

- [1] J.P. Perdew, K. Burke, M. Ernzerhof, Generalized Gradient Approximation Made Simple, *Physical Review Letters* 77(18) (1996) 3865-3868.
- [2] J.P. Perdew, K. Burke, M. Ernzerhof, Generalized Gradient Approximation Made Simple [*Phys. Rev. Lett.* 77, 3865 (1996)], *Physical Review Letters* 78(7) (1997) 1396-1396.
- [3] J. Tersoff, New empirical approach for the structure and energy of covalent systems, *Physical Review B* 37(12) (1988) 6991-7000.
- [4] G.D. Sorarù, L. Kundanati, B. Santhosh, N. Pugno, Influence of free carbon on the Young's modulus and hardness of polymer-derived silicon oxycarbide glasses, *Journal of the American Ceramic Society* 102(3) (2019) 907-913.
- [5] A.D. Kulkarni, D.G. Truhlar, S. Goverapet Srinivasan, A.C.T. van Duin, P. Norman, T.E. Schwartzenuber, Oxygen Interactions with Silica Surfaces: Coupled Cluster and Density Functional Investigation and the Development of a New ReaxFF Potential, *The Journal of Physical Chemistry C* 117(1) (2013) 258-269.
- [6] I. Ponomarev, A.C.T. van Duin, P. Kroll, Reactive Force Field for Simulations of the Pyrolysis of Polysiloxanes into Silicon Oxycarbide Ceramics, *The Journal of Physical Chemistry C* 123(27) (2019) 16804-16812.

APPENDIX A

PUBLICATION INFORMATION AND CONTRIBUTING AUTHORS

Material from this work is reproduced, in whole or in part, from several publications.

Part I Chapter 1 is reproduced in part from: S. Haseen, P. Kroll, Paving the way for cristobalite TiO_2 and GeO_2 attainable under moderate tensile stress: A DFT study of transformation paths and activation barriers in cristobalite-rutile transformations of MO_2 ($\text{M} = \text{Si}, \text{Ge}, \text{Ti}$), *Computational Materials Science* 170 (2019) 109170.

Part I Chapter 2 is reproduced in part from: S. Bhat, L. Wiehl, S. Haseen, P. Kroll, K. Glazyrin, P. Gollé-Leidreiter, U. Kolb, R. Farla, J.-C. Tseng, E. Ionescu, T. Katsura, R. Riedel, A Novel High-Pressure Tin Oxynitride $\text{Sn}_2\text{N}_2\text{O}$, *Chemistry—A European Journal* 26(10) (2020) 2187-2194.

Part I Chapter 3 is reproduced in part from: S. Bhat, A. Ale, S. Bernard, W. Zhang, R. Ishikawa, S. Haseen, P. Kroll, L. Wiehl, R. Farla, T. Katsura, Y. Ikuhara, R. Riedel, Discovery of Ternary Silicon Titanium Nitride with Spinel-Type Structure, *Scientific Reports* 10(1) (2020) 7372.

Part II Chapter 1 is taken from a manuscript in preparation: Haseen, S.; Kroll, P. Analyzing the Effect Of Composition, Density, and the Morphology of the “Free” Carbon Phase on Elastic Moduli in Silicon Oxycarbide